Investigation of Fundamental Degradation Mechanism toward Developing Highly Durable Electrocatalysts for PEFC

趙, 暁静

https://doi.org/10.15017/1441235

出版情報：九州大学, 2013, 博士（工学）, 課程博士
バージョン：
権利関係：全文ファイル公表済

Investigation of Fundamental Degradation Mechanism toward Developing Highly Durable Electrocatalysts for PEFC

A dissertation submitted to the
KYUSHU UNIVERSITY
for the degree of Doctor of Engineering

by

ZHAO Xiaojing
Department of Hydrogen Energy Systems
Graduate School of Engineering
Kyushu University
January 2014

Approved by:

Prof. Dr. Kazunari Sasaki, examiner/supervisor
Faculty of Engineering, Kyushu University

Prof. Dr. Etsuo Akiba, co-examiner
Faculty of Engineering, Kyushu University

Prof. Dr. Kohei Ito, co-examiner
Faculty of Engineering, Kyushu University

Prof. Dr. Hiroshige Matsumoto, co-examiner
International Institute for Carbon-Neutral Energy Research, Kyushu University

Assoc. Prof. Dr. Akari Hayashi, co-advisor
International Research Center for Hydrogen Energy, Kyushu University

Fukuoka, Japan

Abstract

This study deals with development of advanced electrocatalysts and exploration of degradation mechanisms for polymer electrolyte fuel cell (PEFC), which is an essential technology for our sustainable society. Although PEFC is an attractive power device for both stationary and automobile applications, cost and durability are still two important issues to overcome for further improvement and commercialization of this technology. Among various factors causing degradation, catalyst deterioration due to the electrochemical oxidation (corrosion) of the carbon support is one of the most serious problems especially for automobile application. We are challenging to overcome such catalyst degradation problem.

Graphite structure of carbon is known to have resistance to carbon corrosion, and some work developing electrocatalysts with graphitic carbon has been reported. However, there is no report systematically studying the detailed influence of graphitization degree on electrocatalytic durability. Therefore, in this study, we report the control of graphitization degree through the systematic heat treatment and then investigate the durability of electrocatalysts derived from such carbon after platinum deposition. Their nanostructures before and after the durability tests are examined in detail for exploration of degradation mechanisms.

For this purpose, two kinds of commercially available state-of-the-art carbon materials, Vulcan XC-72 and Ketjen Black EC600-JD, were heat treated at 1100, 1600, and 2000 °C in order to produce graphitized surface. Eight different Pt/C electrocatalysts (Pt/VC, Pt/GVC1100, Pt/GVC1600, Pt/GVC2000, Pt/KB, Pt/GKB1100, Pt/GKB1600, and Pt/GKB2000) were synthesized. Their durability was evaluated using an electrochemically accelerating potential cycle protocol, considering a practical condition of fuel cell vehicles (Triangle wave between 1.0 V and 1.5 V vs. RHE, 2 s/cycle) in N_2 saturated 0.1 M $HClO_4$ solution at 25 °C. Their durability was studied through the change in electrochemically active surface area (ECA), oxygen reduction reactivity (ORR), and the size of platinum particles in TEM images. As expected, higher graphitization degree led to an increase in corrosion resistance, but at the same time resulted in an increase in the mobility of platinum particles on carbon supports. Therefore, an optimum condition with both high corrosion resistance and sufficient interaction between platinum particles and carbon was investigated. Consequently, in this study we have found that the graphitization at 1600 °C is optimum among 1100, 1600, and 2000 °C to obtain highest

durability for Pt/C electrocatalysts. Graphitization degree obviously comes to be an important factor to develop electrocatalysts with high durability.

For investigating practical application of our electrocatalysts, membrane electrolyte assemblies (MEAs) with Pt/VC and Pt/GVC1600 as cathode catalyst layers were prepared and their current-voltage (I-V) characteristics, and durability performance were evaluated. Initial performance of MEA was found to be salmost the same between these two electrocatalysts, but regarding to durability, Pt/GVC1600 showed much more improved durability than Pt/VC. Heat treatment of carbon supports at an optimum temperature leads to an increase in durability even at an actual PEFC operational temperature.

Nanostructure observation of Pt/C electrocatalysts also proved the improved durability for Pt/C electrocatalysts heat-treated at 1600 °C by their structure with graphite-like surface and sufficient interaction between platinum particles and carbon. On the other hand, for Pt/KB, even though the growth of platinum particle size was not very much, the retention of ECA after the potential cycle test was extremely low such as 2 %. This result leads to the fact that the degradation of Pt/C electrocatalysts could not be explained only by platinum growth or agglomeration during the potential cycle test. To understand much lower ECA than the expected value, the electrolyte solution after the potential cycle test was examined by inductively coupled plasma (ICP) analysis. As a result, dissolution of platinum was found to be a predominate factor for degradation of Pt/KB.

Further, an accelerated degradation test was newly introduced by using in-situ SEM/STEM observation at elevated temperature under the air-containing condition to understand the fundamental degradation mechanism of electrocatalysts. Simultaneous in-situ SEM/STEM observation for selected electrocatalysts showed that embedded platinum into carbon surface was a major reason for degradation of electrocatalysts. This phenomenon was also suppressed when carbon surface was graphitized. Similar phenomenon was observed after the potential cycle test for Pt/KB, which had the lowest durability. Therefore, we believe that degradation mechanism observed by heating in the air is the same as the degradation mechanism derived by the potential cycle test even though the acceleration condition is more severe for heating in the air in this study.

In conclusion, we have investigated the possible degradation mechanism of electrocatalysts and have found that graphitization degree is the important factor to design electrocatalysts with both high activity and high durability.

Acknowledgements

I would like to express my deepest gratitude to my supervisor, *Prof. Kazunari Sasaki*, for his guidance and encouragement throughout my doctoral period in Kyushu University. Also, his scientific ability, insight and his social skill are admirable. It has been an honor and a pleasure knowing and learning from him.

I wish to express my great thanks to my dissertation committee members, *Prof. Etsuo Akiba, Prof. Kohei Ito*, *and Prof. Hiroshige Matsumoto* for their time commitment, useful discussions and advices throughout this process.

I sincerely give my grateful to my advisor, *Assoc. Prof. Akari Hayashi*, for her valuable guidance and sustained support throughout my studies. She has taught me not only knowledge and techniques on studies, but also how to be a devoted researcher. Words could not express my admiration for her rigorous working attitude and gratitude for pertinent advices and encouragements she gave me.

I would like to give my grateful to *Mr. Ken'ichi Kimijima* and *Ichizo Yagi* in FC-Cubic TRA (Tokyo) who spent a lot of time helping me to heat-treated my carbon materials. I would like to grateful to *Mr. Hiroaki Matsumoto* in Hitachi High Technologies Corporation for their collaboration on the in-situ SEM/STEM observation. I would also like to thank to *Mr. Takeshi Daio* for his supporting when he was in the research laboratory for High Voltage Electron Microscopy (Kyushu University).

I am grateful to many of my colleagues (past and current) in Laboratory of Hydrogen Utilization Processes (Sasaki Lab.) for their assistance to this thesis work. I would like especially thank to *Ms. Zhiyun Noda* for her guidance and assistance for my experiments throughout my study in Kyushu University.

I would like to thank my families for giving me their love and support. Especially thank to my husband, Benning Lian, for his undying support, encouragement and

assistance during this period. He work hard every day and take care of our son after work without complains even one word. I must express my apologies to my son, Mingde Lian, for leaving him with his father in Hyogo Prefecture when he was only six years old. He is a sunny and optimistic boy and told me to fighting with study many times on the phone. I've got the best family in the world!

Lastly, I gratefully acknowledge to the China Scholarship Council for giving me a scholarship to study in Kyushu University. This study was supported by "Demonstration Research on a Hydrogen-based Society through Collaboration among Industry, University, Government, and Local Community", MEXT Scientific Research S (No. 23226015), JSPS, Japan and Grant-in Aid for Young Scientists (A) (No. 25701016), JSPS, Japan.

Fukuoka, January 2014
Xiaojing Zhao

Contents

Abstract i

Acknowledgements iii

Contents v

List of Figures ix

List of Tables xvii

Chapter 1 Introduction 1

1.1 Introduction 1

1.1.1 Overview of Fuel Cells 1

1.1.2 Principle of Fuel Cells 3

1.1.3 Energy and the Reversible OCV of Fuel Cells 4

1.1.4 Efficiency of Fuel Cells 7

1.1.5 Fuel Cell Irreversibilities – Causes of Voltage Drop 8

1.1.6 Types of Fuel cells 10

1.2 Polymer Electrolyte Fuel Cells (PEFCs) 11

1.2.1 Characteristics of PEFCs 11

1.2.2 Electrodes for PEFCs 13

1.2.3 Problems to be Solved 14

1.2.4 Recent Research Trend against Carbon Corrosion Problems 15

1.3 Objective of This Study 16

References 17

Chapter 2 Experimental 21

2.1 Materials 21

2.2 Preparation and Characterization of Carbon Supports 21

2.2.1 Carbon Supports Used in This Study 21

2.2.2 Heat Treatment 21

2.2.3 Specific Surface Area by Nitrogen Adsorption Measurement 22

2.2.4 Graphitization Degree by X-ray Diffraction 23
2.3 Preparation and Characterization of Pt/C Electroatalysts 24
2.3.1 Preparation 24
2.3.2 Platinum Loading by TG Measurement 25
2.3.3 Platinum Crystallize Size by X-ray Diffraction 25
2.4 Electrochemical Evaluation of Pt/C Electrocatalysts 26
2.4.1 Three Electrode Set-up 26
2.4.2 Working Electrode 27
2.4.3 Cyclic Voltammetry 28
2.4.4 Rotation Disk Electrode Method 30
2.4.5 Durability 32
2.4.6 Platinum Dissolution 33
2.5 Evaluation of MEAs 34
2.5.1 Preparation 34
2.5.2 I-V Characteristic 35
2.5.3 Ohmic Resistance 36
2.5.4 Durability 38
2.6 Analyses by Electron Microscopy 38
2.6.1 Ex-situ Observation 38
2.6.2 In-situ Observation 38
References 40

Chapter 3 Material Characterization of Electrocatalysts 41
3.1 Carbon/Graphitized Carbon 41
3.1.1 Specific Surface Area 41
3.1.2 Graphitization Degree 42
3.2 Platinum Deposited Carbon/Graphitized Carbon 43
3.2.1 Platinum Loading 43
3.2.2 TEM Observation 44
3.2.3 Average Platinum Crystallite and Platinum Particle Size 46
3.3 Conclusions 46

References 48

Chapter 4 Electrochemical Characterization of Pt/C Electrocatalysts 49

4.1 Electrochemical Evaluation of Pt/Vulcan Group Electrocatalysts at 25 °C 49

4.1.1 Change in Cyclic Voltammograms During the Potential Cycle Test 49

4.1.2 Change in ECA During the Potential Cycle Test 52

4.1.3 Change in Linear Sweep Voltammograms for ORR During the Potential Cycle Test 55

4.1.4 Change in Mass Activity for ORR During the Potential Cycle Test 58

4.2 Electrochemical Evaluation of Pt/Ketjen Black Group Electrocatalysts at 25 °C 61

4.2.1 Change in Cyclic Voltammograms During the Potential Cycle Test 61

4.2.2 Change in ECA During the Potential Cycle Test 63

4.2.3 Change in Linear Sweep Voltammograms for ORR During the Potential Cycle Test 65

4.2.4 Change in Mass Activity for ORR During the Potential Cycle Test 67

4.3 Electrochemical Evaluation of Selected Pt/C Electrocatalysts at 60 °C 70

4.4 Conclusions 72

References 73

Chapter 5 Evaluation of MEAs 75

5.1 Preparation of Catalyst Layers 75

5.1.1 Evaluation of Sufficient Nafion Amount for the Anode Catalyst Layer 76

5.1.2 Evaluation of Sufficient Nafion Amount for the Cathode Catalyst Layer with Pt/VC 77

5.1.3 Evaluation of Sufficient Nafion Amount for the Cathode Catalyst Layer with Pt/GVC1600 78
5.2 Electrochemical Evaluation of MEAs 80
5.2.1 I-V characteristics 80
5.2.2 Change in I-V Characteristics During the Potential Cycle Test 81
5.3 Conclusions 83
References 85

Chapter 6 Degradation Mechanism for Pt/C Electrocatalysts 87
6.1 Degradation of Pt/C Electrocatalysts in Half-cell Reactions 87
6.1.1 Evaluation of Pt/Vulcan Group Electrocatalysts by Ex-situ TEM Observation 87
6.1.2 Evaluation of Pt/Ketjen Black Group Electrocatalysts by Ex-situ TEM Observation 91
6.1.3 Evaluation of Pt/C Electrocatalysts by ICP analysis 94
6.2 Degradation of Pt/C Electrocatalysts at Elevated Temperatures Under the Air (Collaborative Work with Hitachi High Technologies Corporation) 95
6.2.1 Evaluation of Pt/VC by In-situ SEM/STEM Observation 95
6.2.2 Evaluation of Pt/GVC1600 by In-situ SEM/STEM Observation 97
6.2.3 Comparison with Degradation in Half-cell Reaction through Ex-situ SEM/STEM Observation 99
6.3 Degradation of Pt/C Electrocatalysts in MEAs 102
6.4 Conclusions 103
References 105

Chapter 7 Conclusions 107
7.1 Conclusions 107
7.2 Outlook and Future Work 107
References 109

List of Figures

Figure 1.1	A simple fuel cell.	1
Figure 1.2	Fuel cell development history [1].	2
Figure 1.3	Reactions and charge flow for PEFC [9].	3
Figure 1.4	Fuel cell inputs and outputs [9].	4
Figure 1.5	A graph showing the voltage for a typical polymer electrolyte fuel cell.	8
Figure 1.6	Components of a single PEFC.	12
Figure 1.7	A schematic diagram of a typical MEA.	13
Figure 1.8	Transport of gases, protons, and electrons at cathode layer [13].	14
Figure 1.9	Diagram of the fuel cell degradation derived by carbon corrosion.	15
Figure 2.1	TEM images of Vulcan XC-72 (a) and Ketjen Black (b).	22
Figure 2.2	Flow chart of Pt/C electrocatalyst preparation.	25
Figure 2.3	Three electrode set-up for the half-cell measurement.	27
Figure 2.4	Working electrode preparation.	28
Figure 2.5	Wave pattern of the potential apply on CV measurement.	28
Figure 2.6	A typical cyclic voltammogram of a Pt/C electrocatalyst.	29
Figure 2.7	A schematic view of the reaction occuring on a rotation disk electrode.	30
Figure 2.8	LSV curves of a typical Pt/C electrocatalyst at different rotational speeds.	31
Figure 2.9	Koutecky-Levich plot of a typical Pt/C electrocatalyst.	32
Figure 2.10	Start-stop potential cycle protocol recommended by FCCJ [8].	33
Figure 2.11	Spray-printing of MEA.	34
Figure 2.12	A schematic drawing of hot-pressing (left) and a photo of MEA made in this study (right).	35
Figure 2.13	A schematic diagram of setting up of MEA on the holder.	36
Figure 2.14	Typical voltage changes just before and after the current is interrupted. Linear change (circled) can be used as ohmic drop.	37

Figure 2.15	A photo of a MEA with the reference electrode.	37
Figure 3.1	XRD spectra showing carbon (002) diffraction using silicon as a standard for a) VC, GVC1100, GVC1600 and GVC2000 and b) KB, GKB1100, GKB1600 and GKB2000.	42
Figure 3.2	TEM images of a) Pt/VC, b) Pt/GVC1100, c) Pt/GVC1600, and d) Pt/GVC2000.	44
Figure 3.3	TEM images of a) Pt/KB, b) Pt/GKB1100, c) Pt/GKB1600, and d) Pt/GKB2000.	45
Figure 4.1	Cyclic voltammograms of Pt/VC after 0, 10000, 30000, 60000 cycles of the potential cycle test. Measurements were recorded in N_2 saturated 0.1 M $HClO_4$ solution at 25 °C with the scan rate of 50 mV/s.	50
Figure 4.2	Cyclic voltammograms of Pt/GVC1100 after 0, 10000, 30000, 60000 cycles of the potential cycle test. Measurements were recorded in N_2 saturated 0.1 M $HClO_4$ solution at 25 °C with the scan rate of 50 mV/s.	51
Figure 4.3	Cyclic voltammograms of Pt/GVC1600 after 0, 10000, 30000, 60000 cycles of the potential cycle test. Measurements were recorded in N_2 saturated 0.1 M $HClO_4$ solution at 25 °C with the scan rate of 50 mV/s.	51
Figure 4.4	Cyclic voltammograms of Pt/GVC2000 after 0, 10000, 30000, 60000 cycles of the potential cycle test. Measurements were recorded in N_2 saturated 0.1 M $HClO_4$ solution at 25 °C with the scan rate of 50 mV/s.	52
Figure 4.5	Change in ECA during the potential cycle test for Pt/VC, Pt/GVC1100, Pt/GVC1600, and Pt/GVC2000.	53
Figure 4.6	Change in ECA during the potential cycle test for Pt/VC including the case that detachment of Pt/VC from the electrode has occured.	54
Figure 4.7	Change in ECA during the potential cycle test for Pt/GVC1100 including the case that detachment of Pt/GVC1100 from the electrode has occured.	55

Figure 4.8	Linear sweep voltammograms of Pt/VC after 0, 10000, 30000, 60000 cycles of the potential cycle test. Measurements were recorded in O_2 saturated 0.1 M $HClO_4$ solution at 25 °C with the scan rate of 10 mV/s and the rotation of 1600 rpm.	56
Figure 4.9	Linear sweep voltammograms of Pt/GVC1100 after 0, 10000, 30000, 60000 cycles of the potential cycle test. Measurements were recorded in O_2 saturated 0.1 M $HClO_4$ solution at 25 °C with the scan rate of 10 mV/s and the rotation of 1600 rpm.	56
Figure 4.10	Linear sweep voltammograms of Pt/GVC1600 after 0, 10000, 30000, 60000 cycles of the potential cycle test. Measurements were recorded in O_2 saturated 0.1 M $HClO_4$ solution at 25 °C with the scan rate of 10 mV/s and the rotation of 1600 rpm.	57
Figure 4.11	Linear sweep voltammograms of Pt/GVC2000 after 0, 10000, 30000, 60000 cycles of the potential cycle test. Measurements were recorded in O_2 saturated 0.1 M $HClO_4$ solution at 25 °C with the scan rate of 10 mV/s and the rotation of 1600 rpm.	57
Figure 4.12	Koutecky-Levich plot (at 0.90 V) of Pt/VC after 0, 10000, 30000, 60000 cycles of the potential cycle test.	58
Figure 4.13	Koutecky-Levich plot (at 0.90 V) of Pt/GVC1100 after 0, 10000, 30000, 60000 cycles of the potential cycle test.	59
Figure 4.14	Koutecky-Levich plot (at 0.90 V) of Pt/GVC1600 after 0, 10000, 30000, 60000 cycles of the potential cycle test.	59
Figure 4.15	Koutecky-Levich plot (at 0.90 V) of Pt/GVC2000 after 0, 10000, 30000, 60000 cycles of the potential cycle test.	60
Figure 4.16	Change in ORR mass activity of Pt/VC, Pt/GVC1100, Pt/GVC1600, and Pt/GVC2000 after 0, 10000, 30000, 60000 cycles of the potential cycle test.	60
Figure 4.17	Cyclic voltammograms of Pt/KB after 0, 10000, 30000, 60000 cycles of the potential cycle test. Measurements were recorded in N_2 saturated 0.1 M $HClO_4$ solution at 25 °C with the scan rate of 50 mV/s.	61

Figure 4.18 Cyclic voltammograms of Pt/GKB1100 after 0, 10000, 30000, 60000 cycles of the potential cycle test. Measurements were recorded in N_2 saturated 0.1 M $HClO_4$ solution at 25 °C with the scan rate of 50 mV/s. 62

Figure 4.19 Cyclic voltammograms of Pt/GKB1600 after 0, 10000, 30000, 60000 cycles of the potential cycle test. Measurements were recorded in N_2 saturated 0.1 M $HClO_4$ solution at 25 °C with the scan rate of 50 mV/s. 62

Figure 4.20 Cyclic voltammograms of Pt/GKB2000 after 0, 10000, 30000, 60000 cycles of the potential cycle test. Measurements were recorded in N_2 saturated 0.1 M $HClO_4$ solution at 25 °C with the scan rate of 50 mV/s. 63

Figure 4.21 Change in ECA during the potential cycle tests for Pt/KB, Pt/GKB1100, Pt/GKB1600, and Pt/GKB2000. 64

Figure 4.22 Linear sweep voltammograms of Pt/KB after 0, 10000, 30000, 60000 cycles of the potential cycle test. Measurements were recorded in O_2 saturated 0.1 M $HClO_4$ solution at 25 °C with the scan rate of 10 mV/s and the rotation of 1600 rpm. 65

Figure 4.23 Linear sweep voltammograms of Pt/GKB1100 after 0, 10000, 30000, 60000 cycles of the potential cycle test. Measurements were recorded in O_2 saturated 0.1 M $HClO_4$ solution at 25 °C with the scan rate of 10 mV/s and the rotation of 1600 rpm. 66

Figure 4.24 Linear sweep voltammograms of Pt/GKB1600 after 0, 10000, 30000, 60000 cycles of the potential cycle test. Measurements were recorded in O_2 saturated 0.1 M $HClO_4$ solution at 25 °C with the scan rate of 10 mV/s and the rotation of 1600 rpm. 66

Figure 4.25 Linear sweep voltammograms of Pt/GKB2000 after 0, 10000, 30000, 60000 cycles of the potential cycle test. Measurements were recorded in O_2 saturated 0.1 M $HClO_4$ solution at 25 °C with the scan rate of 10 mV/s and the rotation of 1600 rpm. 67

Figure 4.26 Koutecky-Levich plot (at 0.90 V) of Pt/KB after 0, 10000, 30000, 60000 cycles of the potential cycle test. 68

Figure 4.27	Koutecky-Levich plot (at 0.90 V) of Pt/GKB1100 after 0, 10000, 30000, 60000 cycles of the potential cycle test.	68
Figure 4.28	Koutecky-Levich plot (at 0.90 V) of Pt/GKB1600 after 0, 10000, 30000, 60000 cycles of the potential cycle test.	69
Figure 4.29	Koutecky-Levich plot (at 0.90 V) of Pt/GKB2000 after 0, 10000, 30000, 60000 cycles of the potential cycle test.	69
Figure 4.30	Change in ORR mass activity of Pt/KB, Pt/GKB1100, Pt/GKB1600, and Pt/GKB2000 after 0, 10000, 30000, 60000 cycles of the potential cycle test.	70
Figure 4.31	Change in ECA during the potential cycle tests for Pt/VC, Pt/GVC1600, Pt/KB, and Pt/GKB1600 at 60 °C.	71
Figure 5.1	I-V characteristics of MEA with different Nafion contents for both anode and cathode with a standard electrocatalyst, TEC10E50E. Platinum loading was kept to 0.3 mg cm^{-2} in all the cases. Measurements were done at the cell temperature of 80 °C under the flow of 100% humidified H_2 and air into the anode and the cathode, respectively, with a constant flow rate of 100 cc min^{-1}.	76
Figure 5.2	I-V characteristics of MEA with different Nafion contents for the cathode catalyst layer with Pt/VC. Platinum loading was kept to 0.3 mg cm^{-2} in all the cases. Measurements were done at the cell temperature of 80 °C under the flow of 100% humidified H_2 and air into the anode and the cathode, respectively, with a constant flow rate of 100 cc min^{-1}.	77
Figure 5.3	SEM images of cross section of MEA (a) and Pt/VC cathode catalyst layers with different Nafion contents (30% (b), 24% (c), and 16% (d)).	78
Figure 5.4	I-V characteristics of MEA with different Nafion contents for the cathode catalyst layer with Pt/GVC1600. Platinum loading was kept to 0.3 mg cm^{-2} in all the cases. Measurements were done at the cell temperature of 80 °C under the flow of 100% humidified H_2 and air into the anode and the cathode, respectively, with a constant flow rate of 100 cc min^{-1}.	79

Figure 5.5 SEM images of Pt/GVC1600 cathode catalyst layers with different Nafion contents (24% (a), and 20% (b)). 79

Figure 5.6 I-V characteristics of MEA with Pt/VC (blue) and Pt/GVC1600 (red) for the cathode. Platinum loading was kept to 0.3 mg cm^{-2} in all the cases. Measurements were done at the cell temperature of 80 °C under the flow of 100% humidified H_2 and air into the anode and the cathode, respectively, with a constant flow rate of 100 cc min^{-1}. 80

Figure 5.7 Change in I-V characteristics during the potential cycling between 1.0 and 1.5 V vs. RHE for MEA with Pt/VC. Platinum loading was kept to 0.3 mg cm^{-2} in all the cases. I-V measurements were done at the cell temperature of 80 °C under the flow of 100% humidified H_2 and air into the anode and the cathode, respectively, with a constant flow rate of 100 cc min^{-1}. 81

Figure 5.8 Change in I-V characteristics during the potential cycling between 1.0 and 1.5 V vs. RHE for MEA with Pt/GVC1600. Platinum loading was kept to 0.3 mg cm^{-2} in all the cases. I-V measurements were done at the cell temperature of 80 °C under the flow of 100% humidified H_2 and air into the anode and the cathode, respectively, with a constant flow rate of 100 cc min^{-1}. 82

Figure 6.1 TEM images of Pt/VC before (a) and after (b) 60000 cycles of the potential cycle test. 88

Figure 6.2 TEM images of Pt/GVC1100 before (a) and after (b) 60000 cycles of the potential cycle test. 89

Figure 6.3 TEM images of Pt/GVC1600 before (a) and after (b) 60000 cycles of the potential cycle test. 89

Figure 6.4 TEM images of Pt/GVC2000 before (a) and after (b) 60000 cycles of the potential cycle test. 89

Figure 6.5 TEM images of Pt/KB before (a) and after (b) 60000 cycles of the potential cycle test. 91

Figure 6.6 TEM images of Pt/GKB1100 before (a) and after (b) 60000 cycles of the potential cycle test. 92

Figure 6.7	TEM images of Pt/GKB1600 before (a) and after (b) 60000 cycles of the potential cycle test.	92
Figure 6.8	TEM images of Pt/GKB2000 before (a) and after (b) 60000 cycles of the potential cycle test.	92
Figure 6.9	Initial SEM (left) and STEM (right) images of Pt/VC.	95
Figure 6.10	Sequence of SEM images for Pt/VC. Observation was performed at 200 °C during the air injection.	96
Figure 6.11	SEM (left) and STEM (right) images of Pt/VC after the accelerated degradation test at 200 °C under the air injection.	97
Figure 6.12	Initial SEM (left) and STEM (right) images of Pt/GVC1600.	97
Figure 6.13	Sequence of SEM images for Pt/GVC1600. Observation was performed at 200 °C during the air injection.	98
Figure 6.14	SEM (left) and STEM (right) images of Pt/GVC1600 after the accelerated degradation test at 200 °C under the air injection.	99
Figure 6.15	SEM (left) and STEM (right) images of Pt/VC after the 60000 potential cycle test. Both images were obtained at the exactly same position by switching the two modes.	100
Figure 6.16	SEM (left) and STEM (right) images of Pt/GVC1600 after the 60000 potential cycle test. Both images were obtained at the exactly same position by switching the two modes.	100
Figure 6.17	SEM (left) and STEM (right) images of Pt/KB after the 60000 potential cycle test. Both images were obtained at the exactly same position by switching the two modes.	101
Figure 6.18	SEM (left) and STEM (right) images of Pt/KB before the potential cycle test. Both images were obtained at the exactly same position by switching the two modes.	101
Figure 6.19	SEM images of Pt/VC cathode catalyst layer before (a) and after (b) the 5000 potential cycle test.	102
Figure 6.20	SEM images of Pt/GVC1600 cathode catalyst layer before (a) and after (b) the 5000 potential cycle test.	102
Figure 7.1	A SEM image of powder MC.	108

List of Tables

Table 1.1	$\Delta\bar{g}_f$ for the reaction $H_2 + 1/2\ O_2 \rightarrow H_2O$ at various temperatures [9].	5
Table 1.2	Different types of fuel cells [9].	10
Table 2.1	Heat treatment of Vulcan and Ketjen Black.	22
Table 2.2	Measurement conditions of X-ray diffraction for carbon materials.	24
Table 2.3	Measurement conditions of X-ray diffraction for Pt/C electrocatalysts.	26
Table 2.4	Conditions for MEA preparation.	35
Table 2.5	Conditions of MEA measurement.	36
Table 3.1	Specific surface areas of prepared carbon materials.	41
Table 3.2	Interlayer spacing d_{002} and crystallite size $L_c(002)$ for prepared carbon materials.	42
Table 3.3	Platinum loading determined from TG measurements for prepared Pt/C electrocatalysts.	43
Table 3.4	Average platinum crystallite and platinum particle size analyzed by X-ray diffraction and TEM.	46
Table 4.1	ECAs of Pt/Vulcan group electrocatalysts.	53
Table 4.2	ECAs of Pt/Ketjen Black group electrocatalysts.	64
Table 4.3	ECAs for selected Pt/C electrocatalysts at 60 °C.	71
Table 5.1	Summary of optimized Nafion content reported by various researchers.	76
Table 5.2	Ohmic resistance of MEAs with Pt/VC and Pt/GVC1600 cathode layer.	81
Table 5.3	Changes in cell voltage of MEAs with Pt/VC and Pt/GVC1600 during the potential cycle test.	82
Table 5.4	Comparison of MEA performance with other studies.	83
Table 6.1	Average platinum particle size of Pt/Vulcan group electrocatalysts before and after the potential cycle test.	90
Table 6.2	Theoretical surface areas (TSAs) of Pt/Vulcan group electrocatalysts.	91

Table 6.3 Average platinum particle size of Pt/Ketjen Black group electrocatalysts before and after the potential cycle test. 93

Table 6.4 Theoretical surface areas (TSAs) of Pt/Ketjen Black group electrocatalysts. 94

Table 6.5 Platinum dissolution in the electrolyte analyzed by ICP. 94

Chapter 1

Introduction

1.1 Introduction

1.1.1 Overview of Fuel Cells

A fuel cell is an electrochemical energy device which directly converts chemical energy into electrical energy. Figure 1.1 shows a simple fuel cell. Electricity is produced by the chemical reaction between hydrogen and oxygen. The product is only water.

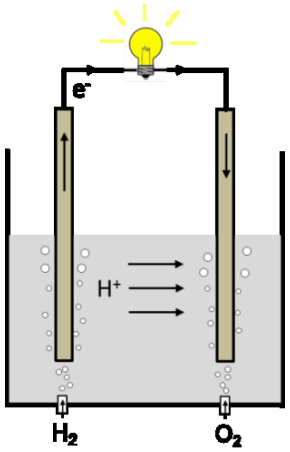

Figure 1.1 A simple fuel cell.

Fuel cell has been studied as an attractive power device owing to high efficiency and zero CO_2 emission for a long period. The timeline of fuel cell development history is shown in Figure 1.2 [1]. The discovery of the fuel cell operating principle – the gaseous fuels that generate electricity, is attributed to William Grove in 1839 [2], although it appears that a Swiss scientist Christian F. Shoenbein independently discovered almost the same effect at about the same time (or even a year before) [3]. However, in spite of sporadic attempts to make a practical device, the fuel cell, or the "gaseous voltaic battery" as it was called by Grove [4], remained nothing more than a scientific curiosity for almost a century.

E. Chen, in *Fuel Cells Technology Handbook* [5], provides a detailed description of

early fuel cell developments. Francis T. Bacon, who started working on practical fuel cells in 1937, developed a 6 kW fuel cell by the end of the 1950s. However, the first practical fuel cell applications were started as U.S. Space Program. General Electric developed the first polymer electrolyte fuel cells which were used in the Gemini Program in the early 1960s. This was followed by the Apollo Space program, which used the fuel cells to generate electricity for life support, guidance, and communications. These fuel cells were built by Pratt and Whitney based on license taken on Bacon`s patents. In the mid-1960s General Motors made an experiment on a fuel cell – powered van, whose fuel cells were developed by Union Carbide.

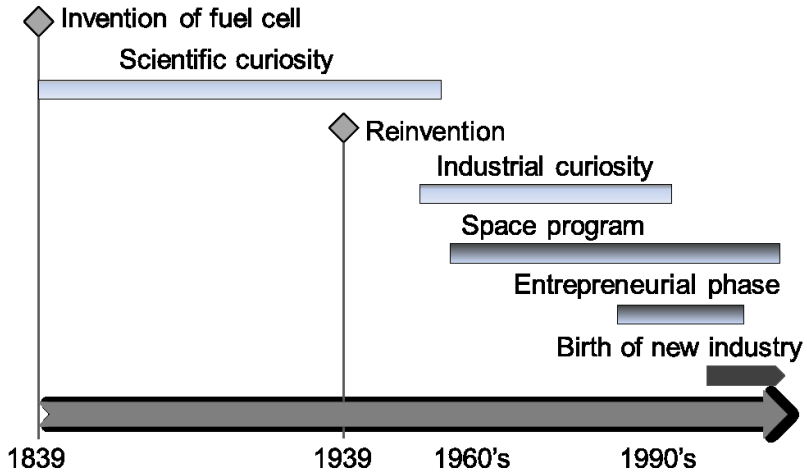

Figure 1.2 Fuel cell development history [1].

Although fuel cells have continued to be successfully used in the U.S. space program until today, they were again "forgotten" for terrestrial applications until the early 1990s. In 1989, Perry Energy Systems, a division of Perry Technologies, working with Ballard and then emerging Canadian company, successfully demonstrated a polymer electrolyte membrane fuel cell (PEFC) – powered submarine. In 1993, Ballard Power Systems demonstrated fuel cell – powered buses. Energy partners, a successor of Perry Energy Systems, demonstrated the first passenger car running on PEFCs in 1993 [6]. The car companies, supported by the U.S. Department of Energy, picked up on this activity and by the end of the century almost every car manufacturer had built and demonstrated a fuel cell – powered vehicle. A new industry was born. The stocks of fuel cell companies, such as Ballard and PlugPower, soared in early 2000, based on a promise of a new energy revolution. The number of fuel cell – related patents worldwide, but primarily in the

United States and Japan, is increasing dramatically [7-8], showing continuous interest and involvement of the scientific and engineering community.

Over the last five years, growth in shipments of fuel cells has rapidly accelerated as various applications have become commercialized. Japan started the commercialization of residential fuel cells in 2009 with its common name, "ENE-FARM". Since then, 50,000 units were already installed and being operated in Japan at the end of 2013. Two fuel cell technologies are available under the scheme, polymer electrolyte fuel cell (PEFC) and solid oxide fuel cell (SOFC); currently the split is around 80% PEFC and 20% SOFC [8]. On the other hand, it has been announced that fuel cell vehicles will be on sale in the USA and in Japan from 2015.

1.1.2 Principle of Fuel Cells

Although electrochemical reactions are dependent on a type of fuel cells, their basic principle and composition are almost the same. Since this thesis is focused on the study of polymer electrolyte fuel cells (PEFCs), PEFC is used as an example to explain the principle of fuel cells.

Fuel cells are generally composed by two electrodes (anode and cathode) and electrolyte. Typical reactions occurring in PEFC are shown in Figure 1.3.

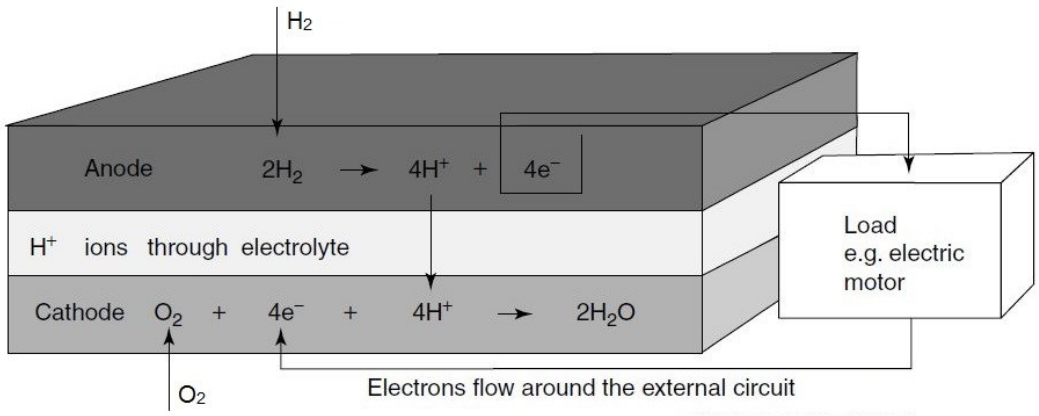

Figure 1.3 Reactions and charge flow for PEFC [9].

Hydrogen and oxygen are the reactants (fuels). Hydrogen at the anode is oxidized into proton (H^+) and electrons are released. These electrons move through external circuit towards the cathode, reduce oxygen, and produce the electrical current and water.

The basic fuel cell reactions are in the following.

At the anode:

$$2H_2 \rightarrow 4H^+ + 4e^- \quad (1.1)$$

At the cathode:

$$O_2 + 4H^+ + 4e^- \rightarrow 2H_2O \quad (1.2)$$

Overall:

$$2H_2 + O_2 \rightarrow 2H_2O \quad (1.3)$$

The reaction comprises four important steps [10]:

1. Reactant delivery (transport) into the fuel cell.
2. Electrochemical reaction.
3. Ionic conduction through the electrolyte and electron conduction through the external circuit.
4. Product removal from the fuel cell.

Unlike battery, electrical energy can be obtained continually with the continuous supply of fuels and oxidants to fuel cells.

1.1.3 Energy and the Reversible OCV of Fuel Cells

Energy considerations for fuel cells are difficult to visualize. The inputs and outputs of fuel cells are summerized in Figure 1.4 [9].

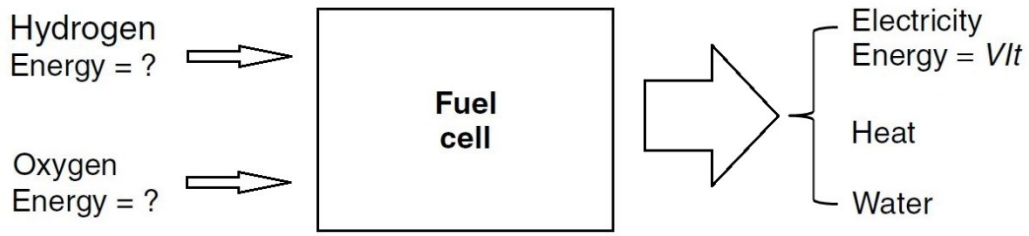

Figure 1.4 Fuel cell inputs and outputs [9].

Even though the electrical power and energy output are easily calculated, power = VI and energy = VIt, the energy of the chemical input and output is not so easily defined and the Gibbs free energy of formation, ΔG_f, is necessary to concern the energy. The ΔG_f is the difference between the Gibbs free energy of the products and the Gibbs free energy

of the inputs or reactants.

$$\Delta G_f = G_f \text{ of products} - G_f \text{ of reactants} \quad (1.4)$$

To consider these quantities in their "per mole" form, these are indicated by $^{-}$ over the lower case letter, for example, $(\bar{g}_f)_{H_2O}$ is the molar specific Gibbs free energy of formation for water.

Considering the basic reaction for the hydrogen/oxygen fuel cell,

$$2H_2 + O_2 \rightarrow 2H_2O$$

which is equivalent to

$$H_2 + 1/2O_2 \rightarrow H_2O$$

the "product" is one mole of H_2O and the "reactants" are one mole of H_2 and half a mole of O_2. Thus,

$$\Delta\bar{g}_f = \left(\bar{g}_f\right)_{H_2O} - \left(\bar{g}_f\right)_{H_2} - 1/2\left(\bar{g}_f\right)_{O_2} \quad (1.5)$$

The $\Delta\bar{g}_f$ changes with temperature and state (liquid or gas), and $\Delta\bar{g}_f$ for the basic hydrogen fuel cell reaction for a number of different conditions is shown in Table 1.1.

If the process is "reversible", then all this Gibbs free energy is converted into electrical energy although in practice, some energy is also released as heat.

Table 1.1 $\Delta\bar{g}_f$ for the reaction $H_2 + 1/2O_2 \rightarrow H_2O$ at various temperatures [9].

Form of water product	Temperature (°C)	$\Delta\bar{g}_f$ (kJ mol^{-1})
Liquid	25	-237.2
Liquid	80	-228.2
Gas	80	-226.1
Gas	100	-225.2
Gas	200	-220.4
Gas	400	-210.3

If $-e$ is the charge on one electron, then the charge that flows is

$$-2Ne = -2F \text{ coulombs}$$

where N is Avogadro's number, F is the Faraday constant, or the charge on one mole of electrons.

If E is the voltage of the fuel cell, then the electrical work done moving this charge through the external circuit is

$$\text{Electrical work done} = \text{charge} \times \text{voltage} = -2FE$$

If the system is reversible, then this electrical work done will be equal to the Gibbs free energy released $\Delta\bar{g}_f$.

$$\Delta\bar{g}_f = -2F \cdot E$$

Thus,

$$E = -\frac{\Delta\bar{g}_f}{2F} \tag{1.6}$$

This fundamental equation gives reversible open circuit voltage (OCV) of the hydrogen fuel cell.

For example, a hydrogen fuel cell operating at 80 °C (form of water product is gas) has $\Delta\bar{g}_f$= −226.1 kJ, and so

$$E = \frac{226100}{2\times 96485} = 1.17 \text{ V}$$

Since $\Delta\bar{g}_f$ changes with temperature and also with reactant pressure and concentration. Using thermodynamic arguments (Balmer, 1990), hydrogen fuel cell reaction can be shown as

$$\Delta\bar{g}_f = \Delta\bar{g}_f^{\,0} - RT\ln\left(\frac{a_{H_2}\cdot a_{O_2}^{\frac{1}{2}}}{a_{H_2O}}\right) \tag{1.7}$$

where a is activity, $\Delta\bar{g}_f^{\,0}$ is the quantity given in Tables 1.1. We can see that if the activity of the reactants increases, $\Delta\bar{g}_f$ becomes more negative, that is, more energy is released. On the other hand, if the activity of the product increases, $\Delta\bar{g}_f$ becomes less negative, and less energy is released. To see how this equation affects voltage, equation 1.7 is substituted into equation 1.6

$$E = \frac{-\Delta \bar{g}_f^0}{2F} + \frac{RT}{2F} \ln\left(\frac{a_{H_2} \cdot a_{O_2}^{\frac{1}{2}}}{a_{H_2O}}\right)$$

$$= E^0 + \frac{RT}{2F} \ln\left(\frac{a_{H_2} \cdot a_{O_2}^{\frac{1}{2}}}{a_{H_2O}}\right) \quad (1.8)$$

where E^0 is the reversible open circuit voltage at the standard pressure, is obtained.

If it is assumed that the gas behaves as an ideal gas and all the pressures are given in bar, the equation simplifies to

$$E = E^0 + \frac{RT}{2F} \ln\left(\frac{P_{H_2} \cdot P_{O_2}^{\frac{1}{2}}}{P_{H_2O}}\right) \quad (1.9)$$

This equation is a form of the Nernst equation. It provides a theoretical basis and a quantitative indication for a large number of variables in fuel cell design and operation. In nearly all cases the pressures in equation 1.9 will be partial pressures, that is, the gases will be part of a mixture.

1.1.4 Efficiency of Fuel Cells

In order to compare the electrical energy produced with the heat by burning the fuel, the calorific value, which is the change in "enthalpy of formation", is used. Its symbol is $\Delta \bar{h}_f$. As with the Gibbs free energy, the convention is that $\Delta \bar{h}_f$ is negative when energy is released. To get a good comparison with other fuel-using technologies, the efficiency of the fuel cell is usually defined as

$$\frac{\text{electrical energy produced per mole of fuel}}{-\Delta \bar{h}_f} \quad (1.10)$$

There are two possible values for $\Delta \bar{h}_f$. For the "burning" of hydrogen

$$H_2 + 1/2O_2 \rightarrow H_2O \text{ (gas)}$$

$$\Delta \bar{h}_f = -241.83 \text{ kJ mol}^{-1}$$

whereas if the product water is condensed back to liquid, the reaction is

$$H_2 + 1/2O_2 \rightarrow H_2O \text{ (liquid)}$$

$$\Delta\bar{h}_f = -285.84 \text{ kJ mol}^{-1}$$

The difference between these two values for $\Delta\bar{h}_f$ (44.01 kJ mol^{-1}) is the molar enthalpy of vaporization of water. The higher value is called the higher heating value (HHV), and the lower value is called the lower heating value (LHV). If this information is not given, the LHV has probably been used, since this will give a higher efficiency number.

The maximum electrical energy available is equal to the change in Gibbs free energy, so

$$\text{Maximum efficiency possible} = \frac{\Delta\bar{g}_f}{\Delta\bar{h}_f} \times 100\% \qquad (1.11)$$

For example, a hydrogen fuel cell operating at 80 °C (form of water product is liquid) has $\Delta\bar{g}_f = -228.2$ kJ, so

Maximum efficiency possible (%) = (−228200) / (−285840) = 80% (HHV basis)

As a result, the fuel cells yield higher efficiency compared with that of heat engine [11].

1.1.5 Fuel Cell Irreversibilities – Causes of Voltage Drop

Theoretical OCV is about 1.2 V for a hydrogen fuel cell operating below 100 °C. However, in reality the voltage is often less than this value. Figure 1.5 shows the performance of a typical PEFC operating at 80 °C, at a normal air pressure.

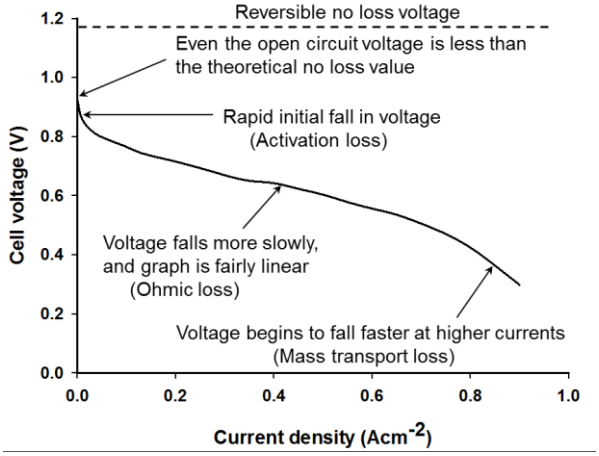

Figure 1.5 A graph showing the voltage for a typical polymer electrolyte fuel cell.

The key points to notice about this graph are as follows:

- Even the open circuit voltage is less than the theoretical value.
- There is a rapid initial fall in voltage.
- The voltage then falls less rapidly, and more linearly.
- There is sometimes a higher current density at which the voltage falls rapidly.

The characteristic shape of Figures 1.5 results from four major irreversibilities [9]. The kind of losses is defined in the following.

1. Activation losses

These are caused by the slowness of the reactions taking place on the surface of the electrodes. A proportion of the voltage generated is lost in driving the electrochemical reaction that transfers the electrons to or from the electrode. This voltage drop is highly non-linear.

2. Fuel crossover and internal current losses

This energy loss results from the waste of fuels passing through the electrolyte, and, to a lesser extent, from electron conduction through the electrolyte. However, a certain amount of fuel diffusion and electron flow will always be possible. Except for the case of direct methanol fuel cells, the fuel loss and internal current are small, and such effect is usually not very important. However, it does have a marked effect on the OCV of low-temperature fuel cells.

3. Ohmic losses

This voltage drop is the straightforward resistance to the flow of electrons through the material of the electrodes and the various interconnectors, as well as the resistance to the flow of ions through the electrolyte. This voltage drop is essentially proportional to current density, linear, and so is called ohmic losses, or sometimes as resistive losses.

4. Mass transport or concentration losses

These result from the change in concentration of the reactants at the surface of the electrodes as the fuel is used. We have seen in section 1.1.3 that concentration affects voltage, and so this type of irreversibility is sometimes called concentration loss. Since the reduction in concentration is caused by an insufficient transport of the reactants to the electrode surface, this type of loss is often called mass transport loss.

1.1.6 Types of Fuel cells

Fuel cells are usually distinguished by the electrolyte in use. Basic information is given in Table 1.2.

Table 1.2 Different types of fuel cells [9].

Fuel cell type	Mobile ion	Operating temperature	Applications and notes
Alkaline (AFC)	OH^-	50 – 200 °C	Used in space vehicles, e.g. Apollo, Shuttle.
Polymer electrolyte (PEFC)	H^+	30 – 100 °C	Vehicles and mobile applications, and for lower combined heat and power (CHP) systems.
Direct methanol (DMFC)	H^+	20 – 90 °C	Suitable for portable electronic systems of low power, running for a long time.
Phosphoric acid (PAFC)	H^+	~ 220 °C	Large numbers of 200-kW CHP systems in use.
Molten carbonate (MCFC)	CO_3^{2-}	~ 650 °C	Suitable for medium- to large-scale CHP systems, up to MW capacity.
Solid oxide (SOFC)	O^{2-}	500 – 1000 °C	Suitable for all sizes of CHP systems, 1 kW to multi-MW.

The polymer electrolyte fuel cell (PEFC) capitalizes on the essential simplicity of the fuel cell. The electrolyte is a solid polymer in which protons are mobile. These cells run at quite low temperatures, so the problem of slow reaction rates is addressed by using sophisticated catalysts and electrodes. PEFCs are a promising candidate for automotive applications, but also for stationary power generation.

One theoretically very attractive solution to the hydrogen supply problem is to use methanol as a fuel instead. This can be done in the PEFC, and such cells are called direct methanol fuel cell (DMFCs). However, these cells exhibit low power output, but there are many potential applications in the rapidly growing area of portable electronics equipment.

Although PEFCs were used on the first manned spacecraft, the alkaline fuel cell (AFC) was used on the Apollo and Shuttle Orbiter craft. The problem of slow reaction rate is overcome by using highly porous electrodes with a platinum catalyst, and sometimes by operating at quite high pressures. Although some historically important alkaline fuel cells have operated at about 200 °C, they are usually operated below 100 °C. The main problem of AFCs is that the air and fuel supplies must be free from CO_2, and so pure oxygen and hydrogen must be used.

The phosphoric acid fuel cell (PAFC) was the first fuel cell to be produced in commercial quantities and widespread terrestrial use. Many 200- kW systems (UTC Fuel Cells) are installed in the USA and Europe, as well as systems are produced by a Japanese company, Fuji Electric. Porous electrodes, platinum catalysts, and a fairly high temperature (~220 °C) are used to increase the reaction rate to a reasonable level.

The solid oxide fuel cell (SOFC) operates in the region of 600 to 1000 °C. This means that high reaction rates can be achieved without expensive catalysts, so that gases such as natural gas can be directly used owing to the ability of internal reforming. This fuel cell type thus addresses all the problems and takes full advantage of the inherent simplicity of the fuel cell concept. Nevertheless, the ceramic materials, which are the main component, are difficult to handle, so they are expensive to be manufactured.

Similar to SOFC, molten carbonate fuel cell (MCFC) can use gases such as methane and coal gas directly, without an external reformer. However, the operation condition is very much limited. Since the electrolyte is composed by a hot and corrosive mixture of lithium, potassium, and sodium carbonates, operating temperatures are limited between 600 °C and 700 °C, where the carbonates form a highly conductive molten salt and carbonate ions provide ionic conductivity.

1.2 Polymer Electrolyte Fuel Cells (PEFCs)

1.2.1 Characteristics of PEFCs

PEFCs are also called PEM fuel cells (PEMFCs) since the electrolyte membrane used in PEFC is named as proton exchange membrane or polymer electrolyte membrane (PEM). PEFCs are attractive power devices for both stationary and automobile applications owing to the following advantages.

- ✧ Solid electrolyte: easy to handle.
- ✧ Low operation temperature: good start-stop capability.
- ✧ Higher power density.
- ✧ High efficiency.
- ✧ Zero CO_2 emissions.

However, they also have disadvantages:

- Expensive materials: platinum catalyst, polymer electrolyte membrane.
- Essential water management.
- Poor tolerance to contaminants.

A fuel cell stack consists of a multitude of single cells stacked up so that the cathode of one cell is electrically connected to the anode of the adjacent cell. Figure 1.6 shows a typical single cell.

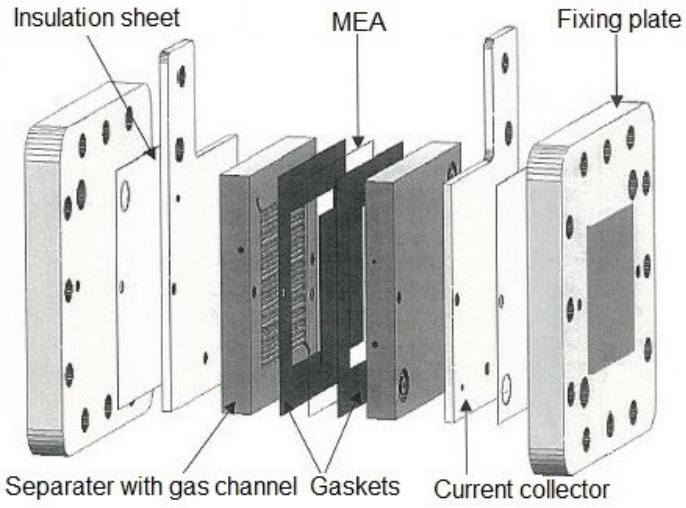

Figure 1.6 Components of a single PEFC.

A single cell is composed of fixing plate, current collector, separator with gas channel, gaskets and MEA. Fixing plate with bolts provides good sealing for the cell. For generating electricity, current collector is used, and separated from fixing plate by insulation sheet. Separator is also called as bipolar plates, designed with channels for the distribution of reactants over the electrode surfaces and also for the successful water drain. They are typical made from graphite. Gaskets are used to prevent gases from leaking.

The heart of the PEFC is the membrane electrode assembly (MEA), which has the most important function on the performance of fuel cells. As shown in Figure 1.7, MEA consists of a proton exchange membrane, catalyst layers, and gas diffusion layers (GDL). Typically, these components are fabricated individually and then pressed together at high temperatures and pressures.

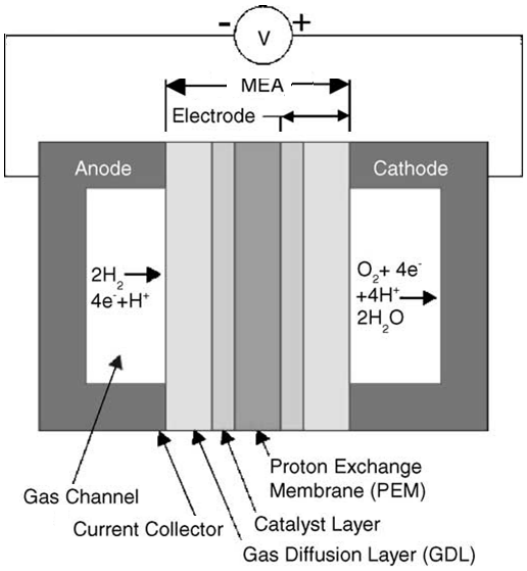

Figure 1.7 A schematic diagram of a typical MEA.

1.2.2 Electrodes for PEFCs

Among these components in MEA, catalyst layer is the most important component, which controls the reaction kinetics. Therefore, considerable efforts have been made for the research of electrocatalysts for PEFCs. To date, platinum-based nanoparticles dispersed on high surface area carbon support are still the most common electrocatalyst in practical PEFCs [12]. Highly dispersed platinum leads to more platinum exposed to the reactants and considerable increase in power density.

Fuel cell electrodes serve as delivering/collecting electrons and also reactant/product species. This requires for electrodes to simultaneously provide high electrical conductivity, high porosity, and of course, high catalytic activity. In effective electrode, the required transport processes, proton, electron, and reactant/product, are totally balanced as shown in Figure 1.8. The ideal catalyst layer should be thin enough to reduce transfer loss.

The site where protons, electrons, and reactant can meet is often referred to the three phase boundary in the catalyst layer. Development of effective three phase boundaries, where reactions are proceeded, is the most challenging part for the PEFC electrode.

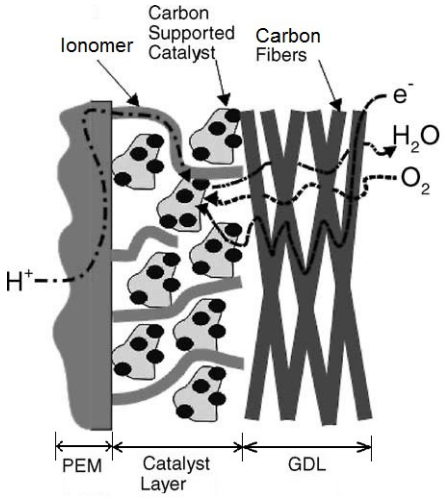

Figure 1.8 Transport of gases, protons, and electrons at cathode layer [13].

1.2.3 Problems to be Solved

Although PEFCs are already commercialized, there are still some issues to be solved for further improvement and wider commercialization of PEFCs. Durability is one of the most important issues. One critical issue facing is the gradual decline in performance during the operation, mainly caused by the loss of the electrochemical surface area (ECA) of carbon supported platinum nanoparticles at the cathode. The major reasons for the degradation of the cathodic catalyst layer are platinum growth or dissolution and carbon corrosion under the potential change especially for automobile application [14-16].

In general, carbon black materials with high surface area, such as Vulcan and Ketjen Black, are commonly used as supports for platinum catalysts for PEFCs, leading to well dispersing small platinum particles and maximizing their catalytic surface area. However, their durability under chemically and electrochemically oxidizing conditions needs further improvement [17].

The mechanism and kinetics of electrochemical oxidation of carbon as a function of potential have mainly been investigated using potentiostatic experiments in phosphoric acid [18], and are described as

$$C + 2H_2O \rightarrow CO_2 + 4H^+ + 4e^- \qquad E = 0.207 \text{ V (vs. RHE)} \qquad (1.12)$$

The generation of CO_2 is believed to proceed through the intermediate formation of carbon surface oxides, as suggested in earlier studies in phosphoric acid fuel cells [19].

Formation of surface oxides on Vulcan is reported at potentials higher than 1.0 V at room temperature [20].

In reality, carbon corrosion is a serious problem for fuel cell vehicle (FCV) since the local cathode potential can reach to as high as 1.5 V during the start-up and shut-down operations, resulting in significant acceleration of carbon corrosion [16, 21-23].

When carbon oxidation occurs under the high potential, migration and agglomeration of platinum particles, and finally the detachment from the carbon supports are resulted as shown in Figure 1.9. All these phenomena negatively contribute to PEFC performance [14-15, 24-28].

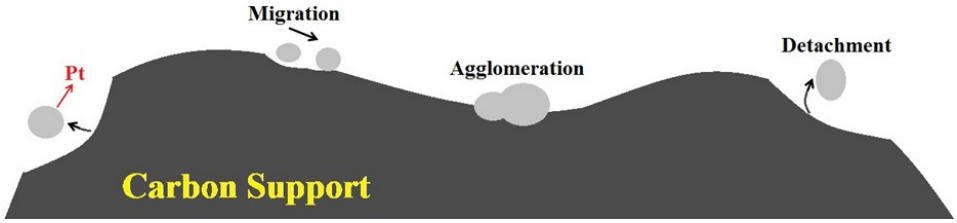

Figure 1.9 Diagram of the fuel cell degradation derived by carbon corrosion.

1.2.4 Recent Research Trend against Carbon Corrosion Problems

To resolve the problem of carbon corrosion, development of either carbon supports with high corrosion resistance or metal oxide supports without using carbon becomes a common possible solution.

Regarding to carbon supports with high corrosion resistance, it is well known that carbon with graphitic surface has high durability against corrosion. Usage of carbon materials with a higher graphitic character, such as carbon nanotubes [17, 29-30] and graphene [31-33], leads to higher durability than carbon black. Heat treatment of carbon materials without originally having the graphitic nanostructures, such as carbon black, results in formation of graphitized carbon surface and improves the carbon corrosion resistance [34-35]. Furthermore, many researchers have synthesized mesoporous carbon [36], carbon nanocage [37], carbon nanofiber (CNF) [38] or other carbon nanomaterials [39-41] with surface graphite structure and have used them as carbon supports with high corrosion resistivity.

On the other hand, metal oxide supports are known to stable against oxidation since they are already fully oxidized. Oxides with many metals, such as Au, Pt, Ir, Ru, Ta, Ti,

Sn, etc., are stable at actual fuel cell environment [42]. Among those oxides, SnO_2 and TiO_2 are widely investigated toward the improvement on durability [43-50]. Also, much research work has been reported on developing high activity and high durability oxides by controlling the nanostructures of oxides, such as hollow nanostructure [51-52], nanofiber [53-54], nanotube [55], etc. Furthermore, with the consideration of increasing the conductivity of oxides, many studies using composites of oxide and carbon as supports, for example, carbon with silica [56-58] or with titania [59-62], have been reported, showing almost the same activity but increased durability compared to carbon supports.

1.3 Objective of This Study

In this study, we have focused on graphitic structure of carbon, which is known to have resistance to carbon corrosion. The aim of the study is proposing nanostructure of carbon supports with high corrosion resistance through the systematic heat treatment of commercially available carbon black materials. Through the heat treatment, carbon surface is graphitized, leading to increase in corrosion resistance. However, highly graphitized smooth carbon surface most likely leads to an increase in the mobility of platinum particles on carbon support at the same time, similar to the case of carbon nanotubes [63]. Therefore, in this study we have challenged to investigate an optimum condition, which can simultaneously achieve high carbon corrosion resistance and good interaction between platinum particles and carbon supports. We have further aimed to understand possible degradation mechanisms of electrocatalysts using various techniques including electrochemical and electron-microscopic methods.

References

[1] F. Barbir, PEM Fuel Cells: Theory and practice, Elsevier Academic Press, 2005.

[2] W. R., Grove, On voltaic series and the combination of gases by platinum, London and Edinburgh philosophical Magazine and Journal of science, Series 3, 14 (1839) 127-130-420.

[3] U. Bossel, The birth of the fuel cell, European Fuel Cell Forum, Oberrohrdorf, Switzerland, 2000, 1835.

[4] W. R., Grove, On a gaseous voltaic battery, London and Edinburgh Philosophical Magazine and Journal of Science, Series 3, 21 (1842) 417-420.

[5] E. Chen, Fuel cell technology handbook, CRC Press, Boca Raton, FL, 2003.

[6] M. Nadal, F. Barbir, Development of a hybrid fuel cell/battery powered electric vehicle, Hydrogen Energy Progress X, 1994, 1427.

[7] C. Stone, A.E. Morrison, From curiosity to "Power to change the world", Solid State Ionics, Vol. 152-153 (2002) 1.

[8] Fuel Cell Today, http://www.fuelcelltoday.com.

[9] J. Larminie and A. Dicks, Fuel cell systems explained (Second Edition), Wiley: UK, 2003.

[10] Ryan P. O`Hayre et al., Fuel cell fundamentals, John Wiley & Sons, New York, 2009.

[11] R. W. Glazebrook, Efficiencies of heat engines and guel cells: The methanol fuel cell as a competitor to otto and diesel engine, J. Power Sources, 7 (1982) 215.

[12] H. A. Gasteiger, S. S. Kocha, B. Sompalli and F. T. Wagner, Activity benchmarks and requirements for Pt, Pt-alloy, and non-Pt oxygen reduction catalysts for PEMFCs, Appl. Cat. B: Enviro., 56 (2005) 9.

[13] S. Litster, G. McLean, PEM fuel cell electrodes, J. Power Sources, 130 (2004) 61.

[14] J. Willsau, J. Heitbaum, The influence of Pt-activation on the corrosion of carbon in gas diffusion electrodes-a DEMS study, J. Electroanal. Chem., 161 (1984) 93.

[15] J.P. Meyers, R.M. Darling, Model of carbon corrosion in PEM fuel cells, J. Electrochem. Soc., 153 (2006) A1432.

[16] C.A. Reiser, L. Bregoli, T.W. Patterson, J.S. Yi, J.D. Yang, M.L. Perry, T.D. Jarvi, A reverse-current decay mechanism for fuel cells, Electrochem. Solid-State Lett., 8 (2005) A273.

[17] Y. Shao, G. Yin, J. Zhang, Y. Gao, Comparative investigation of the resistance to electrochemical oxidation of carbon black and carbon nanotubes in aqueous sulfuric acid solution, Electrochim. Acta, 51 (2006) 5853.

[18] K. Kinoshita, Carbon: Electrochemical and physicochemical properties, John Wiley & Sons, New York, 1988.

[19] K. Kinoshita, J. Bett, Electrochemical oxidation of carbon black in concentrated phosphoric acid at 135 °C, Carbon, 11 (1973) 237.

[20] K. H. Kangasniemi, D. A. Condit, T. D. Jarvi, Characterization of Vulcan electrochemically

oxidized under simulated PEM fuel cell conditions, J. Electrochem. Soc., 151 (4) (2004) 125.

[21] L.C. Colmenares, A. Wurth, Z. Jusys, R.J. Behm, Model study on the stability of carbon support materials under polymer electrolyte fuel cell cathode operation conditions, J. Power Sources, 190 (2009) 14.

[22] A. Ohma, K. Shinohara, A. Liyama, T. Yoshida, A. Daimaru, Membrane and catalyst performance targets for automotive fuel cells by FCCJ membrane, catalyst, MEA WG, ECS Trans., 41 (2011) 775.

[23] T.J. Schmidt, High-temperature PEFCs: durability insights, in: F.N. Buechi, M. Inaba, T.J. Schmidt (Eds.), Polymer Electrolyte Fuel Cell Durability, Springer, NY, 2009, pp. 199.

[24] A.L. Dicks, The role of carbon in fuel cells, J. Power Sources, 156 (2006) 128.

[25] R. Borup, et al., Scientific aspects of polymer electrolyte fuel cell durability and degradation (Review), Chem. Rev., 107 (2007) 3904.

[26] P.J. Ferreira, G.J. La O', Y. Shao-Horn, D. Morgan, R. Makharia, S. Kocha, H.A. Gasteiger, Instability of Pt/C electrocatalysts in proton exchange membrane fuel cells: A mechanistic investigation, J. Electrochem. Soc., 152 (2005) A2256.

[27] K.J.J. Mayrhofer, S.J. Ashton, J.C. Meier, G.K.H. Wiberg, M. Hanzlik, M. Arenz, Non-destructive transmission electron microscopy study of catalyst degradation under electrochemical treatment, J. Power Sources, 185 (2008) 734.

[28] S. Maass, F. Finsterwalder, G. Frank, R. Hartmann, C. Merten, Carbon support oxidation in PEM fuel cell cathodes, J. Power Sources, 176 (2008) 444.

[29] L. Li, Y. Xing, Electrochemical durability of carbon nanotubes in noncatalyzed and catalyzed oxidations, J. Electrochem. Soc., 153 (2006), A1823.

[30] L. Li, Y. Xing, Electrochemical durability of carbon nanotubes at 80 °C, J. Power Sources, 178 (2008) 75.

[31] E. Antolini, Graphene as a new carbon support for low-temperature fuel cell catalysts, Applied Catalysis: Enviromental, 123-124 (2012) 52.

[32] Y. Li, Y. Li, E. Zhu, T. McLouth, C. Chiu, X. Huang, Y. Huang, Stabilization of high-performance oxygen reduction reaction Pt electrocatalyst supported on reduced graphene oxide/carbon black composite, J. Am. Chem. Soc., 134 (2012) 12326.

[33] H. Wu, D. Wexler, H. Liu, Durability investigation of graphene-supported Pt nanocatalysts for PEM fuel cells, J. Solid State Electrochem., 15 (2011) 1057.

[34] M. Hara, M. Lee, C. Liu, B. Chen, Y. Yamashita, M. Uchida, H. Uchida, M. Watanabe, Electrochemical and Raman spectroscopic evaluation of Pt/graphitized carbon black catalyst durability for the start/stop operating condition of polymer electrolyte fuel cells, Electrochim. Acta, 70 (2012) 171.

[35] H. Yano, T. Akiyama, P. Bele, H. Uchida, M. Watanabe, Durability of Pt/graphitized carbon catalysts for the oxygen reduction reaction prepared by the nanocapsule method, Phys. Chem.

Chem. Phys., 12 (2010) 3806.

[36] P.V. Shanahan, L. Xu, C. Liang, M. Waje, S. Dai, Y.S. Yan, Graphitic mesoporous carbon as a durable fuel cell catalyst support, J. Power Sources, 185 (2008) 423.

[37] B. Xia, J. Wang, S. Teng, X. Wang, Durability improvement of a Pt catalyst with the use of a graphitic carbon support, Chem. Euro. J., 16 (2010) 8268.

[38] D. Sebastián, A. G. Ruíz, I. Suelves, R. Moliner, M. J. Lázaro,V. Baglio, A. Stassi, A. S. Aricò, Enhanced oxygen reduction activity and durability of Pt catalysts supported on carbon nanofibers, Appl. Catal. B: Environ., 115-116 (2012) 269.

[39] S. Sharma, B. G. Pollet, Support materials for PEMFC and DMFC electrocatalysts-A review, J. Power Sources, 208 (2012) 96.

[40] C. Wang, N.V. Dale, K. Adjemlan, Rotating disk electrode investigation of Pt/Carbon electrocatalyst activity and durability, ECS Trans., 41 (2011) 2245.

[41] S.K. Natarajan, J. Hamelin, Electrochemical durability of carbon nanostructures as catalyst support for PEMFCs, J. Electrochem. Soc., 156 (2009) B210.

[42] K. Sasaki, F. Takasaki, Z. Noda, S. Hayashi, Y. Shiratori, K. Ito, Alternative electrocatalyst support materials for polymer electrolyte fuel cells, ECS Trans., 33 (2010) 473.

[43] T. Ioroi, Z. Siroma, N. Fujiwara, S. Yamazaki, K. Yasuda, Sub-stoichiometric Titanium oxide-supported platinum electrocatalyst for polymer electrolyte fuel cells, Electrochem. Comm., 7 (2005) 183.

[44] M. Nakada, A. Ishihara, S. Mitsushima, N. Kamiya, K. Ota, Effect on tin oxides on oxide formation and reduction of platinum particles, Electrochem. Solid-State Lett., 10 (2007) F1.

[45] W. S. Baker, J. J. Pietron, M. E. Teliska, P. J. Bouwman, D. E. Ramaker, K. E .Swider-Lyons, Enhanced oxygen reduction activity in acid by Tin-oxide supported Au Nanoparticle catalysts, J. Electrochem. Soc., 153 (2006) A1702.

[46] T. Takeguchi, Y. Anzai, R. Kikuchi, K. Eguchi, W. Ueda, Preparation and characterization of CO -tolerant Pt and Pd anodes modified with SnO_2 nanoparticles for PEFC, J. Electrochem. Soc. 154 (2007) B1132.

[47] A. Masao, Z. Noda, F. Takasaki, K. Ito, K. Sasaki, Carbon-free Pt electrocatalysts supported on SnO_2 for polymer electrolyte fuel cells, Electrochem. Solid-State Lett., 12 (2009) B119.

[48] F. Takasaki, S. Matsuie, Y. Takabatake, Z. Noda, A. Hayashi, Y. Shiratori, K. Ito, K. Sasaki, Carbon-free Pt electrocatalysts supported on SnO_2 for polymer electrolyte fuel cells: electrocatalytic activity and durability, J. Electrochem. Soc., 158 (2011) B1270.

[49] K. Kakinuma, M. Uchida, T. Kamino, H. Uchida, M. Watanabe, Synthesis and electrochemical characterization of Pt catalyst supported on $Sn_{0.96}Sb_{0.04}O_{2-\delta}$with a network structure, Electrochimica Acta, 56 (2011) 2881.

[50] S. Y. Huang, P. Ganesan, B. N. Popov, Electrocatalytic activity and stability of Titania-supported Platinum–Palladium electrocatalysts for polymer electrolyte membrane fuel cell, ACS Catal., 2

(2012) 825.

[51] P. Zhang, S.Y. Huang, B.N. Popov, Mesoporous Tin oxide as an oxidation-resistant catalyst support for proton exchange membrane fuel cell, ECS Trans., 157 (2010) B1163.

[52] S. Sun, G. Zhang, X. Sun, M. Cai, M. Ruthkosay, J. Nanotech., 2012 (2012) 389595.

[53] K. Senevirathne, R. Hui, S. Campbell, S. Ye, J. Zhang, Electrocatalytic activity and durability of Pt/NbO_2 and Pt/Ti_4O_7 nanofibers for PEM fuel cell oxygen reduction reaction, Electrochim. Acta, 59 (2012) 538.

[54] C. Yao, F. Li, X. Li, D. Xia, Fiber-like nanostructured Ti_4O_7 used as durable fuel cell catalyst support in oxygen reduction catalysis, J. Mater. Chem., 22 (2012) 16560.

[55] D. H. Lim, W. J. Lee, N. L. Macy, W. H. Smyrl, Electrochemical durability investigation of Pt/TiO_2 nanotube catalysts for polymer electrolyte membrane fuel cells, Electrochem. Solid-State Lett., 12 (2009) B123.

[56] S. Takenaka, H. Matsumori, H. Matsune, E. Tanabe, M. Kishida, High durability of carbon nanotube-supported Pt electrocatalysts covered with Silica layers for the cathode in a PEMFC, J. Electrochem. Soc., 155 (2008) B929.

[57] T. Kinumoto, K. Nagano, T. Tsumura, M. Toyoda, A novel durable electrode catalyst of Pt/Ketjen black decorated with SnO_2 nanoparticles for polymer electrolyte fuel cells, Electrochemistry, 79 (2011) 334.

[58] R. Wang, X. Li, H. Li, Q. Wang, H. Wang, W. Wang, J. Kang, Y. Chang, Z. Lei, Highly stable and effective Pt/carbon nitride (CNx) modified SiO_2 electrocatalyst for oxygen reduction reaction, Inter. J. Hydrogen Energy, 36 (2011) 5775.

[59] K. Huang, K. Sasaki, R. R. Adzic, Y. Xing, Increasing Pt oxygen reduction reaction activity and durability with a carbon-doped TiO_2 nanocoating catalyst support, J. Mater. Chem., 22 (2012) 16824.

[60] Y. Bing, V. Neburchilov, C. Song, R. Baker, A. Guest, D. Ghosh, S. Ye, S. Campbell, J. Zhang, Effects of synthesis condition on formation of desired crystal structures of doped-TiO_2/carbon composite supports for ORR electrocatalysts, Electrochim. Acta, 77 (2012) 225.

[61] A. Bauer, R. Hui, A. Ignaszak, J. Zhang, D.J. Jones, Application of a composite structure of carbon nanoparticles and N_b-TiO_2 nanofibers as electrocatalyst support for PEM fuel cells , J. Power Sources, 210 (2012) 15.

[62] Z. Z. Jiang, Z. B. Wang, W. L. Qu, D.M. Gu, G.P. Yin, Synthesis and characterization of carbon riveted Pt/MWCNTs@TiO_2-TiC catalyst with high durability for PEMFCs application, Appl. Catal. B: Environ., 123-124 (2012) 214.

[63] M. Okamoto, T. Fujigaya, N. Nakashima, Design of an assembly of poly(benzimidazole), carbon nanotubes, and Pt nanoparticles for a fuel-cell electrocatalyst with an ideal interfacial nanostructure, Small, 5 (2009) 735.

Chapter 2

Experimental

2.1 Materials

All the chemicals were used as received without further purification. Dichloromethane, 2-propanol, and 5% Nafion® dispersion solution DE521 CS type (for half-cell test) were purchased from WAKO. Platinum (II) acetylacetonate and 5% Nafion® solution (for full-cell test) were obtained from ALDRICH. Perchloric acid, Ethanol, Vulcan XC-72, Ketjen Black EC600-JD, and standard silicon StanSil-G03A were obtained from KANTO CHEMICAL, KISHIDA CHEMICAL, Cabot Corp., Lion Corp., and OSAKA YAKKEN, respectively. MilliQ water was used in all cases.

2.2 Preparation and Characterization of Carbon Supports

2.2.1 Carbon Supports Used in This Study

For the carbon sources, two kinds of traditional and commercially available materials, Vulcan XC-72 and Ketjen Black EC600-JD, were selected in this study. Both Vulcan and Ketjen Black were commonly used as supports for platinum catalysts for PEFCs since they are commercialized and have high specific surface area. Usage of such carbon materials leads to well dispersing small platinum particles and maximizing their catalytic surface area, conductivity, and electrochemical stability under usual fuel cell operating conditions [1-2]. TEM images (Figure 2.1) show the nanostructure of these two carbon materials. Vulcan is made of amorphous carbon nanoparticles of 30 – 60 nm in diameter. The specific surface area is usually around 200 m^2g^{-1}. On the other hand, Ketjen black has similar particle size but higher specific surface area because of its hollow structure. The specific surface area is typically over 1200 m^2g^{-1}.

2.2.2 Heat Treatment

With the aim of graphitizing the surface of carbon materials, Vulcan and Ketjen Black were heat treated at three different temperatures (1100 °C, 1600 °C, and 2000 °C) (Table 2.1). Heat treatment at 1100 °C was performed under nitrogen (G1 grade) flow by heating from room temperature at 20 °C min^{-1} and then keeping at 1100 °C for 3h, using an infrared lamp heating equipment (ULVAC-RIKO, SSA-E45P). Heat treatments at 1600 °C and 2000 °C were done under argon (G1 grade) flow by heating from room temperature at 20 °C min^{-1} and 40 °C min^{-1}, respectively, and then keeping at 1600 °C and 2000 °C, respectively, for 3h using a high frequency induction heating equipment (SK MEDICAL, MU-1700D). Graphitized Vulcan at different temperatures was denoted as GVC1100, GVC1600, and GVC2000, respectively. Similarly for Ketjen Black, they were denoted as GKB1100, GKB1600, and GKB2000, respectively. With adding non heat-treated Vulcan and Ketjen Black, VC and KB, eight kinds of carbon materials were used for this study.

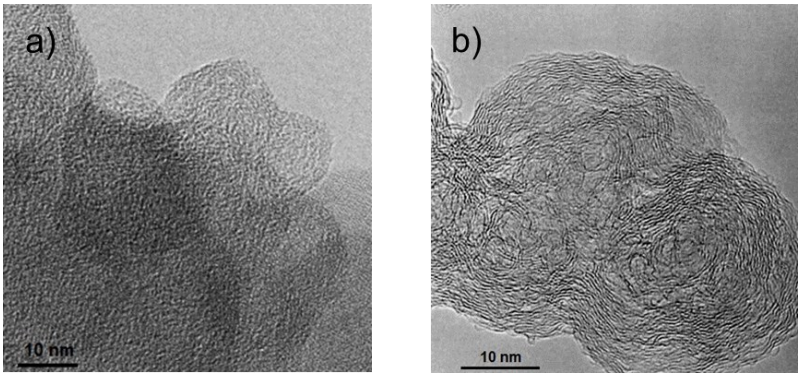

Figure 2.1 TEM images of Vulcan XC-72 (a) and Ketjen Black (b).

Table 2.1 Heat treatments of Vulcan and Ketjen Black.

Heat-treated temperature	Heat-treated condition	Carbon materials obtained
1100 °C	N_2, 20 °C /min, 3h	GVC1100, GKB1100
1600 °C	Ar, 20 °C /min, 3h	GVC1600, GKB1600
2000 °C	Ar, 40 °C /min, 3h	GVC2000, GKB2000

2.2.3 Specific Surface Area by Nitrogen Adsorption Measurement

Specific surface area of carbon materials was calculated by the method developed by Brunauer, Emmett, and Teller (BET) [3] based on nitrogen adsorption measurement using BELSORP-mini (BEL Japan, Inc.). This is a method by which physical adsorption

of gas molecules conclude the surface area of a sample from the quantity of molecules adsorbed. Measurement was started with the pre-treating of carbon materials at 200 °C for 2 h under vacuum to remove the water vapor adsorbed on the materials. Glass cells filled with the known amount of each sample were soaked into liquid nitrogen. Adsorption/desorption isotherms were obtained by measuring the amount of gas adsorbed with the increase in relative pressures at a constant temperature (77 K, liquid N_2).

The concept of the BET theory [3] is an extension of the Langmuir theory, which is a theory for monolayer molecular adsorption, to multilayer adsorption with the following hypotheses: (a) gas molecules physically adsorb on a solid in layers infinitely; (b) there is no interaction between each adsorption layer; and (c) the Langmuir theory can be applied to each layer. The resulting BET equation is

$$\frac{P}{V(P_0-P)} = \frac{1}{CV_m} + \frac{C-1}{CV_m} \cdot \frac{P}{P_0} \tag{2.1}$$

where P/P_0 is relative pressure (P and P_0 are the equilibrium and the saturation pressure of adsorbates at the temperature of adsorption, respectively), V is the adsorbed gas quantity, and V_m is the monolayer adsorbed gas quantity. C is the BET constant.

When multiply V_m with the surface area that one molecule occupies when N_2 molecules covered on sample surface, the total surface area of the sample is obtained. Specific surface area is then determined by total surface area divided by sample weight.

2.2.4 Graphitization Degree by X-ray Diffraction

In order to evaluate the graphitization degree of carbon materials obtained by heat treatment of Vulcan and Ketjen Black, both measurements and calculations were performed according to JIS R 7651:2007 [4]. Here, JIS R 7651:2007 is particularly made for carbon materials which are relatively graphitized by heat treatment. For the measurements, XRD patterns were obtained using RINT-Ultima Ⅲ (Rigaku Corp.) with a Cu Kα-radiation (λ = 1.54 Å). Silicon powder was mixed into the carbon sample as a standard. The measurement conditions are listed in Table 2.2.

Table 2.2 Measurement conditions of X-ray diffraction for carbon materials.

Voltage / current	40 kV/40 mA	Divergence Slit (DS)	1/3°
Scanning Type	FT	Scatter Length Limit Slit	2 mm
Fixed Time	4 cps	Scatter Slit (SS)	1/3°
Scanning Interval	0.02°	Receiving Slit (RS)	0.30 mm
Scanning Scope	20 ~ 30°	Monochrome Receiving Slit	0.8 mm

For the calculations, Carbon-X, which is a software made based on JIS R 7651:2007, was in use. In this calculation software, diffraction peak profiles are corrected on consideration of Lawrence, polarization, absorption, and carbon atomic scattering. Then, the interlayer spacing d_{002} and the crystallite size L_c (002) of carbon materials are calculated. In this study, graphitization degree is defined as how close the value of d_{002} is to 0.3354 nm, which is the value of d_{002} for graphite.

2.3 Preparation and Characterization of Pt/C Electrocatalysts

2.3.1 Preparation

Pt/C electrocatalysts were prepared by depositing platinum on eight kinds of carbon supports obtained in section 2.2.2. Pt/C electrocatalysts were synthesized using platinum (II) acetylacetonate as a platinum precursor and dichloromethane as a solvent based on the method in the literature [5]. Figure 2.2 shows the flow chart of Pt/C electrocatalyst preparation. Each prepared carbon powder and platinum (II) acetylacetonate were suspended in dichloromethane within the ultrasonic bath, until the solvent were completely removed through evaporation. The obtained black solid was then transferred to the infrared lamp heating equipment, and then heated at 210 °C for 3h and 240 °C for 3h under nitrogen flow to reduce platinum (II) to platinum metal. Consequently, eight different Pt/C electrocatalysts were obtained by this method. For all the Pt/C electrocatalysts, the amount of platinum on carbon was controlled at about 20 wt%.

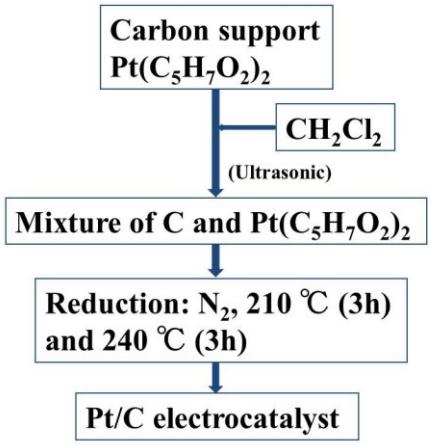

Figure 2.2 Flow chart of Pt/C electrocatalyst preparation.

2.3.2 Platinum Loading by TG Measurement

In order to confirm that if the platinum amount for all the Pt/C electrocatalysts was controlled at about 20 wt% or not, the amount of platinum deposited on carbon supports was quantified from the weight loss during the combustion of Pt/C electrocatalysts up to 800 °C by heating from room temperature at 4 °C min^{-1} under air flow of 30 ml min^{-1} using a thermogravimeter, TG 8120 (Rigaku Corp.).

2.3.3 Platinum Crystallize Size by X-ray Diffraction

The platinum crystallite size of Pt/C electrocatalysts was also derived through X-ray diffraction measurement. The measurement conditions are listed in Table 2.3.

Platinum crystallite size was calculated from the half-maximum width of the platinum diffraction peak (111) using the analysis program named JADE based on the Scherrer's equation [6]:

$$\tau = \frac{K\lambda}{\beta \cos\theta} \tag{2.2}$$

where τ is the mean size of the ordered (crystallite) domains; k is a dimensionless shape factor, with a value close to the unity; λ is the X-ray wavelength; β is the line broadening at half the maximum intensity, after subtracting the instrumental line broadening, in radians; θ is the Bragg angle.

Table 2.3 Measurement conditions of X-ray diffraction for Pt/C electrocatalysts.

Voltage/current	40 kV/40 mA	Divergence Slit (DS)	2/3°
Scanning Type	Continuous Scanning	Scatter Length Limit Slit	10 mm
Scanning Speed	2°/min	Scatter Slit (SS)	2/3°
Scanning Interval	0.01°	Receiving Slit (RS)	0.30 mm
Scanning Scope	10 ~ 90°	Monochrome Receiving Slit	0.8 mm

2.4 Electrochemical Evaluation of Pt/C Electrocatalysts

2.4.1 Three Electrode Set-up

For the evaluation of the Pt/C electrocatalysts prepared for PEFC, the measurement with MEA is effective owing to the true operation environment of experiments. However, for the testing of many kinds of Pt/C electrocatalysts which electrochemical activity and durability are unknown, the test by preparing MEAs will take time and need much more electrocatalysts. Therefore, on the consideration that electrocatalyst of PEFC is used in an acid condition and the operation temperature is relatively low, electrochemical measurement of electrocatalysts are often made as thin-films cast on rotating disk electrodes in liquid electrolyte with a half-cell configuration. This method has been shown to be predictive of the performance trends of practical electrocatalysts in the electrocatalyst coated membranes used in PEFCs [7]. It is a standard procedure to evaluate oxygen reduction reactivity using the rotation disk electrode which is a kind of the convection voltammogram for the study such as development of new cathode electrocatalysts.

Here, electrochemical measurement was also performed in the perchloric acid solution using the three electrode set-up to evaluate the activity, and durability of the eight kinds of electrocatalysts was evaluated. In this study, electrochemical measurements of Pt/C electrocatalysts were performed on the automatic polarization system (Hokuto Denko Corp., HZ-5000) and rotating disk electrode apparatus (Hokuto Denko Corp., HR-500) with a three-electrode set-up (Hokuto Denko Corp., HX-107) (see Figure 2.3).

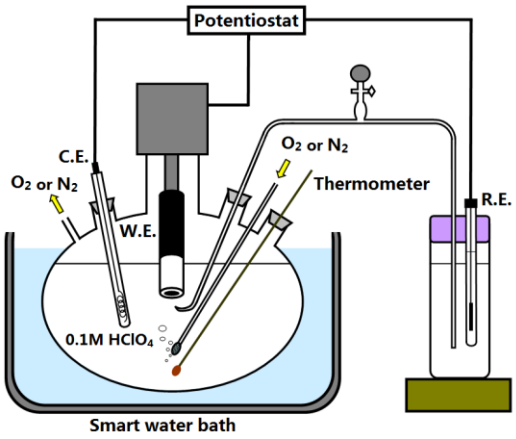

Figure 2.3 Three electrode set-up for the half-cell measurement.

The electrodes prepared were used as the working electrodes. Pt-wire and Ag/AgCl electrode with saturated KCl were both obtained from Hokuto Denko Corporation and used as the counter electrode and the reference electrode, respectively.

All the values of potential were recalculated as volts versus reversible hydrogen electrode (RHE). Electrochemical measurements were performed in a perchloric acid solution (0.1 M $HClO_4$) at 25 °C, and usually under the nitrogen saturated condition using the cyclic voltammetry method. In order to evaluate oxygen reduction reaction (ORR), linear sweep voltammograms (LSVs) were obtained under the oxygen saturated condition with rotating disk electrode (RDE).

2.4.2 Working Electrode

Electrodes were prepared according to the method recommended by Fuel Cell Commercialization Conference of Japan (FCCJ) in 2011[8]. A few milligrams of Pt/C electrocatalyst powder were dispersed in the mixture of ultra-pure water, 2-proponal, and 5% Nafion® dispersion solution (19:6:0.1 volume ratio) and ultrasonically stirred for 30 min using a ultra sonic homogenizer (UH-600, SMT CO., LTD.), in order to obtain a homogeneous suspension. Then, 10 μL of this was cast onto the surface of an Au disk (Hokuto Denko Corp., 0.196 cm^2) and dried at 60 °C for 15 min (Figure 2.4). The platinum amount was kept to 17.3 μg cm^{-2} throughout the experiments.

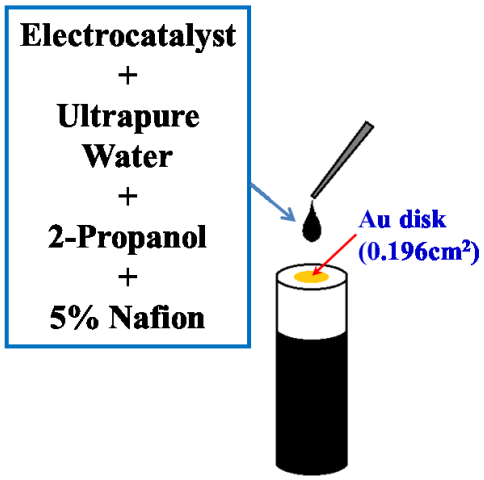

Figure 2.4 Working electrode preparation.

2.4.3 Cyclic Voltammetry

Cyclic voltammetry (CV) is typically used to characterize fuel cell electrocatalysts in more detail. In a standard CV measurement, the potential is swept back and forth between two voltage limits while the current response is measured. The voltage sweep is generally linear with time, and the plot of the resulting current versus voltage is called a cyclic voltammogram.

An illustration of the CV waveform used in this study is provided in Figure 2.5. E_0 is initial potential, after changing potential from E_0 to E_1, and then sweeping it between E_1 and E_2 at the scan rate of 50 mV/s (In this experiment potential is swept from 0.05 V to 1.20 V vs. RHE).

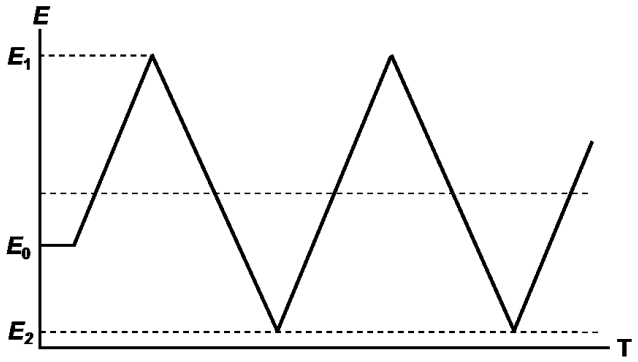

Figure 2.5 Wave pattern of the potential apply on CV measurement.

A typical cyclic voltammogram recorded for a Pt/C electrocatalyst in 0.1 M $HClO_4$ solution at 25 °C is shown in Figure 2.6. When the potential increases from 0.05 V, a

current begins to flow and reaches a peak as the potential increases further. This is related to hydrogen desorption reaction occurring on the electrode surface. Between 0.45 and 0.55 V, only a small current flow is measured. This current is attributed to the formation of electrolytic double layer. As the potential increases from 0.55 V further, the platinum surface becomes oxidized and is covered with an oxide layer. At higher potentials, the current rises significantly because the formation of oxygen starts. By decreasing the potential, the platinum surface is reduced, but not until about 1.0 V due to the over potential. At approximately 0.35 V, platinum starts to get covered with hydrogen and at lower potentials near 0.05 V, molecular hydrogen is formed. Then, with sweeping to the positive potential again, hydrogen starts desorbing from platinum surface.

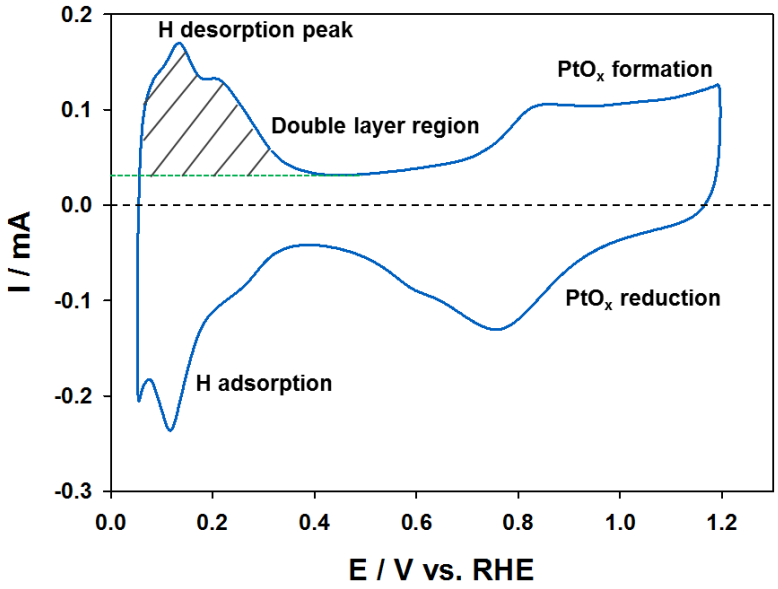

Figure 2.6 A typical cyclic voltammogram of a Pt/C electrocatalyst.

The electrochemical surface area (ECA) can be obtained by quantifying the total charge (Q_H) provided by hydrogen desorption on the catalyst surface. As shown in Figure 2.6, shaded area indicates the electric charge generated by hydrogen desorption during the cyclic voltammetry measurement. The Q_H value can be calculated using the analyzing software (Hokuto Denko Corp., HZ-5000ANA). The charge, which can be generated from the desorption from platinum surface completely covered with hydrogen, is 2.1 C m^{-2} (one hydrogen atom per platinum atom in a single layer) [9]. With these values, the electrochemical surface area (A_s) can be calculated as below.

$$A_S[\mathrm{m^2g^{-1}}] = \frac{Q_H[\mathrm{C}]}{2.1[\mathrm{C}/m^2]\cdot L_{Pt}[\mathrm{g}]} \quad (2.3)$$

where Q_H is the electric charge of hydrogen desorption; L_{Pt} is the mass of platinum.

Before the measurement, for cleaning process of the platinum surface, 50 cycles were applied between 0.05 and 1.20 V vs. RHE under the nitrogen saturated condition. Then, CV measurement was performed every 500 potential cycles during the potential cycle test.

2.4.4 Rotation Disk Electrode Method

The rotating disk electrode (RDE) is a convenient technique to study the mechanism of electrochemical reactions and to determine their kinetic parameters. It is a method analyzing the electrode activity quantitatively by controlling the mass transport speed of species to and from the electrode surface through the change in rotation rates of the electrode. Figure 2.7 shows the schematic view of the reaction occuring on a rotation disk electrode.

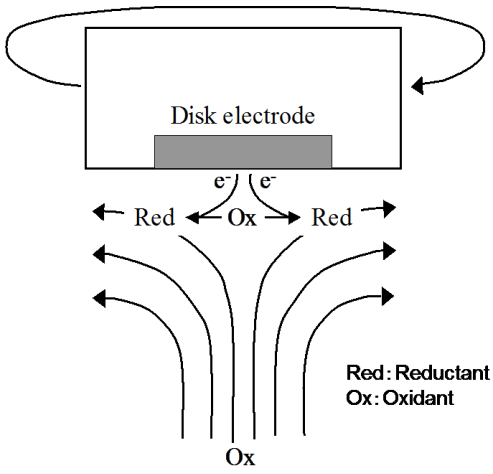

Figure 2.7 A schematic view of the reaction occuring on a rotation disk electrode.

For ORR measurements in this study, the potential was linearly swept from 0.20 V to 1.20 V with the scan rate of 10 mV/s. The voltammogram obtained by rotation disk electrode is also called linear sweep voltammogram (LSV). For all the prepared Pt/C electrocatalysts, LSV curves of them were measured at different rotation speeds (400, 900, 1600, and 2500 rpm). Figure 2.8 shows typical LSV curves of a Pt/C electrocatalyst. Below 1.0 V, oxygen starts reduced, leading to increase in current. Here, oxygen amount

is controlled by diffusion from the electrolyte solution, which is determined by rotation speed of the electrode. Usually, below 0.7 V, the plateau is observed and called as the diffusion limited current. Between 0.7 to 1.0 V, the current is more dominated by the kinetic part of reactions. Therefore, ORR activity of electrocatalysts is evaluated at this potential area. For quantifying ORR activity among Pt/C electrocatalysts, mass activity (A/g_{Pt}) is calculated using the value of current at 0.90 V obtained from LSV curves.

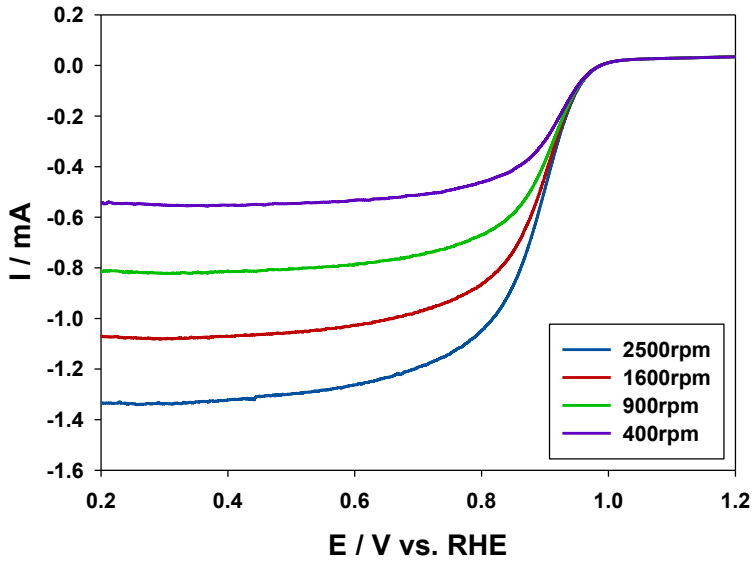

Figure 2.8 LSV curves of a typical Pt/C electrocatalyst at different rotational speeds.

It is well known that the Koutecky-Levich equation [9] listed below is employed to determine the kinetic parameters:

$$1 / i = 1 / i_k + 1 / (0.620nFAcD^{2/3}v^{-1/6}\omega^{1/2}) \quad (2.4)$$

where i is the measured current; i_k is the kinetic current; n is the number of electrons transferred in the half reaction (mol^{-1}); F is the Faraday constant (C/mol); c is the analyte concentration (mol/cm^3); A is the electrode area (cm^2); D is the diffusion coefficient (cm^2/s); v is the kinematic viscosity (cm^2/s); ω is the angular rotation rate of the electrode (rad/s).

The kinetic current i_k does not depend on the rotation speed. A straight line is given with a plot $1/i$ vs. $\omega^{1/2}$ at a constant potential. Then, i_k is obtained when $\omega^{1/2}$ is an infinite.

Using the Koutecky-Levich equation and the data recorded in Figure 2.8, Koutecky-Levich plot can be made as shown in Figure 2.9. Mass activity is calculated

using the kinetic current, read from Koutecky-Levich plot:

$$\text{Mass activity } (A/g_{Pt}) = i_k / g_{Pt} \tag{2.5}$$

where g_{Pt} is the mass of platinum.

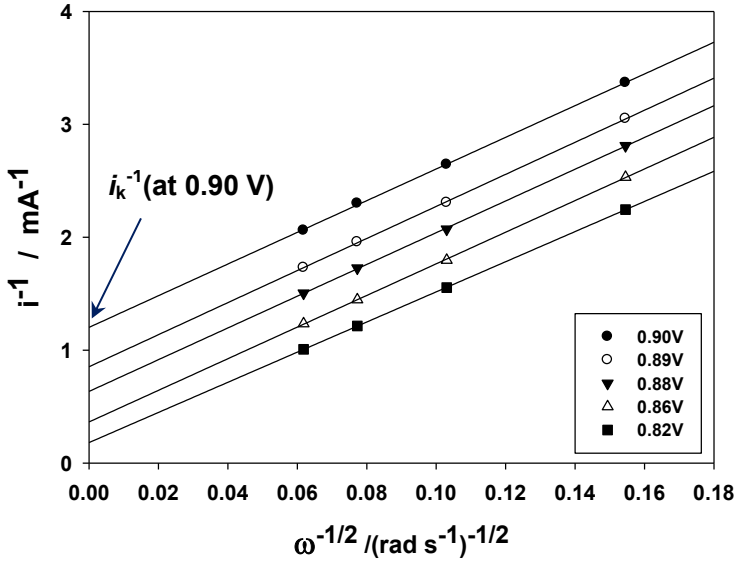

Figure 2.9 Koutecky-Levich plot of a typical Pt/C electrocatalyst.

In this study, ORR measurements were performed four times during the potential cycle test – before potential cycle, after 10000 potential cycles, after 30000 potential cycles and after 60000 potential cycles under the oxygen saturated condition. Then, mass activity at 0.90 V was evaluated.

2.4.5 Durability

In actual FCVs, it is generally said that the gas in the anode flowfield is gradually replaced by air during shut-down period and cathode potential becomes increased around 1.4 V vs. RHE during start-up operation, owing to so-called "hydrogen-front" mechanism [10]. Based on the simulation study of start-stop operation under the condition where both anode and cathode are supplied with air and then hydrogen is introduced into the anode flowfield, the cathode potential exhibits a triangular sweep behavior and reaches approximately 1.5 V vs. RHE at low flow rates [11]. Therefore, electrochemical durability of electrocatalysts was investigated according to the simulated actual start-stop potential cycle protocol, made of triangle waves between 1.0 and 1.5 V vs. RHE with 2

sec per cycle, made by Fuel Cell Commercialization Conference of Japan (FCCJ) [8] as described in Figure 2.10.

In this study, potential cycle test was performed up to 60000 cycles at 25 °C for all Pt/C electrocatalysts.

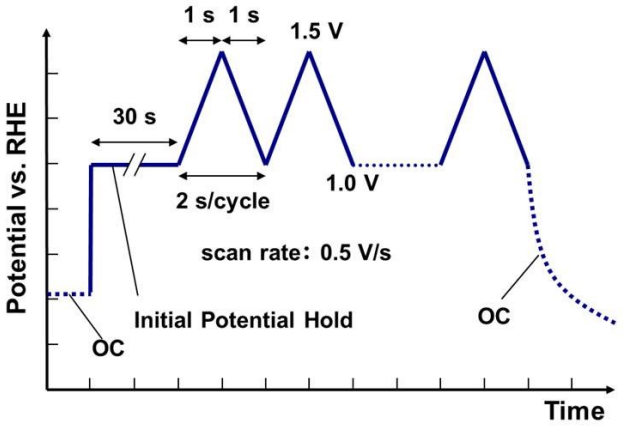

Figure 2.10 Start-stop potential cycle protocol recommended by FCCJ [8].

2.4.6 Platinum Dissolution

To evaluate platinum dissolution phenomena, Inductively Coupled Plasma Atomic Emission Spectroscopy (ICP-AES), also referred to as Inductively Coupled Plasma Optical Emission Spectrometry (ICP-OES), is an useful analytical technique. It is a type of emission spectroscopy that uses the inductively coupled plasma to produce excited atoms and ions which emit electromagnetic radiation at characteristic wavelengths of a particular element [12-13]. The intensity of this emission can indicate the concentration of elements within the sample solution.

In this study, in order to make clear if and how much platinum was dropped or dissolved into the electrolyte solution during the potential cycle test, ICP analysis was performed. The amount of platinum ions, including platinum nanoparticles, in selected electrolyte solution after 60000 cycles was analyzed. For this particular analysis, carbon paper without Teflon coated (Toray, EC-TP1-060) was used as a counter electrode instead of Pt-wire in order to eliminate platinum ion coming from the counter electrode. Then, carbon paper after 60000 cycles was placed in aquilegia (HCl : HNO_3 = 3 : 1) and ultra-sonicated for 10 minutes. This aquilegia was diluted by MillQ water and also analyzed by ICP. Possible re-precipitation of platinum on the carbon paper was counted

for actual amount of dissolution from Pt/C electrocatalysts.

2.5 Evaluation of MEAs

2.5.1 Preparation

Those Pt/C electrocatalysts which had high durability in the half-cell experiment were selected for MEA test. MEA was prepared in the following.

The electrocatalysts prepared in this study were used for the cathode. Commercially available 46.2% platinum deposited Ketjen black (TKK Corp., TEC10E50E) was used as the anode electrocatalyst in all the cases. Typically, the slurry, composed of 100 mg of electrocatalysts (Pt/VC, Pt/VC1600, or TEC10E50E), 0.481 mL of ultrapure water, 4.335 mL of 99.5% ethanol, and 0.981 mL of 5% Nafion® solution, was well dispersed by ultrasonic homogenizer (SMT company, UH-600). Here, the ratio of Nafion®/electrocatalyst was 0.30/0.70 and 0.24/0.76 for the anode and the cathode, respectively.

Then the prepared slurry was spray-printed on the both side of Nafion® NRE-212 (Dupont) within the area of circle (area: 0.5 cm^2) by the spray printing system (Nordson, C-3J) as shown in Figure 2.11. Platinum loading at the anode and the cathode was kept to 0.3 mg cm^{-2}.

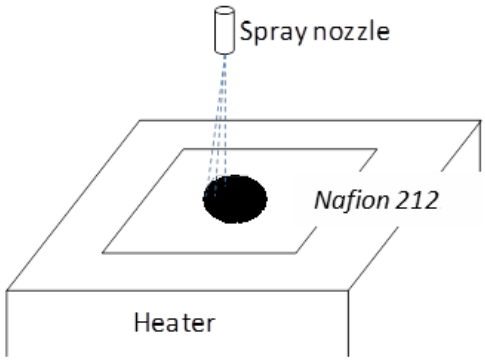

Figure 2.11 Spray-printing of MEA.

Finally, the electrocatalyst-deposited Nafion® membrane was hot-pressed at 0.3 kN for 190 seconds. After that, hydrophobic carbon paper with polytetrafluoroethylene (Toray, EC-TP1-060T) was cut into the circle (area: 0.5 cm^2), and

electrocatalyst-deposited Nafion® membrane was sandwiched by two pieces of carbon paper and then hot-pressed at 0.6 kN and 132 °C for 20 seconds. Figure 2.12 shows a schematic drawing of hot-pressing and a photo of MEA made in this study. Table 2.4 summerizes the conditions of MEA preparation.

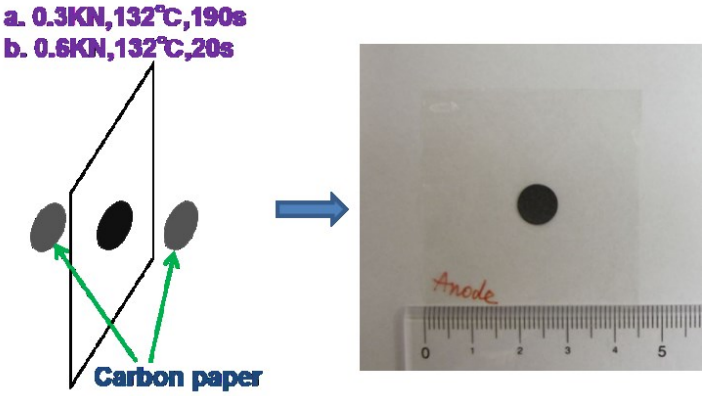

Figure 2.12 A schematic drawing of hot-pressing (left) and a photo of MEA made in this study (right).

Table 2.4 Conditions for MEA preparation.

	Anode	**Cathode**
Electrocatalyst	TEC10E50E (TKK)	Pt/VC and Pt/GVC1600
Ratio of Nafion /electrocatalysts	0.30/0.70	0.24/0.76
Platinum loading (mg/cm^2)	0.3	0.3
Membrane	Nafion® NRE-212 (Dupont)	
Gas diffusion layer	Hydrophobic carbon paper (Toray, EC-TP1-060T)	

2.5.2 I-V Characteristic

For measurement of current-voltage (I-V) characteristics, a prepared MEA was sandwiched with the cell holder as shown in Figure 2.13. A I-V characteristic was measured at the cell temperature of 80 °C under the flow of 100% humidified H_2 and air into the anode and the cathode, respectively, with a constant flow rate of 100 cc min^{-1} (Table 2.5).

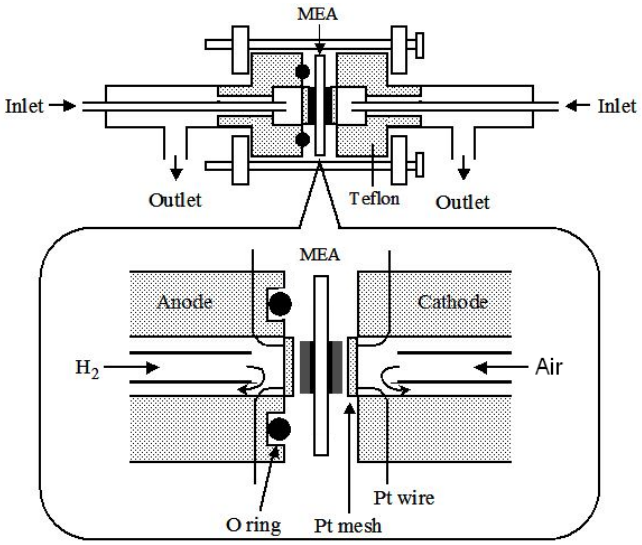

Figure 2.13 A schematic diagram of setting up of MEA on the holder.

Table 2.5 Conditions for MEA measurement.

	Anode	**Cathode**
Gas	H_2	Air
Humidity	100% RH	
Flow rate	100 cc min^{-1}	
Cell operation temperature	80 °C	

N_2 is used to purge the anode and cathode chambers of the cell prior to introducing reactants and shutting down the measurement, in order to remove with any residual gas.

As a pretreatment step before the actual measurement, a constant current of 200 mA cm^{-2} was applied to the MEA by Current Pulse Generator (Hokuto Denko, HC-III) for four hours in order to sufficiently humidify the MEA to maintain conductivity of the electrolyte membrane. Finally, the values of cell voltage were recorded during applying the current from zero until the voltage decreased to about 0.20 V with an interval of one minute.

2.5.3 Ohmic Resistance

The current interrupt is a common technique to measure the ohmic drop based on the simple application of Ohm's law. If the flow of this current is stopped suddenly or interrupted then ohmic voltage drops very quickly and linearly as shown in Figure 2.14.

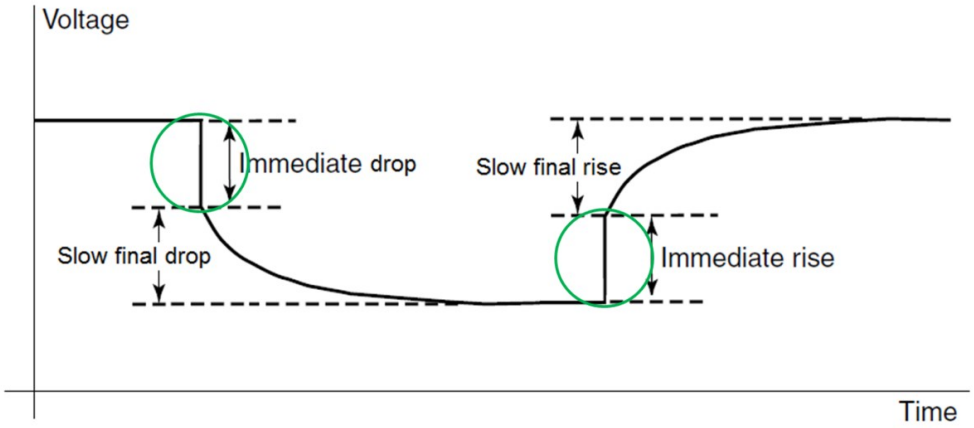

Figure 2.14 Typical voltage changes just before and after the current is interrupted. Linear change (circled) can be used as ohmic drop.

Therefore, ohmic drop is determined by the difference in the voltage immediately before and immediately after the current has been interrupted. The ohmic drop divided by the known current before the interrupting gives the ohmic resistance.

In this study, the current interrupt technique was used to separate the ohmic resistance using a digital phosphor oscilloscope (Tektronix Inc., TDS 3012B). In this measurement, the small reference electrode (Platinum loading is 0.6 mg cm^{-1}) was attached to the anode side of the MEA as shown in Figure 2.15. Under the three different current values for the MEA cell, ohmic drop was recorded and then plotted against the current. Finally, ohmic resistance was calculated through the slope after the linear fitting. Similarly, ohmic resistance of the anode was measured through the circuit between the anode and the reference electrode. Then, cathode resistance was calculated by subtracting the anode ohmic drop from the cell ohmic drop.

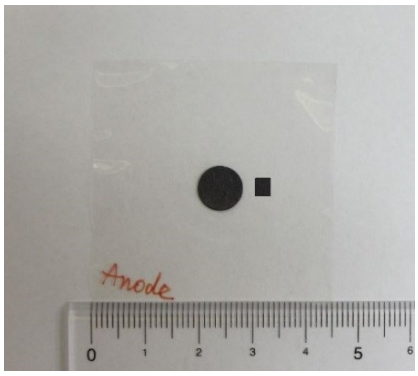

Figure 2.15 A photo of a MEA with the reference electrode.

2.5.4 Durability

Similar to the half-cell measurement as shown in section 2.4.5, the durability analysis of MEAs was also performed using the potential cycles between 1.0 and 1.5 V vs. RHE with 2 sec per cycle. During the potential cycles, H_2 and N_2 were supplied to the anode and the cathode, respectively. Here, the anode was used as reference electrode to applied the potential to the cathode using a fuel cell test system (Toyo Technic, 890e) and a electrochemical interface (Solarton SI, 1287).

2.6 Analyses by Electron Microscopy

Since the Pt/C electrocatalyst is made with small platinum nanoparticles deposited on the surface of carbon, effect of platinum crystallite/particle size on the activity of electrocatalyst has been an important subject [14-18]. Then, evaluation of electrocatalysts using an electron microscopy technique becomes essential.

2.6.1 Ex-situ Observation

In order to declare the relationship between the platinum particle growth and the degradation mechanism of electrocatalyst, the nanostructure changes before and after the cycle test were characterized using transmission electron microscopy (JOEL, JEM-ARM200F or Philips, Tecnai-20) and scanning transmission electron microscope (Hitachi, HD-2300A) at an acceleration voltage of 200 kV, or using field emission scanning electron microscope (FESEM) (Hitachi, S5200) at an acceleration voltage of 30 kV. For the determination of average platinum particle size, 30 to 90 platinum particles on each TEM image were picked up and used for calculation using an image analysis software.

2.6.2 In-situ Observation

In order to gain fundamental understanding of degradation mechanism of Pt/C electrocatalysts, accelerated degradation test was performed using Enviromental TEM (ETEM). In this study, ETEM technique based on a standard 300 kV cold-field emission gun TEM (Hitachi HF3300) equipped with the unique secondary electron and STEM imaging capability was used under the collaboration with Hitachi High-Technology.

An efficient differencial pumping system with a gas injection heating holder allowed in-situ study under heating and in a gaseous atmosphere up to 10 Pa. In this study 200 °C and air atmosphere were in use. A simultaneous in-situ SEM/STEM study for Pt/C electrocatalysts was carried out under such accelerated degradation condition.

References

[1] A.L. Dicks, The role of carbon in fuel cells, J. Power Sources, 156 (2006) 128.

[2] D.A. Stevens, M.T. Hicks, G.M. Haugen, J.R. Dahn, Ex situ and in situ stability of PEMFC catalysts effect of carbon type and humidification on degradation of the carbon, J. Electrochem. Soc., 152 (2005) A2309.

[3] S. Brunauer, P.H. Emmett, E. Teller, Adsorption of gases in multimolecular layers, J. Am. Chem. Soc., 60 (1938) 309.

[4] JIS R 7651. Measurement of lattice parameters and crystallite sizes of carbon materials, 2007.

[5] A. Hayashi, H. Notsu, K. Kimijima, J. Miyamoto, I. Yagi, Preparation of Pt/mesoporous carbon (MC) electrode catalyst and its reactivity toward oxygen reduction, Electrochim. Acta, 53 (2008) 6117.

[6] H. P. Klug, L. E. Alexander, X-ray diffraction procedures, 2nd Ed., John Wiley & Sons Inc., 1974, 687.

[7] H. A. Gasteiger, S. S. Kocha, B. Sompalli and F. T. Wagner, Activity benchmarks and requirements for Pt, Pt-alloy, and non-Pt oxygen reduction catalysts for PEMFCs, Appl. Cat. B: Enviro., 56 (2005) 9.

[8] Fuel Cell Commercialization Conference of Japan (FCCJ), Proposals of the development targets, research and development challenges and evaluation methods concerning PEFCs, http://www.fccj.jp/pdf/23_01_kt.pdf.

[9] A.J. Bard, L.R. Faulkner, Electrochemical Methods, 2nd ed., Wiley, New York, 2001.

[10] C.A. Reiser, L. Bregoli, T.W. Patterson, J.S. Yi, J.D. Yang, M.L. Perry, T.D. Jarvi, A reverse-current decay mechanism for fuel cells, Electrochem. Solid-State Lett., 8 (2005) A273.

[11] A. Ohma, K. Shinohara, A. Liyama, T. Yoshida, A. Daimaru, Membrane and catalyst performance targets for automotive fuel cells by FCCJ membrane, catalyst, MEA WG, ECS Trans., 41 (2011) 775.

[12] A. Stefánsson, I. Gunnarsson, N. Giroud, New methods for the direct determination of dissolved inorganic, organic and total carbon in natural waters by Reagent-Free Ion Chromatography and inductively coupled plasma atomic emission spectrometry, Anal. Chim. Acta, 582 (1) (2007) 69.

[13] J. M. Mermet, Is it still possible, necessary and beneficial to perform research in ICP-atomic emission spectrometry, J. Anal. At. Spectrom., 20 (2005) 11.

[14] L. J. Bregoli, The influence of platinum crystallite size on the electrochemical reduction of oxygen in phosphoric acid, Electrochimica Acta, 23 (1978) 489.

[15] P. N. Ross in U. V. Rao (Ed.), Precious Metals 1986, International Precious Metals Institute, Allentown, PA, 1986, 355.

[16] M. L. Sattler, P. N. Ross, The surface structure of Pt crystallites supported on carbon black, Ultramicroscopy, 20 (1986) 21.

[17] P. Stonehart, J. Baris, J. Hochmuth, P. Pagliaro, DOE/NASA-10176-10, Final Report, 1983.

[18] M. Watanabe, H. Sei, P. Stonehart, The influence of platinum crystallite size on the electroreduction of oxygen, J. Electroanal. Chem., 261 (1989) 375.

Chapter 3

Material Characterization of Electrocatalysts

3.1 Carbon/Graphitized Carbon

As mentioned in chapter 2, eight kinds of carbon materials (VC, GVC1100, GVC1600, GVC2000, KB, GKB1100, GKB1600 and GKB2000) were prepared in this study as carbon supports. In order to understand the difference in material properties, specific surface area and graphitization degree were evaluated through nitrogen adsorption/desorption and X-ray diffraction measurements, respectively.

3.1.1 Specific Surface Area

Based on nitrogen adsorption/desorption measurements, BET surface areas were calculated and listed in Table 3.1.

Table 3.1 Specific surface areas of prepared carbon materials.

Carbon support	BET surface area (m^2g^{-1})	Carbon support	BET surface area (m^2g^{-1})
VC	225	KB	1280
GVC1100	225	GKB1100	1160
GVC1600	110	GKB1600	610
GVC2000	90	GKB2000	300

BET surface area for the Vulcan group materials had a tendency to decrease after the heat treatment, and decreased more at relatively higher heat treatment temperatures. This is associated with the increase in more crystallized surface by the removal of amorphous surface including structural defects since it is oxidized to such as CO_2 in the presence of small amount of oxygen.

This chapter has been published in Zhao et al., *J. Electrochimica Acta* 97 (2013) 33-41.

For the Ketjen Black group materials, the similar tendency was seen. Since the initial BET surface area of KB was almost six times larger than VC, even after the heat treatment at 2000 °C, BET surface area was kept to 300 m^2g^{-1}. However, the rate of BET surface loss was relatively large for Ketjen Black group materials.

3.1.2 Graphitization Degree

In this study, graphitization degree is defined as how close the d_{002} value is to 0.3354 nm, which is that of graphite. For further quantitatively analyzing the graphitization degree, the interlayer spacing and respective crystallite size of each material were determined based on JIS R 7651:2007 as explained in section 2.2.4. They were analyzed by X-ray diffraction, particularly (002) diffraction, by referring to the diffraction positions of the standard silicon. Resulting XRD spectra of C (002) diffraction, and interlayer spacing d_{002} and respective crystallite size L_c(002) are listed in Figure 3.1 and Table 3.2, respectively.

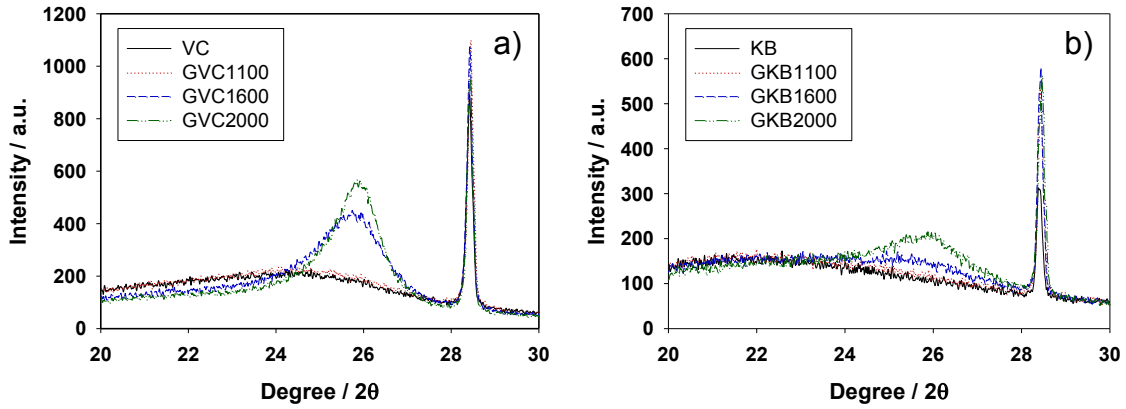

Figure 3.1 XRD spectra showing carbon (002) diffraction using silicon as a standard for a) VC, GVC1100, GVC1600 and GVC2000 and b) KB, GKB1100, GKB1600 and GKB2000.

Table 3.2 Interlayer spacing d_{002} and crystallite size L_c(002) for prepared carbon materials.

Carbon support	d_{002} (nm)	L_c (002) (nm)	Carbon support	d_{002} (nm)	L_c (002) (nm)
VC	0.3524	3.0	KB	--	--
GVC1100	0.3522	3.3	GKB1100	--	--
GVC1600	0.3448	5.5	GKB1600	0.3450	4.1
GVC2000	0.3436	7.7	GKB2000	0.3440	5.0

In this study, (002) diffraction line was very broad for VC and GVC1100, however, the interlayer spacing d_{002} and the crystallite size L_c(002) of them were roughly calculated. On the other hand, neither the interlayer spacing d_{002} nor the crystallite size L_c(002) was determined since both KB and GKB1100 did not have clear (002) diffraction lines owing to their low graphitic surface as shown in Figure 3.1.

For both the Vulcan and Ketjen Black group materials, the interlayer spacing d_{002} gradually decreased and got close to 0.3354 nm, derived from the ideal graphite crystal [1], with increasing heat treatment temperature. The respective crystallite size also gradually grew, consisting with the previous reports [2-3]. Therefore, more graphitized surfaces of carbon were successfully obtained with increasing heat treatment temperature [4]. Consequently, in our study, GVC2000 and GKB2000 exhibited the highest graphitization degree among the Vulcan and Ketjen Black group materials, respectively. Similar to BET surface area, the heat treatment at 1100 °C did not change much on graphitization degree. It is probably because the temperature of 1100 °C is not high enough for graphitization of the carbon surface.

3.2 Platinum Deposited Carbon/Graphitized Carbon

3.2.1 Platinum Loading

For eight different carbon materials, platinum catalysts were deposited using platinum (II) acetylacetonate as a platinum precursor with the method mentioned in section 2.3.1. The actual amount of deposited platinum on carbon was analyzed by TG measurement, and every Pt/C electrocatalyst was confirmed to contain about 20 wt% of platinum as listed in Table 3.3.

Table 3.3 Platinum loading determined from TG measurements for prepared Pt/C electrocatalysts.

Pt/C electrocatalyst	Platinum loading (wt%)	Pt/C electrocatalyst	Platinum loading (wt%)
Pt/VC	20.2	Pt/KB	20.7
Pt/GVC1100	19.8	Pt/GKB1100	21.3
Pt/GVC1600	19.6	Pt/GKB1600	19.7
Pt/GVC2000	17.4	Pt/GKB2000	18.1

Since GVC1600, GVC2000, GKB1600, and GKB2000 have lower BET surface

area, almost half or lower than the original BET surface area of original Vulcan or Ketjen Black, more platinum (II) acetylacetonate against carbon was used in order to keep depositing almost the same 20 wt% platinum on these carbon supports. It was probably because the more graphitized surface formed by the heat treatment at 1600 °C and 2000 °C was not able to absorb platinum (II) acetylacetonate before the reduction of Pt (II) to Pt(0).

3.2.2 TEM Observation

TEM observation was made in order to check the particle size and the distribution of platinum on carbon supports.

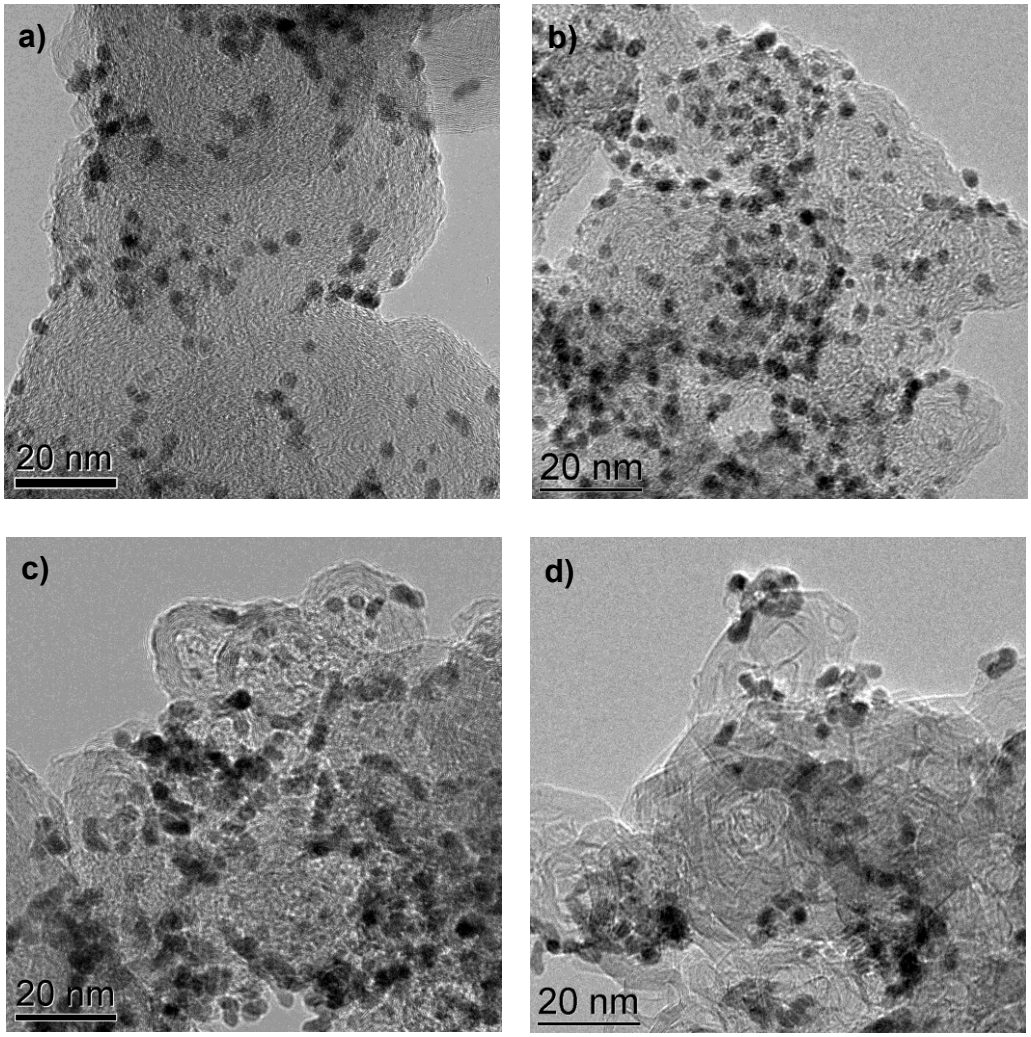

Figure 3.2 TEM images of a) Pt/VC, b) Pt/GVC1100, c) Pt/GVC1600, and d) Pt/GVC2000.

Figure 3.2 shows TEM images of Pt/VC, Pt/GVC1100, Pt/GVC1600, and Pt/GVC2000. Platinum particles were homogeneously distributed for Pt/VC and Pt/GVC1100 electrocatalysts. For Pt/GVC1600 and Pt/GVC2000 electrocatalysts, graphite-like layers on the surface of carbon support were clearly observed. Although agglomeration of some platinum particles was seen for Pt/GVC1600, platinum particles were adequately dispersed on the carbon surface. For Pt/GVC2000, platinum particles were not homogeneously deposited and rather agglomerated on certain spots, which was resulted from its highest graphitization degree.

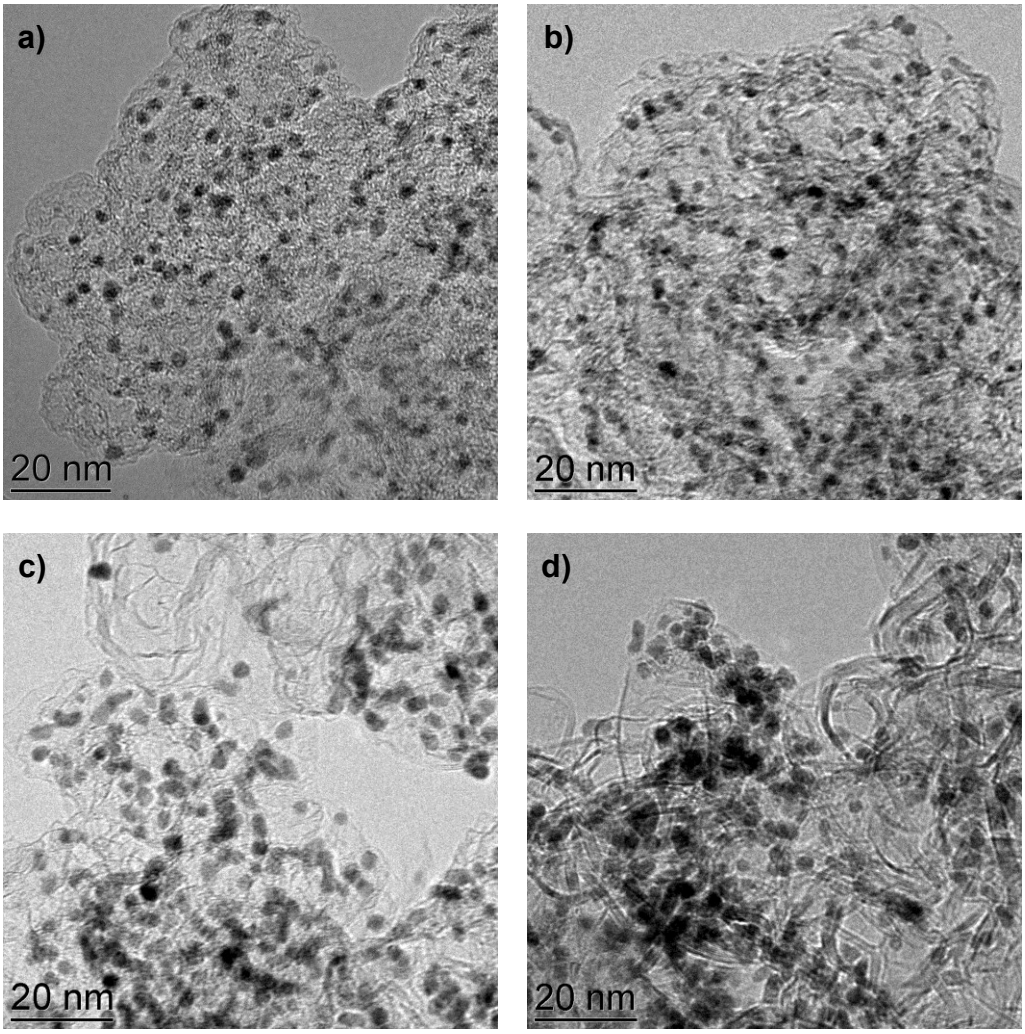

Figure 3.3 TEM images of a) Pt/KB, b) Pt/GKB1100, c) Pt/GKB1600, and d) Pt/GKB2000.

Figure 3.3 shows TEM images of Pt/KB, Pt/GKB1100, Pt/GKB1600, and Pt/GKB2000. Similar to Pt/Vulcan group electrocatalysts, graphite-like layers on the surface of carbon support were also observed for Pt/GKB1600 and Pt/GKB2000. Except

for Pt/GKB2000, where agglomeration of platinum particles was seen for some locations, platinum particles were well dispersed on carbon supports for the other three Pt/Ketjen Black group electrocatalysts.

3.2.3 Average Platinum Crystallite and Platinum Particle Size

X-ray diffraction measurement was performed, and average platinum crystallite size on carbon support was calculated from the Scherrer's equation using platinum (111) peak and listed in Table 3.4. As expected, the size of platinum crystallite became larger when they were deposited on more graphitized carbon as a result of lower surface area of the carbon support followed by lower dispersion of platinum particles. Even so, the crystallite size stayed within the range of 2.0 and 3.0 nm.

Table 3.4 Average platinum crystallite and platinum particle size analyzed by X-ray diffraction and TEM.

Pt/C electrocatalyst	d_{XRD} (nm)	d_{TEM} (nm)	Pt/C electrocatalyst	d_{XRD} (nm)	d_{TEM} (nm)
Pt/VC	2.25	2.32 ± 0.38	Pt/KB	2.07	2.11 ± 0.36
Pt/GVC1100	2.41	2.44 ± 0.30	Pt/GKB1100	2.20	2.14 ± 0.35
Pt/GVC1600	2.88	2.85 ± 0.46	Pt/GKB1600	2.52	2.53 ± 0.33
Pt/GVC2000	2.94	2.88± 0.42	Pt/GKB2000	2.65	2.62 ± 0.39

From the TEM images shown in Figure 3.1 and 3.2, the size of platinum particles was also evaluated using image analysis software named Scandium with the number of selected platinum particles from 30 to 90 for eight Pt/C electrocatalysts. Results are listed in Table 3.4. The size of platinum particles derived from X-ray diffraction and TEM were well matched each other. Details of TEM analyses will be discussed in the later section with the results after the electrochemical durability test.

3.3 Conclusions

Eight kinds of carbon materials were obtained through heat treatment of commercially available Vulcan and Ketjen Black at three different heat treatment temperatures. Results from BET and X-ray diffraction measurements showed that carbon materials with higher graphitization degree were obtained by heat treatment at higher

temperatures. Platinum particles were successfully deposited on these carbon materials with the loading of about 20 wt%. X-ray diffraction and TEM analyses revealed that the platinum particle size of all the Pt/C electrocatalysts stayed between 2.0 and 3.0 nm in diameter, even though the agglomeration of platinum particles was distinguished on the carbon treated at higher temperatures.

References

[1] H. O. Pierson, Handbook of carbon, graphite, diamond and fullerenes, Noyes Publications, 1993, 156.

[2] F.G. Emmerich, Application of a cross-linking model to the Young`s modulus of graphitizable and non-graphitizable carbons, Carbon, 33 (1995) 47.

[3] J. Rodriguez-Mirasol, T. Cordero, J. J. Rodriguez, High-temperature carbons from kraft lignin, Carbon, 34 (1996) 43.

[4] A.B. Garcia, I. Camean, I. Suelves, J.L. Pinilla, M.J. Lazaro, J.M. Palacios, R. Moliner, The graphitization of carbon nanofibers produced by the catalytic decomposition of natural gas, Carbon, 47 (2009) 2563.

Chapter 4

Electrochemical Characterization of Pt/C Electrocatalysts

4.1 Electrochemical Evaluation of Pt/Vulcan Group Electrocatalysts at 25 °C

Prepared four different Pt/Vulcan group electrocatalysts were evaluated in 0.1 M $HClO_4$ solution at 25 °C using a three-electrode set-up. Electrochemically active surface area (ECA) and oxygen reduction reactivity (ORR) were evaluated using cyclic and linear sweep voltammetry. ECA and ORR were recorded before and after the certain potentials, which was based on the durability protocol.

4.1.1 Change in Cyclic Voltammograms During the Potential Cycle Test

Cyclic voltammograms for Pt/VC, Pt/GVC1100, Pt/GVC1600, and Pt/GVC2000 are shown in Figure 4.1, 4.2, 4.3, and 4.4, respectively. Change in cyclic voltammograms during the potential cycles (10000, 30000, 60000 cycles) between 1.0 and 1.5 V is also included in these figures.

This chapter has been published in Zhao et al., *J. Electrochimica Acta* 97 (2013) 33-41.

As shown in cyclic voltammograms stated as 0 cycle (black line) in Figure 4.1 to Figure 4.4, the size of electronic double layer at 0.3-0.5 V decreased for the carbon support materials with heat treatment at a higher temperature, corresponding to the lowering of BET surface area of carbon. All these four electrocatalysts showed clear hydrogen adsorption/desorption and PtO_x formation/reduction peaks. By comparing with Figures 4.1, 4.2, 4.3, and 4.4, it is clear that all these Pt/C electrocatalysts had a tendency to lose its hydrogen adsorption/desorption and PtO_x formation/reduction peaks after the potential cycle test, but the rate of loss was different. Apparently, Pt/GVC1600 (Figure 4.3) showed the least decrease in those peaks during the potential cycle test among Pt/Vulcan group electrocatalysts.

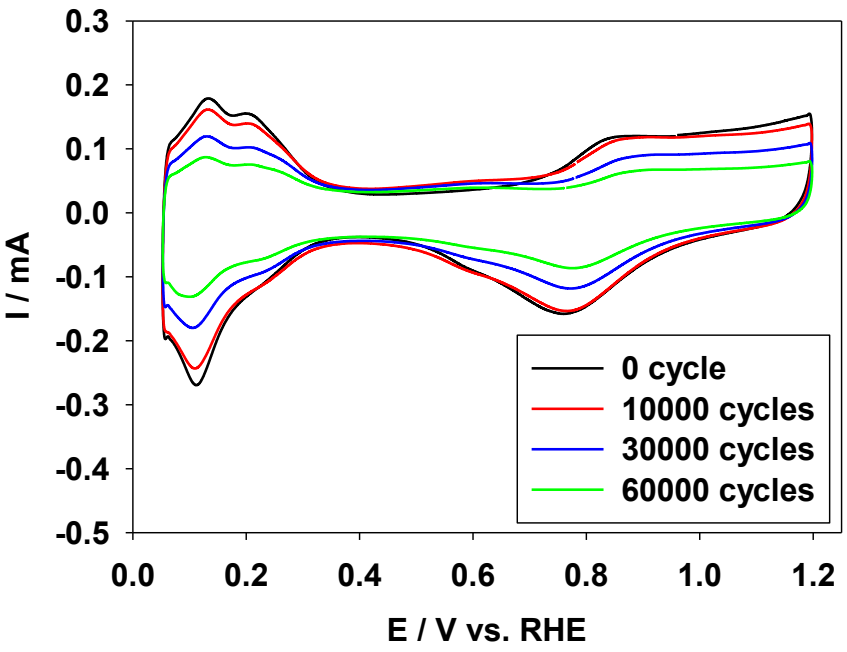

Figure 4.1 Cyclic voltammograms of Pt/VC after 0, 10000, 30000, 60000 cycles of the potential cycle test. Measurements were recorded in N_2 saturated 0.1 M $HClO_4$ solution at 25 °C with the scan rate of 50 mV/s.

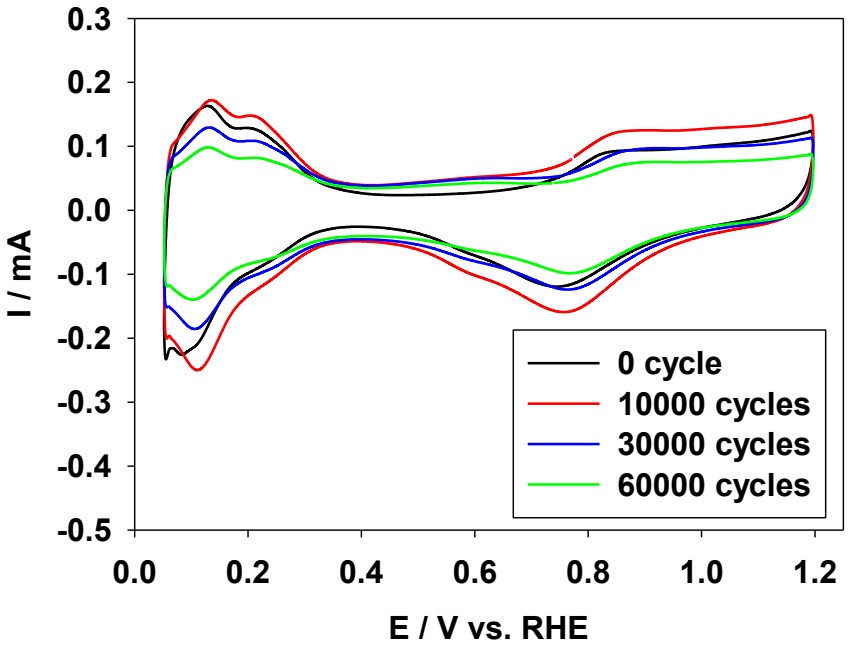

Figure 4.2 Cyclic voltammograms of Pt/GVC1100 after 0, 10000, 30000, 60000 cycles of the potential cycle test. Measurements were recorded in N_2 saturated 0.1 M $HClO_4$ solution at 25 °C with the scan rate of 50 mV/s.

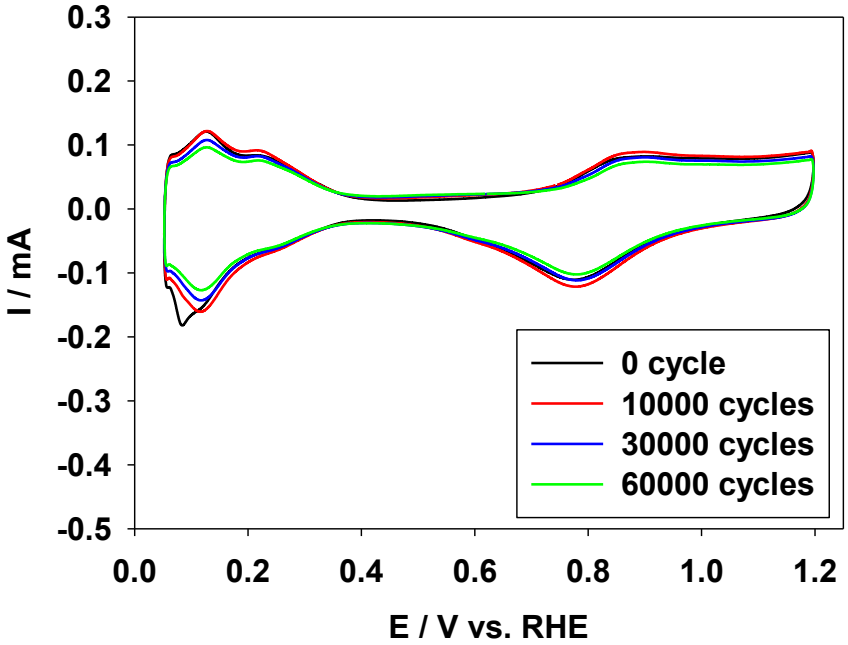

Figure 4.3 Cyclic voltammograms of Pt/GVC1600 after 0, 10000, 30000, 60000 cycles of the potential cycle test. Measurements were recorded in N_2 saturated 0.1 M $HClO_4$ solution at 25 °C with the scan rate of 50 mV/s.

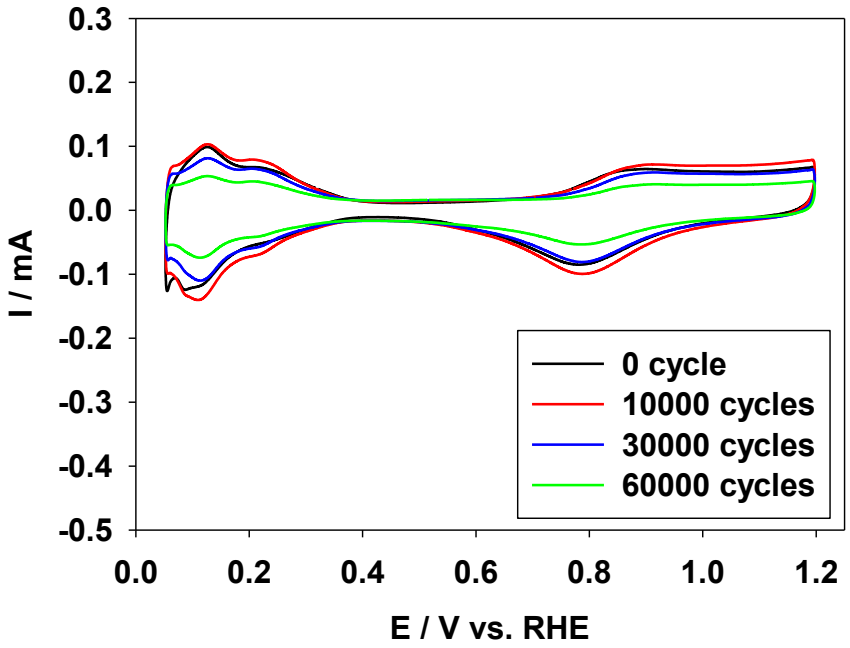

Figure 4.4 Cyclic voltammograms of Pt/GVC2000 after 0, 10000, 30000, 60000 cycles of the potential cycle test. Measurements were recorded in N_2 saturated 0.1 M $HClO_4$ solution at 25 °C with the scan rate of 50 mV/s.

4.1.2 Change in ECA During the Potential Cycle Test

ECAs of these four Pt/C electrocatalysts were calculated based on Figure 4.1 to Figure 4.4 using the charge associated with hydrogen desorption on platinum (2.1 C m^{-2}). Change in ECA against the number of potential cycle was plotted in Figure 4.5.

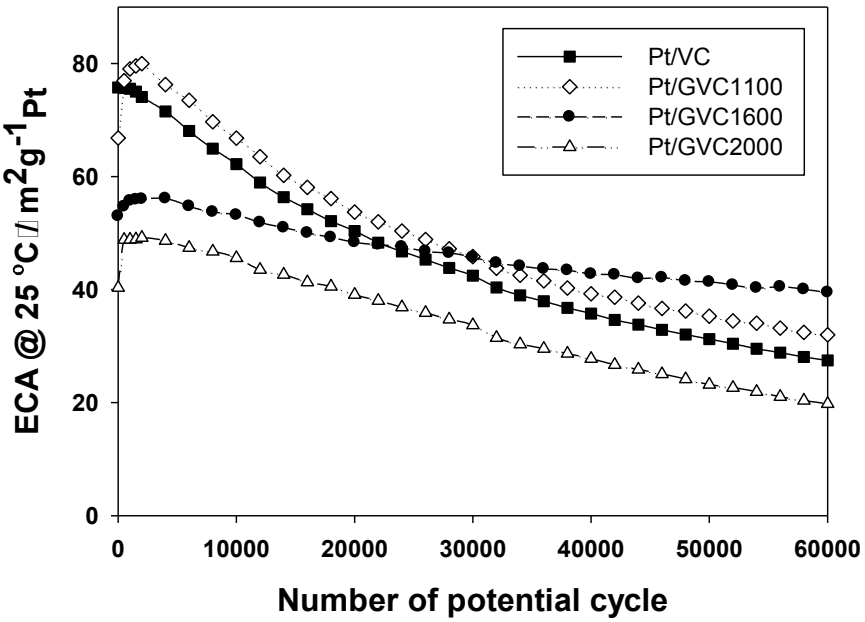

Figure 4.5 Change in ECA during the potential cycle test for Pt/VC, Pt/GVC1100, Pt/GVC1600, and Pt/GVC2000.

Besides Pt/VC, ECA increased after the initial several hundred cycles probably owing to the produced clean platinum surface during the potential cycles. Therefore, for quantitative comparison, initial ECA, maximum ECA, ECA after 60000 potential cycles, and % retention of ECA ($ECA_{after\text{-}60k\text{-}cycles}$ / ECA_{max}) were calculated for each Pt/Vulcan group electrocatalyst and listed in Table 4.1. The % retention of ECA was confirmed by testing two to three samples for each Pt/C electrocatalyst and the differences among test remained within a few percent.

Table 4.1 ECAs of Pt/Vulcan group electrocatalysts.

Pt/C electrocatalyst	Initial ECA (m^2g^{-1})	Max. ECA (m^2g^{-1})	ECA after 60000 cycles (m^2g^{-1})	Retention of ECA (%)
Pt/VC	75.8	75.8	27.5	36.3
Pt/GVC1100	66.8	80.0	32.0	40.0
Pt/GVC1600	53.0	56.1	39.5	70.4
Pt/GVC2000	40.3	49.2	19.8	40.2

By looking at ECA_{max} values in Table 4.1, ECA_{max} decreased for Pt/GVC1600 and Pt/GVC2000 although all the samples had similar platinum particle size as shown in Table 3.4. This is probably due to the increased aggregation of platinum particles on the

smoothened carbon surface of GVC1600 and GVC2000 resulted from the heat treatment, leading to the loss of sufficient interparticle distance for electrocatalytic reactions [1].

Regarding to their durability, Pt/GVC1600 showed highest durability and retention of ECA, 70.4%, which was almost twice better than that of Pt/VC. On the other hand, Pt/GVC2000 showed retention of ECA, 40.2%, which was almost the same as that of Pt/VC, even though GVC2000 had highest graphitization degree as mentioned in chapter 3. This is probably because the interaction between the platinum nanoparticles and the carbon support became weakened at the same time. Platinum agglomeration and detachment were easily happened in such cases, leading to the decrease in ECA values and also % retention of ECA. Pt/GVC1100 showed retention of ECA, 40.0%, which was almost the same as that of Pt/VC. This result can be easily explained from the results of material properties after the heat treatment at 1100 °C in chapter 3, which were not much changed from the original Pt/VC.

In case of Pt/VC and Pt/GVC1100, they sometimes detached from the electrode surface owing to their degradation during the potential cycle test. In such cases the % retention of ECA became much lower like 10-20 % as shown in Figures 4.6 and 4.7.

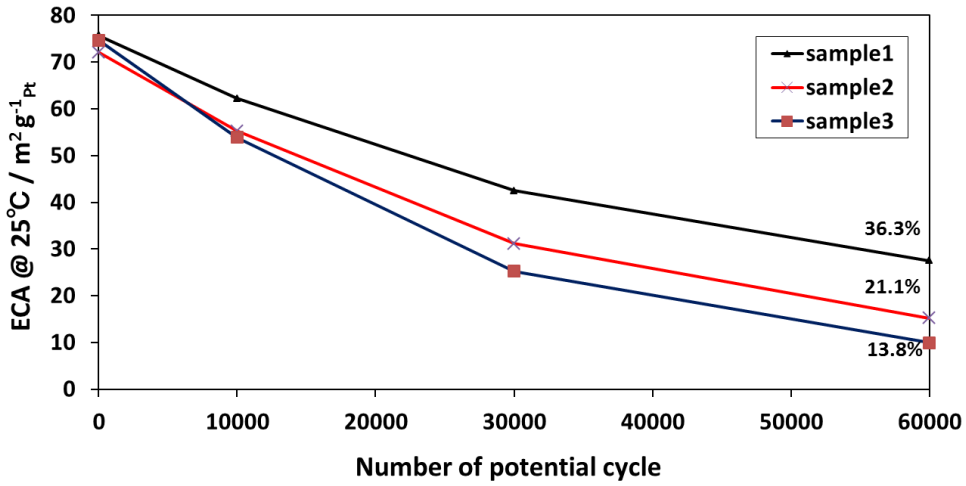

Figure 4.6 Change in ECA during the potential cycle test for Pt/VC including the case that detachment of Pt/VC from the electrode has occured.

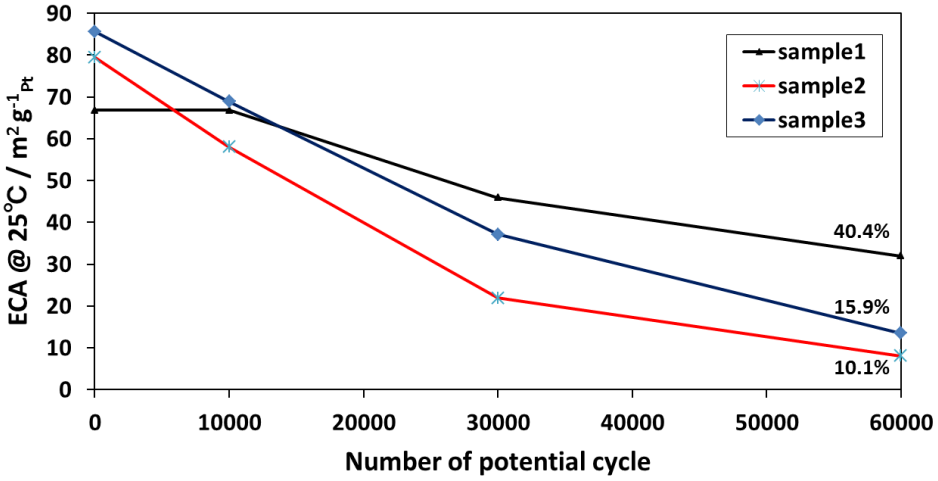

Figure 4.7 Change in ECA during the potential cycle test for Pt/GVC1100 including the case that detachment of Pt/GVC1100 from the electrode has occured.

4.1.3 Change in Linear Sweep Voltammograms for ORR During the Potential Cycle Test

ORR measurements were also performed before and after 10000, 30000, and 60000 potential cycles. Figures 4.8, 4.9, 4.10 and 4.11 show the linear sweep voltammograms under the rotation of 1600 rpm at 25 °C for Pt/VC, Pt/GVC1100, Pt/GVC1600, and Pt/GVC2000 electrocatalyst, respectively.

Similar to the decline of their hydrogen adsorption/desorption and PtO_x formation/reduction peaks in cyclic voltammogram curves, in case of any samples, ORR was also lost at a certain degree during the potential cycle test. However, the rate of loss was different. By comparing with Figures 4.8, 4.9, 4.10 and 4.11, Pt/GVC1600 (Fig. 4.10) clearly showed the smallest decrease in ORR during the potential cycle test among other Pt/Vulcan group electrocatalysts.

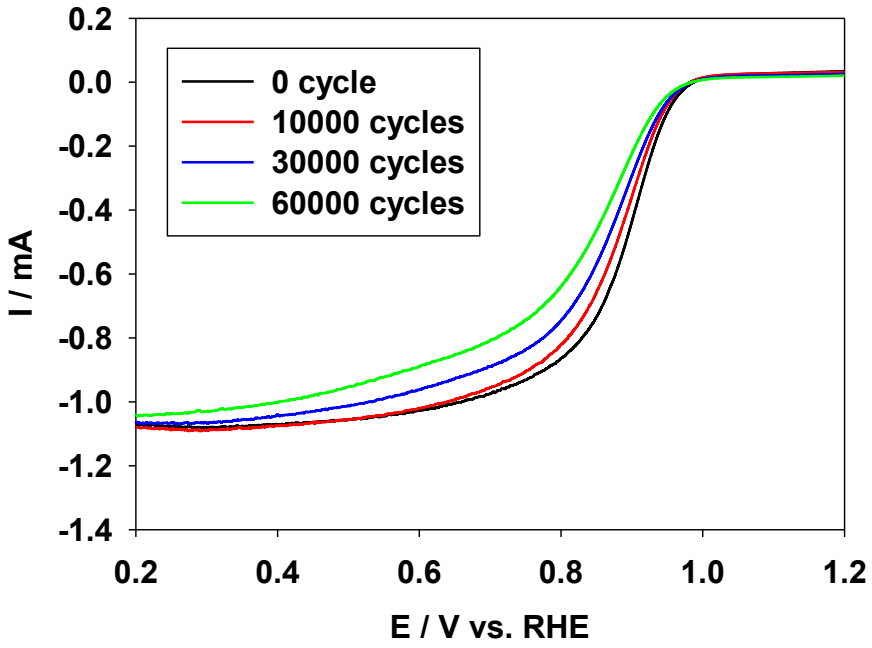

Figure 4.8 Linear sweep voltammograms of Pt/VC after 0, 10000, 30000, 60000 cycles of the potential cycle test. Measurements were recorded in O_2 saturated 0.1 M $HClO_4$ solution at 25 °C with the scan rate of 10 mV/s and the rotation of 1600 rpm.

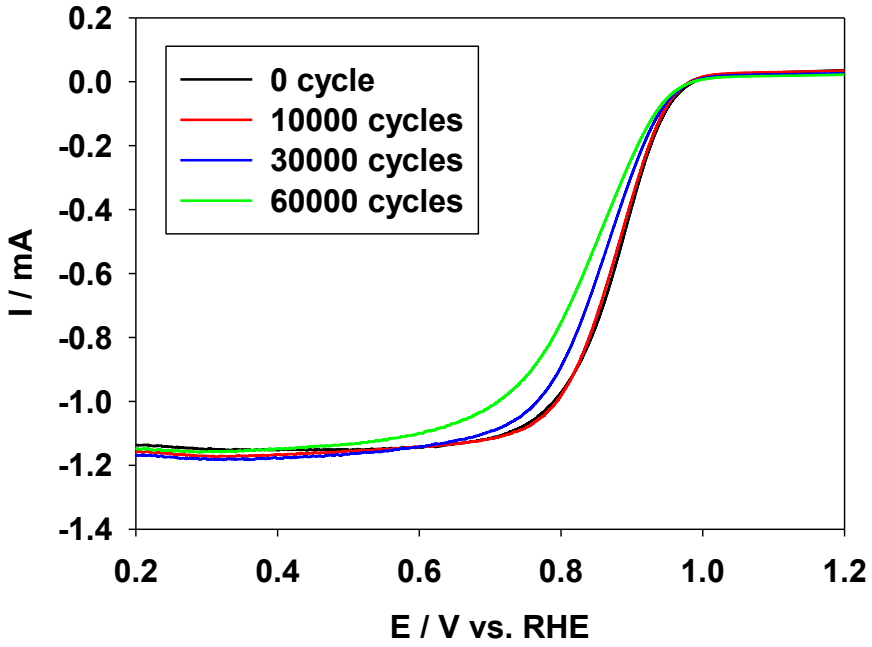

Figure 4.9 Linear sweep voltammograms of Pt/GVC1100 after 0, 10000, 30000, 60000 cycles of the potential cycle test. Measurements were recorded in O_2 saturated 0.1 M $HClO_4$ solution at 25 °C with the scan rate of 10 mV/s and the rotation of 1600 rpm.

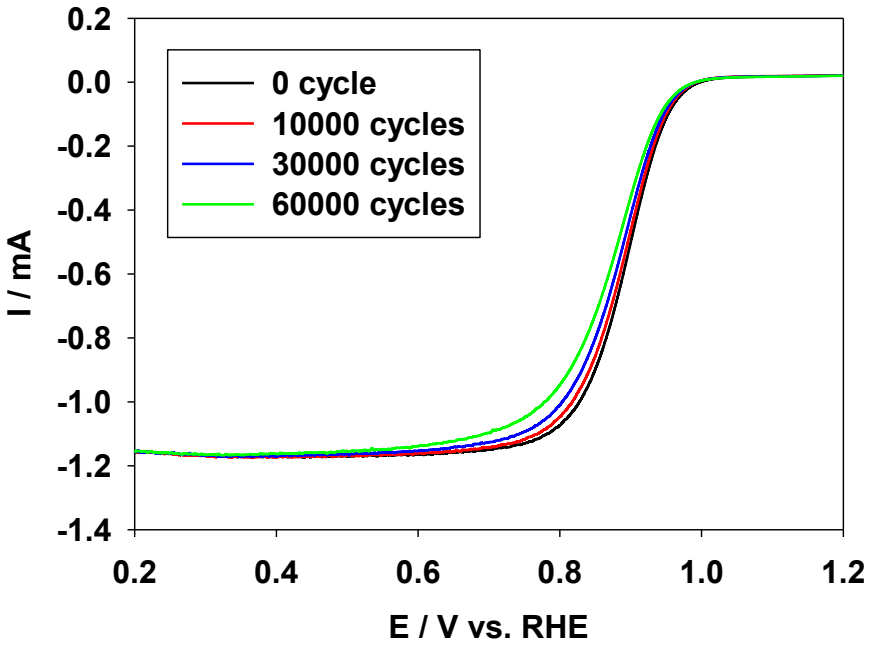

Figure 4.10 Linear sweep voltammograms of Pt/GVC1600 after 0, 10000, 30000, 60000 cycles of the potential cycle test. Measurements were recorded in O_2 saturated 0.1 M $HClO_4$ solution at 25 °C with the scan rate of 10 mV/s and the rotation of 1600 rpm.

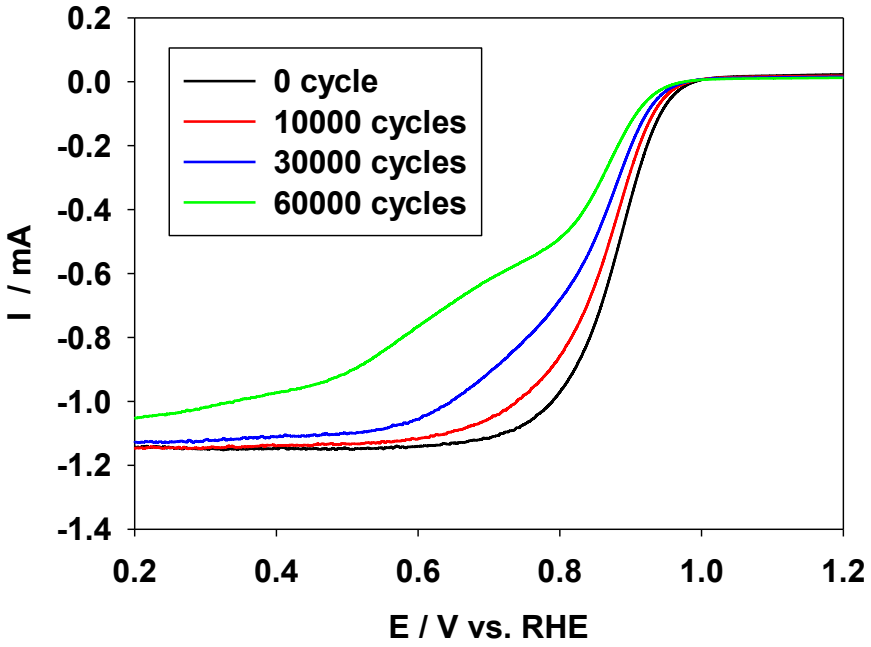

Figure 4.11 Linear sweep voltammograms of Pt/GVC2000 after 0, 10000, 30000, 60000 cycles of the potential cycle test. Measurements were recorded in O_2 saturated 0.1 M $HClO_4$ solution at 25 °C with the scan rate of 10 mV/s and the rotation of 1600 rpm.

4.1.4 Change in Mass Activity for ORR During the Potential Cycle Test

In order to quantitatively analyze the change in ORR activity, mass activity at 0.90 V was calculated. Based on ORR measurements at different rotational speeds (400, 900, 1600, and 2500 rpm), Koutecky-Levich plots were plotted and shown in Figure 4.12, 4.13, 4.14, and 4.15 for Pt/VC, Pt/GVC1100, Pt/GVC1600, and Pt/GVC2000, respectively. The value of i_k was determined from the y-value when x = 0. Then, using i_k, mass activity was calculated and plotted in Figure 4.16.

For Pt/Vulcan group electrocatalysts, the similar durability trend of mass activity to ECA was observed. Pt/GVC1600 showed highest mass activity throughout the potential cycle test. The 58% of mass activity was retained even after 60000 cycles, in comparison to only 33% for Pt/VC. The improvement of durability on ORR for Pt/GVC1600 is attributable to the high retention of ECA caused by graphitized carbon surface and sufficient interaction between platinum particles and carbon at the same time.

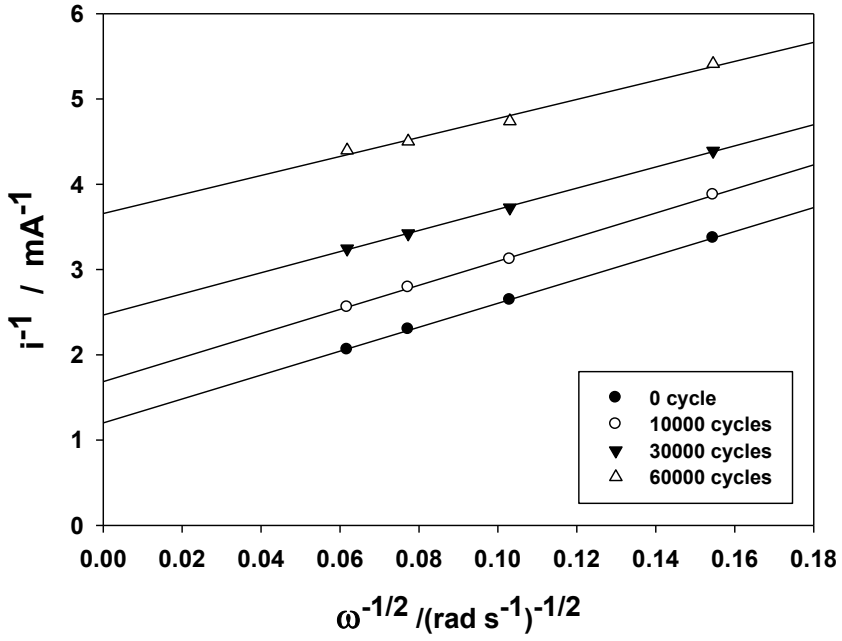

Figure 4.12 Koutecky-Levich plot (at 0.90 V) of Pt/VC after 0, 10000, 30000, 60000 cycles of the potential cycle test.

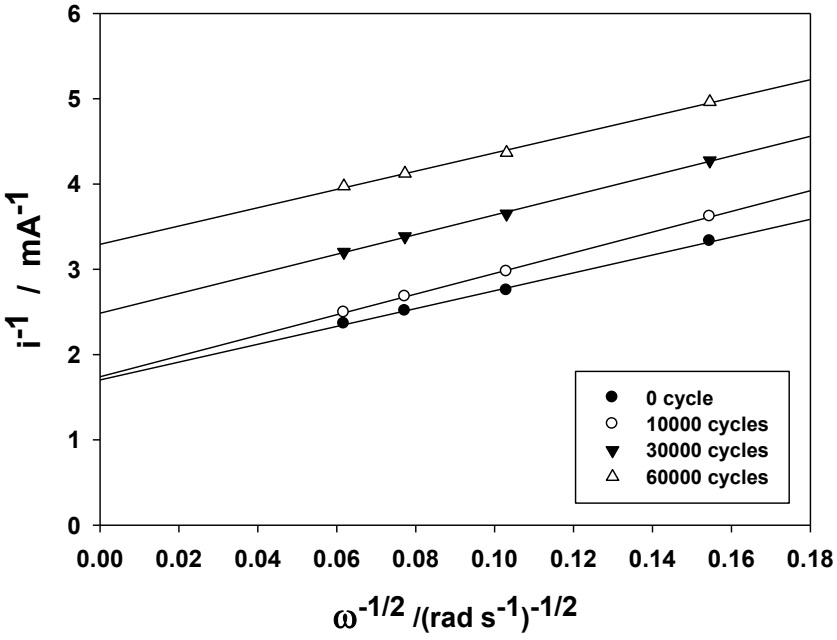

Figure 4.13 Koutecky-Levich plot (at 0.90 V) of Pt/GVC1100 after 0, 10000, 30000, 60000 cycles of the potential cycle test.

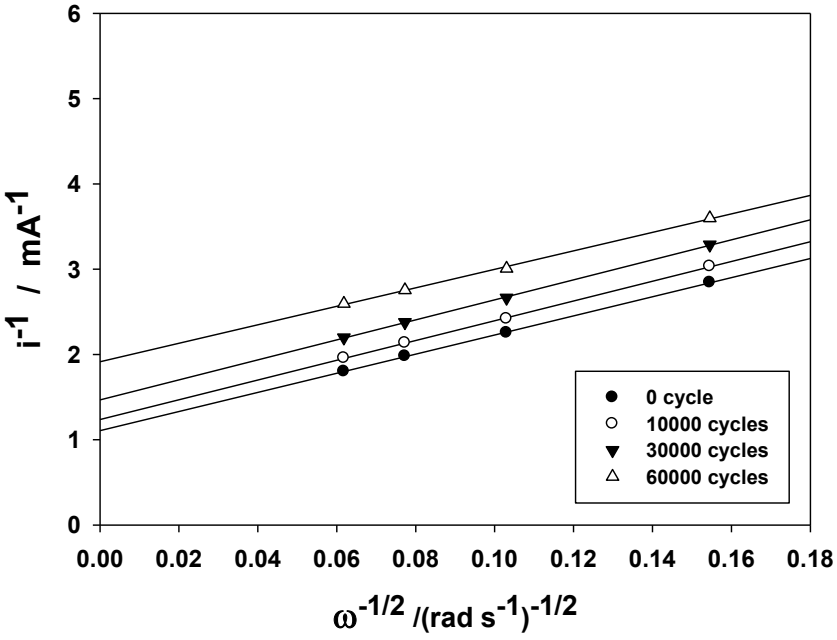

Figure 4.14 Koutecky-Levich plot (at 0.90 V) of Pt/GVC1600 after 0, 10000, 30000, 60000 cycles of the potential cycle test.

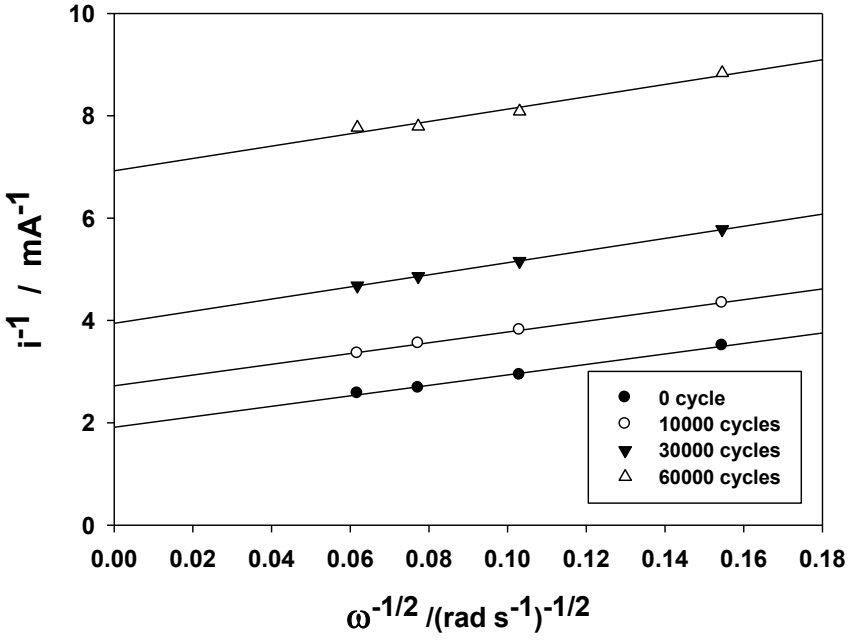

Figure 4.15 Koutecky-Levich plot (at 0.90 V) of Pt/GVC2000 after 0, 10000, 30000, 60000 cycles of the potential cycle test.

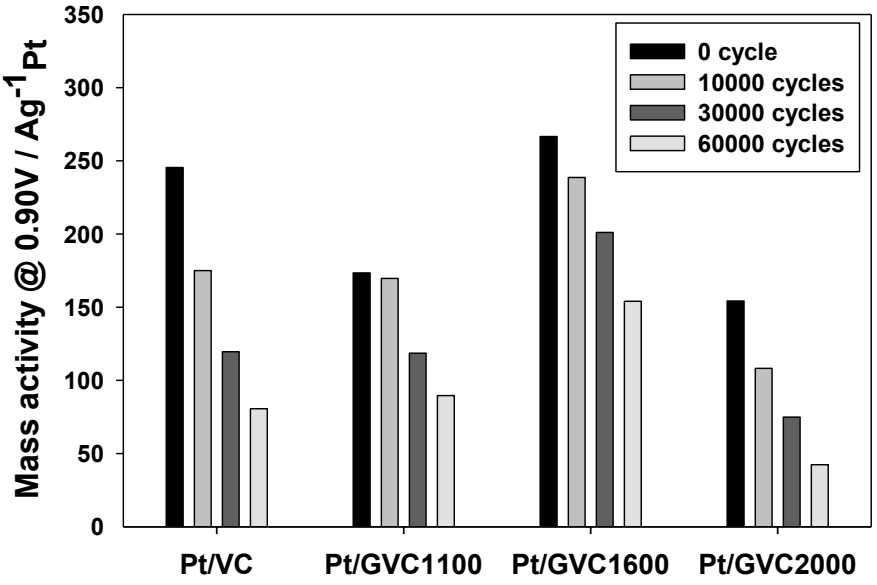

Figure 4.16 Change in ORR mass activity of Pt/VC, Pt/GVC1100, Pt/GVC1600, and Pt/GVC2000 after 0, 10000, 30000, 60000 cycles of the potential cycle test.

4.2 Electrochemical Evaluation of Pt/Ketjen Black Group Electrocatalysts at 25 °C

4.2.1 Change in Cyclic Voltammograms During the Potential Cycle Test

Cyclic voltammograms before and after the potential cycles (10000, 30000, 60000 cycles) for Pt/KB, Pt/GKB1100, Pt/GKB1600, and Pt/GKB2000 are shown in Figure 4.17, 4.18, 4.19, and 4.20, respectively.

Similar to the Pt/Vulcan group, Pt/Ketjen Black group electrocatalysts had a tendency to lose their hydrogen adsorption/desorption and PtO_x formation/reduction peaks after the potential cycle test, but the decreasing rate was different. Also, the peak derived from carbon surface oxidation was rather clearly grown around 0.6 V for the Pt/Ketjen Black group electrocatalysts after the potential cycles. This is probably due to the rough surface of Ketjen Black, leading to high specific surface area. Such a peak was suppressed by heat treatment, which is reasonable for the sample with more graphitized oxidation resistance surface.

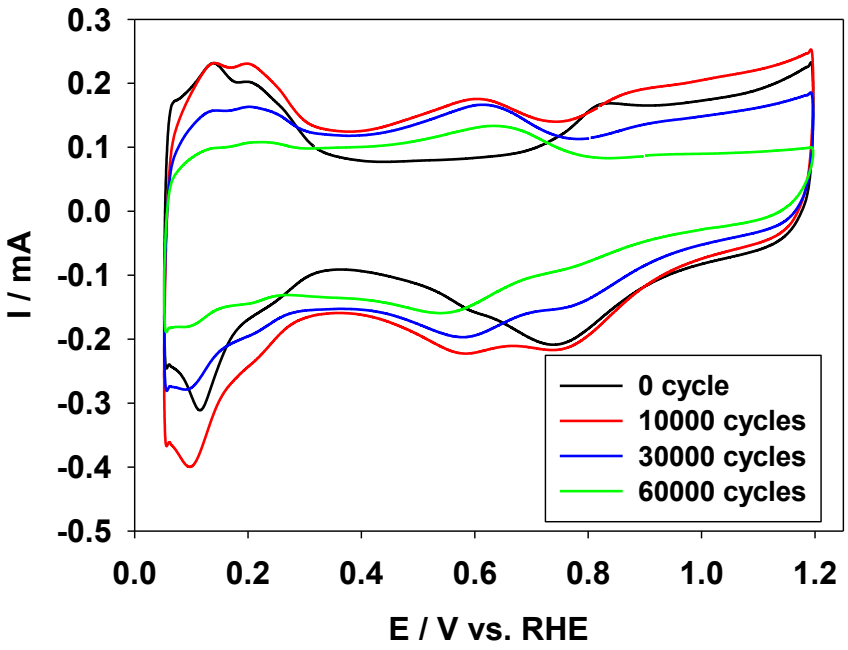

Figure 4.17 Cyclic voltammograms of Pt/KB after 0, 10000, 30000, 60000 cycles of the potential cycle test. Measurements were recorded in N_2 saturated 0.1 M $HClO_4$ solution at 25 °C with the scan rate of 50 mV/s.

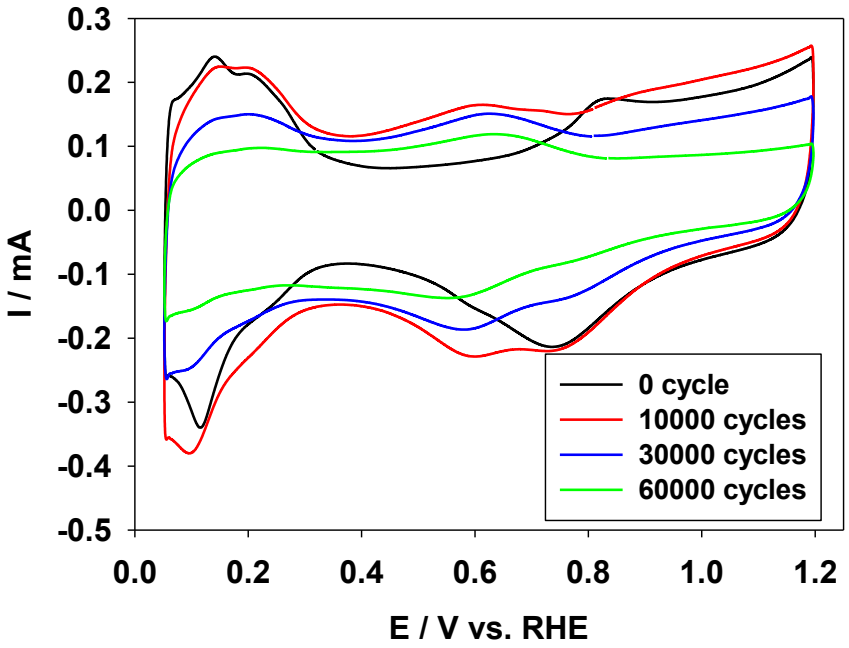

Figure 4.18 Cyclic voltammograms of Pt/GKB1100 after 0, 10000, 30000, 60000 cycles of the potential cycle test. Measurements were recorded in N_2 saturated 0.1 M $HClO_4$ solution at 25 °C with the scan rate of 50 mV/s.

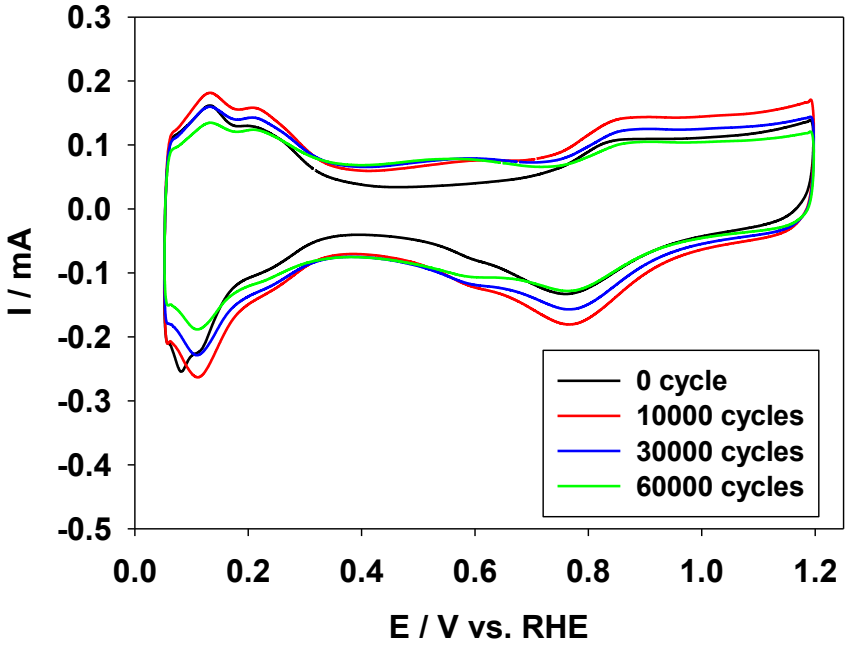

Figure 4.19 Cyclic voltammograms of Pt/GKB1600 after 0, 10000, 30000, 60000 cycles of the potential cycle test. Measurements were recorded in N_2 saturated 0.1 M $HClO_4$ solution at 25 °C with the scan rate of 50 mV/s.

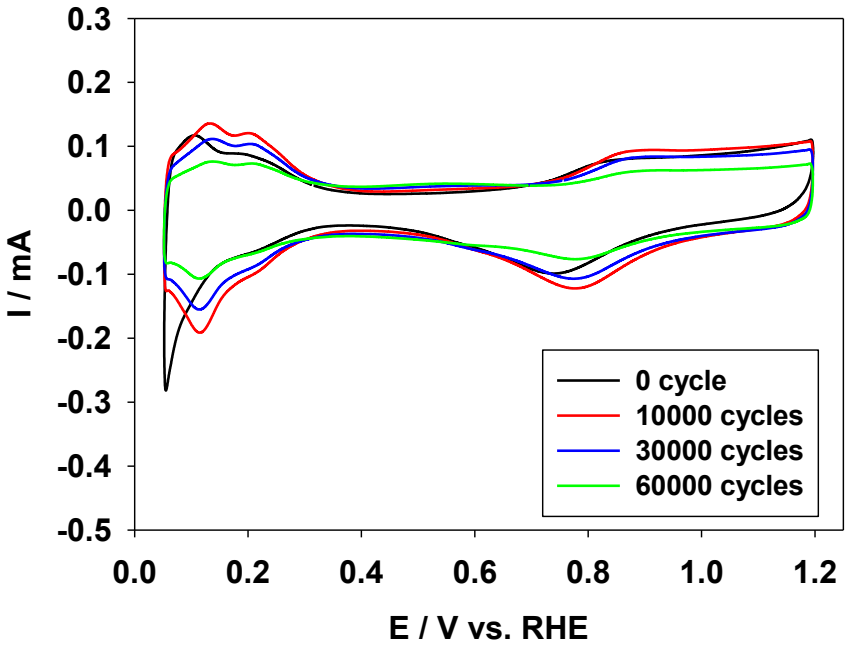

Figure 4.20 Cyclic voltammograms of Pt/GKB2000 after 0, 10000, 30000, 60000 cycles of the potential cycle test. Measurements were recorded in N_2 saturated 0.1 M $HClO_4$ solution at 25 °C with the scan rate of 50 mV/s.

4.2.2 Change in ECA During the Potential Cycle Test

ECAs of these four Pt/C electrocatalysts were then calculated from cyclic voltammogram curves based on the charge associated with hydrogen desorption on platinum. Change in ECA against the number of potential cycle was plotted in Figure 4.21. Initial ECA, maximum ECA, ECA after 60000 cycles, and % retention of ECA ($ECA_{after\text{-}60k\text{-}cycles}$ / ECA_{max}) were also calculated and listed in Table 4.2. The % retention of ECA for the Pt/Ketjen Black group electrocatalysts was confirmed by testing two to three samples for each Pt/C electrocatalyst, and the differences among test remained within a few percent.

As indicated in Figure 4.21, both Pt/GKB1600 and Pt/GKB2000 showed an increase in ECA after the initial several hundred cycles, probably owing to the produced clean platinum surface during the potential cycles. Again, even with similar platinum particle size among the Pt/Ketjen Black group (Table 3.4), relatively low ECA_{max} values of Pt/GKB1600 and Pt/GKB2000 (Table 4.2) were observed owing to the increased aggregation of platinum particles on the smoothened carbon surface, leading to the loss

of sufficient interparticle distance for electrocatalytic reactions.

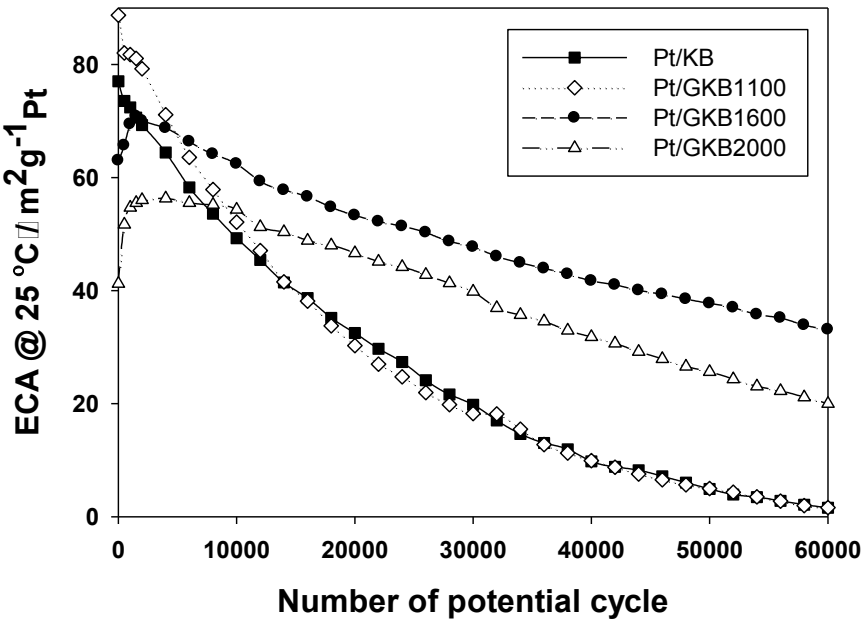

Figure 4.21 Change in ECA during the potential cycle tests for Pt/KB, Pt/GKB1100, Pt/GKB1600, and Pt/GKB2000.

Regarding to durability, Pt/GKB1600 showed the highest retention of ECA (46.8%) after the potential cycle test. In comparison to Pt/KB, the % retention of ECA was very much improved from 2.1% to 46.8%. Pt/KB and Pt/GKB1100 showed almost the same durability. Pt/GKB2000 showed lower durability than Pt/GKB1600 even with increased graphitization degree of GKB2000. Similar reasons to the Pt/Vulcan group, which already discussed in section 4.1.2, can be expected for the Pt/Ketjen Black group.

Table 4.2 ECAs of Pt/Ketjen Black group electrocatalysts.

Pt/C electrocatalyst	Initial ECA (m^2g^{-1})	Max. ECA (m^2g^{-1})	ECA after 60000 cycles (m^2g^{-1})	Retention of ECA (%)
Pt/KB	77.0	77.0	1.6	2.1
Pt/GKB1100	88.7	88.7	1.6	1.8
Pt/GKB1600	63.0	70.8	33.1	46.8
Pt/GKB2000	41.2	56.3	20.0	35.5

Comparing to the Pt/Vulcan group electrocatalysts, Pt/Ketjen Black group showed lowering in durability. This can be explained by the difference of nanostructure between Vulcan and Ketjen Black. BET surface areas for Vulcan and Ketjen Black were very

much different like 225 m^2 g^{-1} and 1280 m^2 g^{-1} (Table 3.1), respectively, owing to a lot more amorphous structure of Ketjen Black. Therefore, Ketjen Black is easily expected to have low oxidation resistivity under a high potential, which is also reported previously [2].

4.2.3 Change in Linear Sweep Voltammograms for ORR During the Potential Cycle Test

ORR measurements were also performed before and after 10000, 30000, and 60000 potential cycles. Figure 4.22, 4.23, 4.24 and 4.25 show the linear sweep voltammograms under the rotation of 1600 rpm at 25 °C for Pt/KB, Pt/GKB1100, Pt/GKB1600, and Pt/GKB2000 electrocatalyst, respectively.

ORR was lost at a certain degree during the potential cycle test, and the rate of loss was different. Pt/GKB1600 (Fig. 4.24) showed the smallest decrease in ORR during the potential cycle test among Pt/Ketjen Black group electrocatalysts.

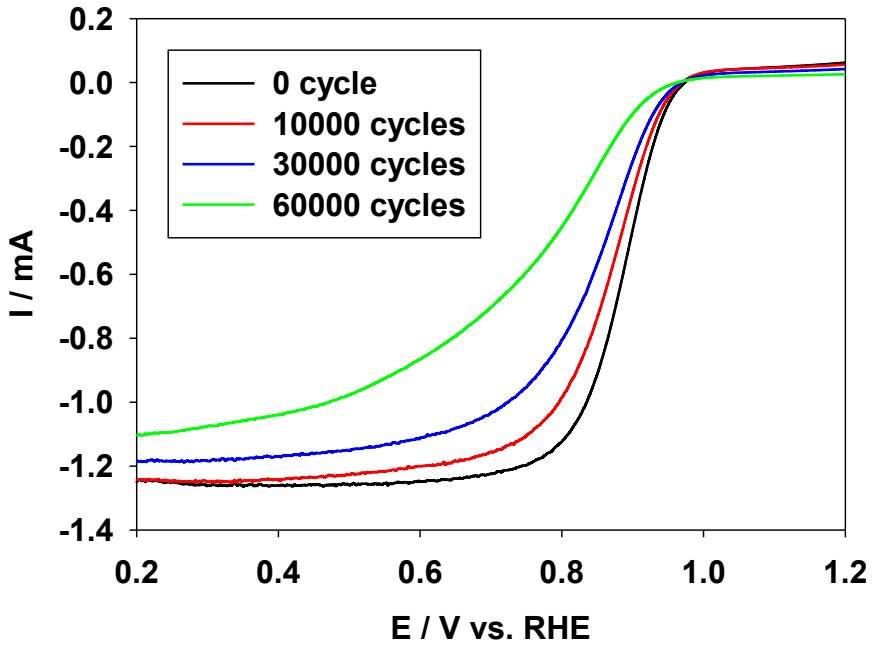

Figure 4.22 Linear sweep voltammograms of Pt/KB after 0, 10000, 30000, 60000 cycles of the potential cycle test. Measurements were recorded in O_2 saturated 0.1 M $HClO_4$ solution at 25 °C with the scan rate of 10 mV/s and the rotation of 1600 rpm.

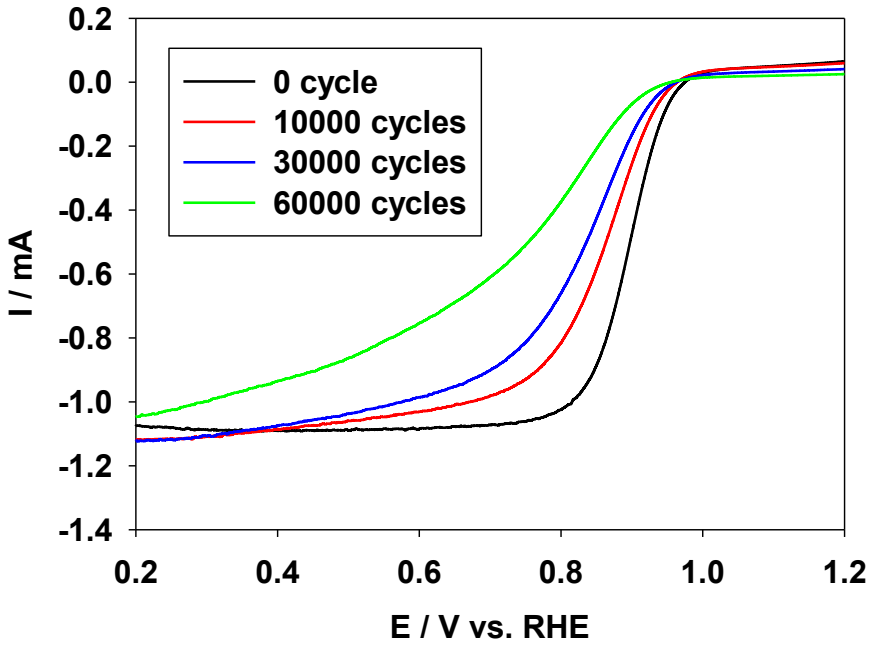

Figure 4.23 Linear sweep voltammograms of Pt/GKB1100 after 0, 10000, 30000, 60000 cycles of the potential cycle test. Measurements were recorded in O_2 saturated 0.1 M $HClO_4$ solution at 25 °C with the scan rate of 10 mV/s and the rotation of 1600 rpm.

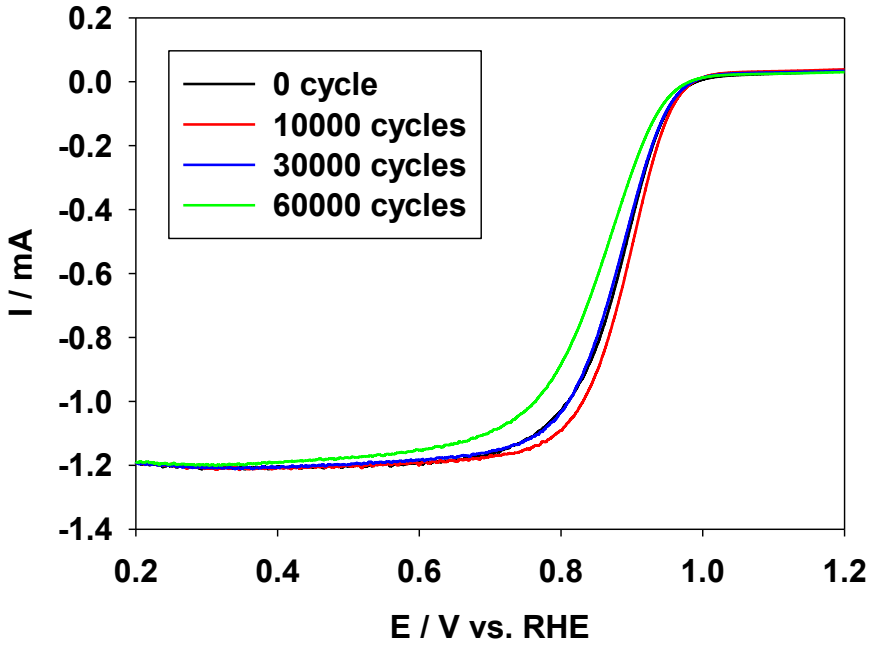

Figure 4.24 Linear sweep voltammograms of Pt/GKB1600 after 0, 10000, 30000, 60000 cycles of the potential cycle test. Measurements were recorded in O_2 saturated 0.1 M $HClO_4$ solution at 25 °C with the scan rate of 10 mV/s and the rotation of 1600 rpm.

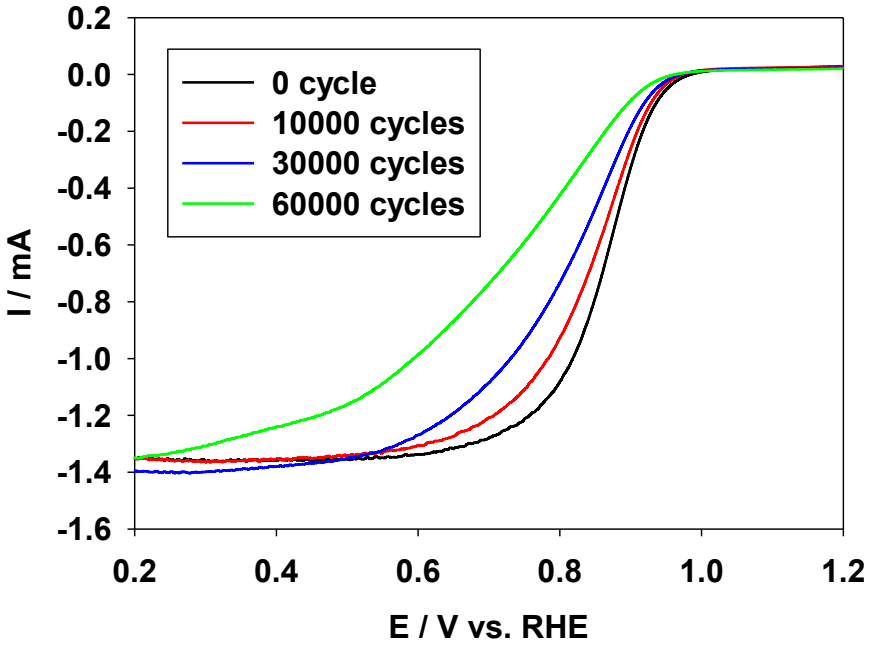

Figure 4.25 Linear sweep voltammograms of Pt/GKB2000 after 0, 10000, 30000, 60000 cycles of the potential cycle test. Measurements were recorded in O_2 saturated 0.1 M $HClO_4$ solution at 25 °C with the scan rate of 10 mV/s and the rotation of 1600 rpm.

4.2.4 Change in Mass Activity for ORR During the Potential Cycle Test

Mass activity at 0.90 V was calculated for the quantitative analysis of ORR. Based on ORR measurements at different rotational speeds (400, 900, 1600, and 2500 rpm), Koutecky-Levich plots were plotted and shown in Figure 4.26, 4.27 4.28 and 4.29 for Pt/KB, Pt/GKB1100, Pt/GKB1600, and Pt/GKB2000, respectively. The value of i_k was determined from the y-value when x = 0. Then, using i_k, mass activity was calculated and plotted in Figure 4.30.

Mass activity of Pt/GKB1600 was the highest throughout the potential cycle test except for the initial activity. This is probably due to the fact that the surface of platinum was not clean enough at the initial stage, leading to lowering ORR activity, and rather clean surface appeared after 10000 cycles, resulting in increasing ORR activity. Regarding to ORR of Pt/KB, Pt/GKB1100, and Pt/GKB2000, the differences among these three samples were not well pronounced in comparison to the differences in ECAs. Consequently, evaluation of ECA by itself is not sufficient enough for studying the durability, and other exploration by ORR and TEM, which will be introduced in chapter 6, is necessary.

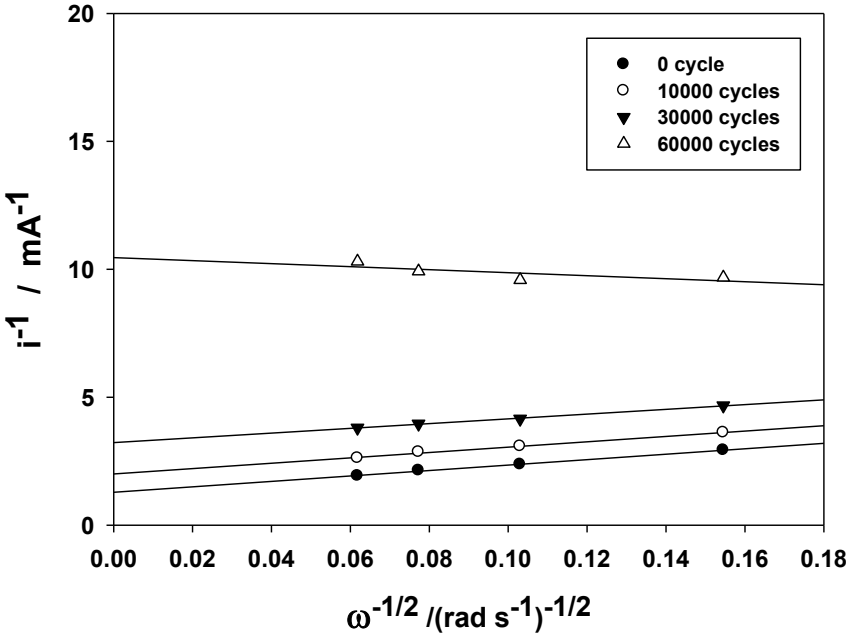

Figure 4.26 Koutecky-Levich plot (at 0.90 V) of Pt/KB after 0, 10000, 30000, 60000 cycles of the potential cycle test.

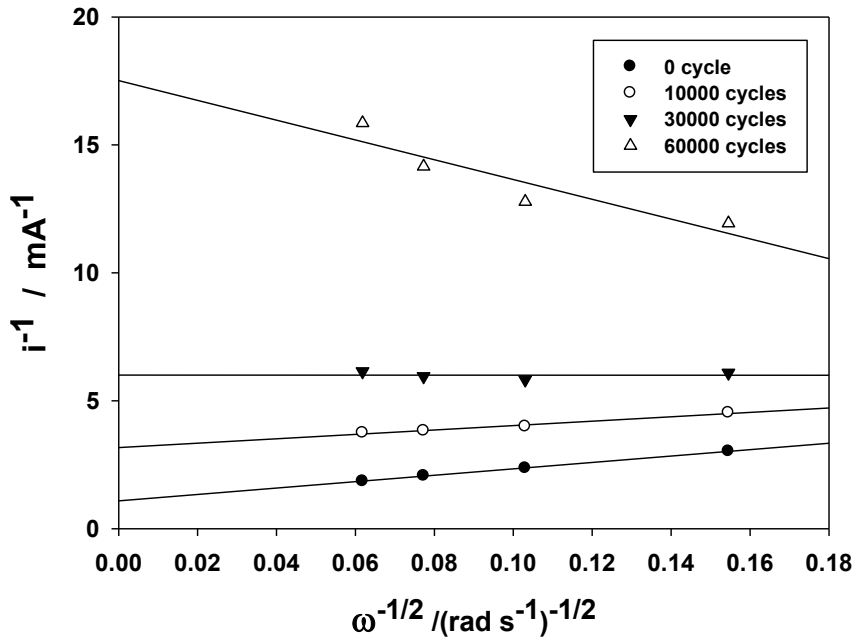

Figure 4.27 Koutecky-Levich plot (at 0.90 V) of Pt/GKB1100 after 0, 10000, 30000, 60000 cycles of the potential cycle test.

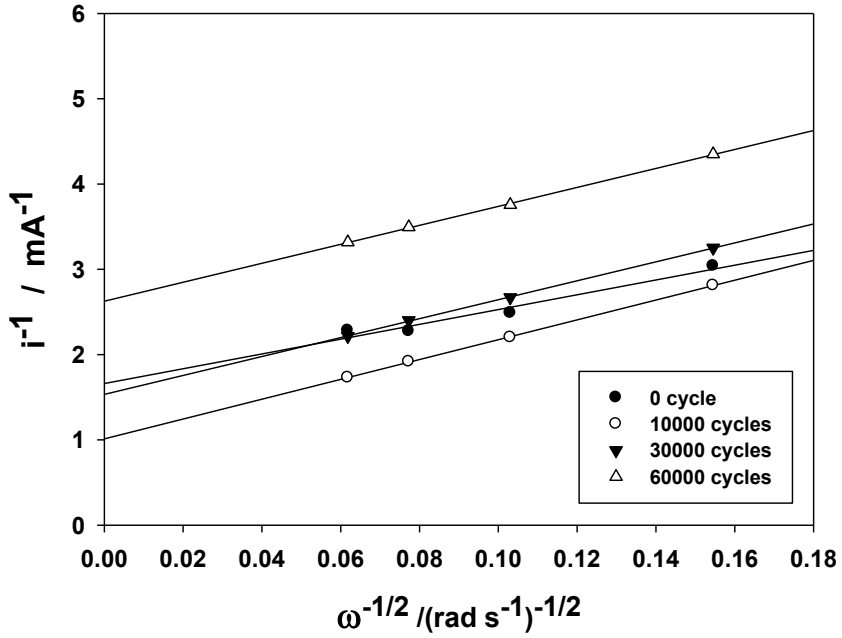

Figure 4.28 Koutecky-Levich plot (at 0.90 V) of Pt/GKB1600 after 0, 10000, 30000, 60000 cycles of the potential cycle test.

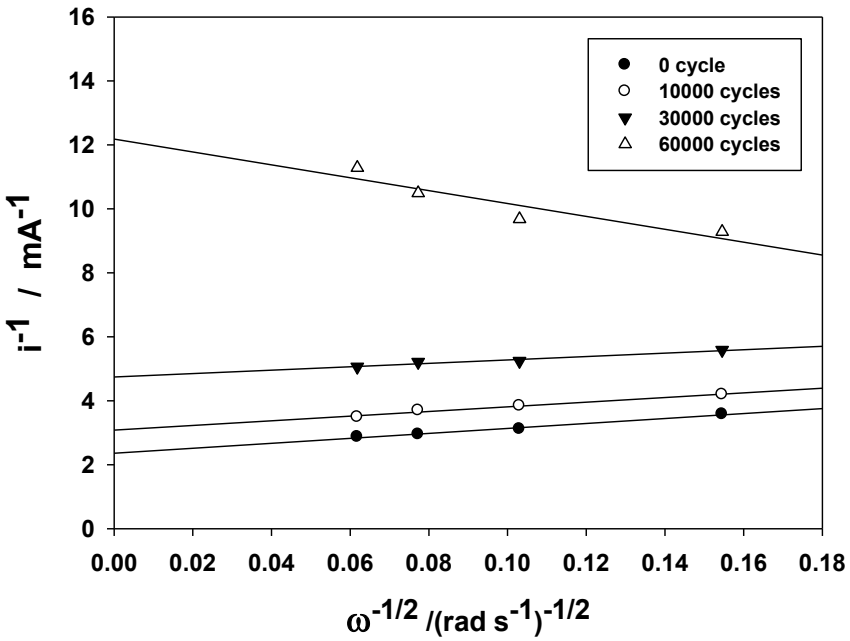

Figure 4.29 Koutecky-Levich plot (at 0.90 V) of Pt/GKB2000 after 0, 10000, 30000, 60000 cycles of the potential cycle test.

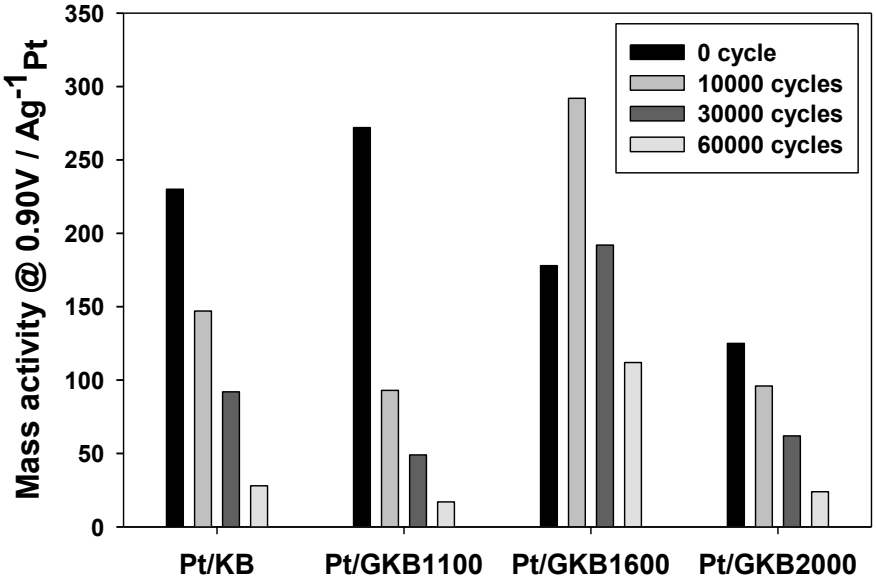

Figure 4.30 Change in ORR mass activity of Pt/KB, Pt/GKB1100, Pt/GKB1600, and Pt/GKB2000 after 0, 10000, 30000, 60000 cycles of the potential cycle test.

4.3 Electrochemical Evaluation of Selected Pt/C Electrocatalysts at 60 °C

Even though the evaluation using a solution half-cell method at room temperature is convenient to study electrocatalytic activity of materials, in reality the operation temperature of PEFC is near 100 °C. It is known that carbon corrosion and performance degradation have strong correlation with operating temperature [3-4]. Therefore, the selected Pt/C electrocatalysts were evaluated at higher temperature, such as 60 °C.

In this study, Pt/GVC1600 and Pt/GKB1600, which had highest durability under the evaluation at 25 °C, were selected for further evaluation at 60 °C together with Pt/VC and Pt/KB. ECA change of these four Pt/C electrocatalysts against the number of potential cycle was plotted in Figure 4.31.

For quantitative comparison, initial ECA and ECA after 10000 and 30000 cycles with corresponding % retention, $ECA_{after\text{-}10k\text{-}cycles}$ / ECA_{ini} and $ECA_{after\text{-}30k\text{-}cycles}$ / ECA_{ini}, are listed in Table 4.3.

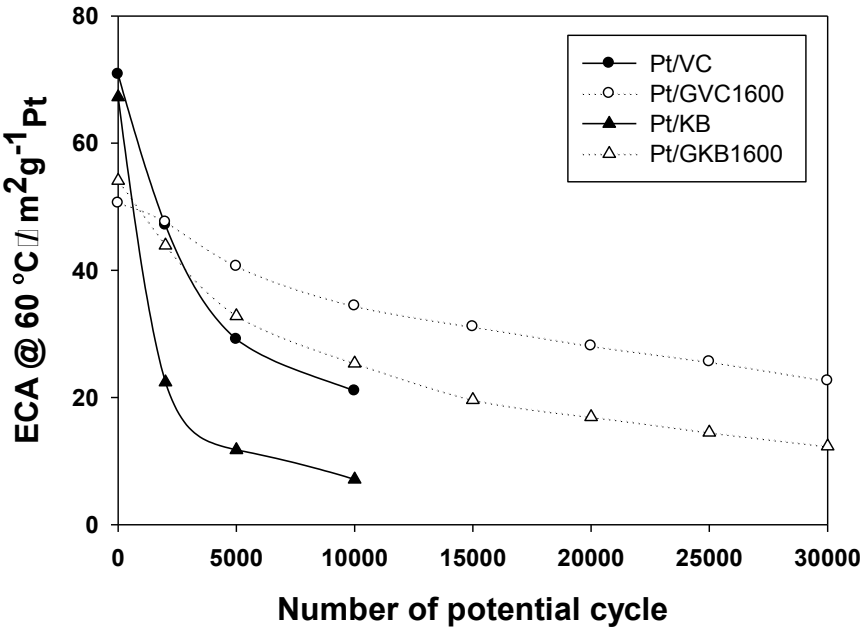

Figure 4.31 Change in ECA during the potential cycle tests for Pt/VC, Pt/GVC1600, Pt/KB, and Pt/GKB1600 at 60 °C.

Table 4.3 ECAs for selected Pt/C electrocatalysts at 60 °C.

Pt/C electrocatalyst	Initial ECA (m^2g^{-1})	After 10000 cycles		After 30000 cycles	
		ECA (m^2g^{-1})	Retention of ECA (%)	ECA (m^2g^{-1})	Retention of ECA (%)
Pt/VC	70.8	21.0	29.7	--	--
Pt/GVC1600	50.6	34.4	70.0	22.6	44.7
Pt/KB	67.3	7.1	10.5	--	--
Pt/GKB1600	54.1	25.4	47.0	12.3	22.7

As seen in Figure 4.31 and Table 4.3, the rate of loss clearly increased for all tested Pt/C electrocatalysts at 60 °C. Non heat-treated samples, Pt/VC and Pt/KB, lost their ECA much faster than heat-treated samples, Pt/GVC1600 and Pt/GKB1600. After 30000 cycles, Pt/GVC1600 and Pt/GKB1600 were still able to keep 44.7% and 22.7% of their original ECAs, respectively. Heat treatment was clearly indicated as a useful tool to increase electrocatalyst's durability even at elevated operational temperature.

4.4 Conclusions

In this chapter, the effect of carbon nanostructure including graphitization degree toward durability has been evaluated using the potential cycle protocol. As a result, both Pt/GVC1600 and Pt/GKB1600 showed the highest ECA retention and ORR activity after the potential cycle test among Pt/Vulcan and Pt/Ketjen Black group electrocatalysts, respectively. Here, the importance of carbon nanostructure including graphitization degree for the durability has clearly been demonstrated. Comparing to Vulcan and Ketjen Black, Vulcan showed higher durability than Ketjen Black, owing to much different nanostructures. In case of Ketjen Black, its amorphous structure with high specific surface area was more easily oxidized. Regarding to graphitization degree, as expected, higher graphitization degree lead to improving corrosion resistance, but at the same time resulted in increasing the mobility of platinum particles on carbon supports. Consequently, the optimum heat treatment condition with both high corrosion resistance and sufficient interaction between platinum particles and carbon support was found to be 1600 °C, among 1100 °C, 1600 °C and 2000 °C.

References

[1] M. Watanabe, H. Sei, P. Stonehart, The influence of platinum crystallite size on the electroreduction of oxygen, J. Electroanal. Chem., 261 (1989) 375.

[2] M. Wang, Q. Liu, H. Sun, N. Ogbeifun, F. Xu, E.A. Stach, J. Xie, Investigation of carbon corrosion in polymer electrolyte fuel cells using steam etching, Materials Chemistry and Physics, 123 (2010) 761.

[3] K. H. Lim et al., Effect of operating conditions on carbon corrosion in polymer electrolyte membrane fuel cells, J. Power Source, 193 (2009) 575.

[4] Y. Y. Jo et al., Degradation of polymer electrolyte membrane fuel cells repetitively exposed to reverse current condition under different temperature, J. Power Source, 196 (2011) 9906.

[5] Y. Chen, J. Wang, H. Liu, R. Li, X. Sun, S. Ye, S. Knights, Enhanced stability of Pt electrocatalysts by nitrogen doping in CNTs for PEM fuel cells, Electrochemistry Communications, 11 (2009) 2071.

[6] P. Joghee, S. Pylypenko, T. Olson, A. Dameron, A. Corpuz, H.N. Dinh, K. Wood, K. O'Neill, K. Hurst, G. Bender, Enhanced stability of PtRu supported on N-doped carbon for the anode of a DMFC, J. Electrochemical Society, 159 (2012) F768.

[7] X. Tuaev, J.P. Paraknowitsch, R. Illgen, A. Thomas, P. Strasser, Nitrogen-doped coatings on carbon nanotubes and their stabilizing effect on Pt nanoparticles, Physical Chemistry Chemical Physics, 14 (2012) 6444.

Chapter 5

Evaluation of MEAs

During the evaluation of prepared Pt/C electrocatalysts using the half-cell method in chapter 4, we have found that an Pt/C electrocatalyst made by heat treatment of Vulcan carbon at 1600 °C, Pt/GVC1600, reveals much more improved durability than the any other Pt/C electrocatalysts. This result has further suggested us to characterize Pt/GVC1600 under an actual PEFC operational condition.

In this chapter, membrane electrode assembles (MEAs) were developed with Pt/GVC1600 and also Pt/VC for the cathode and evaluated in terms of electrochemical activity and durability similar to the half-cell experiments in the previous chapter.

5.1 Preparation of Catalyst Layers

Sufficient amount of Nafion ionomer is essential within the catalyst layers of MEAs to produce high performance. Insufficient Nafion leads to suppress the proton transfer necessary for electrochemical reactions. On the other hand, too much Nafion may block the mass transfer for both gas and water.

Previously reported studies on the optimization of Nafion content in MEAs have suggested that the optimized Nafion content depends on the MEA fabrication parameters (platinum weight percent against carbon support, platinum loading amount on catalyst layer, and solvent used for electrocatalyst slurry) and techniques used in MEA preparation [1-5]. The optimum Nafion content reported by various researchers is summarized in Table 5.1. Therefore, in this study, the sufficient amount of Nafion content was also evaluated for both anode and cathode catalyst layers.

This chapter has been submitted to Zhao et al., *ECS Trans*. 2013 Vol.58.

Table 5.1 Summary of optimized Nafion content reported by various researchers.

No.	Pt / (Pt + C) (wt%)	Pt loading (mg cm^{-2})	Optimum Nafion / (Nafion + Pt + C) (wt%)	Reference
1	25	0.5	33	Uchida [1]
2	20	0.2	40	Antolini [2]
3	20	0.1	33	Passalacqua[3]
4	45.5	0.4	25 (anode)/30 (cathode)	Kun-Ho Kim [4]
5	10	0.4	30 - 35	Paganin [5]

5.1.1 Evaluation of Sufficient Nafion Amount for the Anode Catalyst Layer

For the anode, a commericial electrocatalyst, TEC10E50E (Platinum loading of 46.2%), was used. On consideration of the Nafion content suggested by others (Table 5.1), Nafion content was controlled to 28, 30, and 33% against the total content (Nafion + Pt + C). Cathode layer was made by exactly the same way as the anode. I-V characteristics of resulting MEA are shown in Figure 5.1.

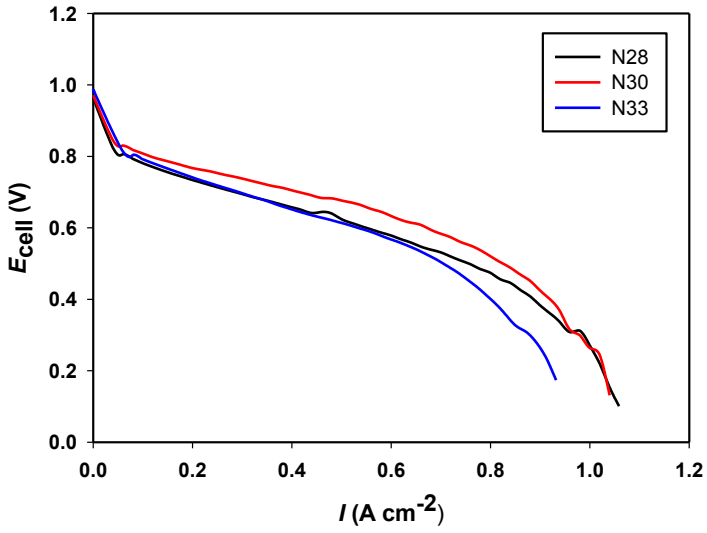

Figure 5.1 I-V characteristics of MEA with different Nafion contents for both anode and cathode with a standard electrocatalyst, TEC10E50E. Platinum loading was kept to 0.3 mg cm^{-2} in all the cases. Measurements were done at the cell temperature of 80 °C under the flow of 100% humidified H_2 and air into the anode and the cathode, respectively, with a constant flow rate of 100 cc min^{-1}.

In the case that 30% Nafion was used, the I-V characteristics were the best throughout the tested current range. Therefore, the Nafion content for the anode catalyst layer was kept to 30% throughout this study.

5.1.2 Evaluation of Sufficient Nafion Amount for the Cathode Catalyst Layer with Pt/VC

Considering the relatively small BET surface area of Vulcan, Nafion content for Pt/VC cathode layer was controlled to 30% or lower (24% and 16%) against the total content (Nafion + Pt + C). I-V characteristics of resulting MEA are shown in Figure 5.2.

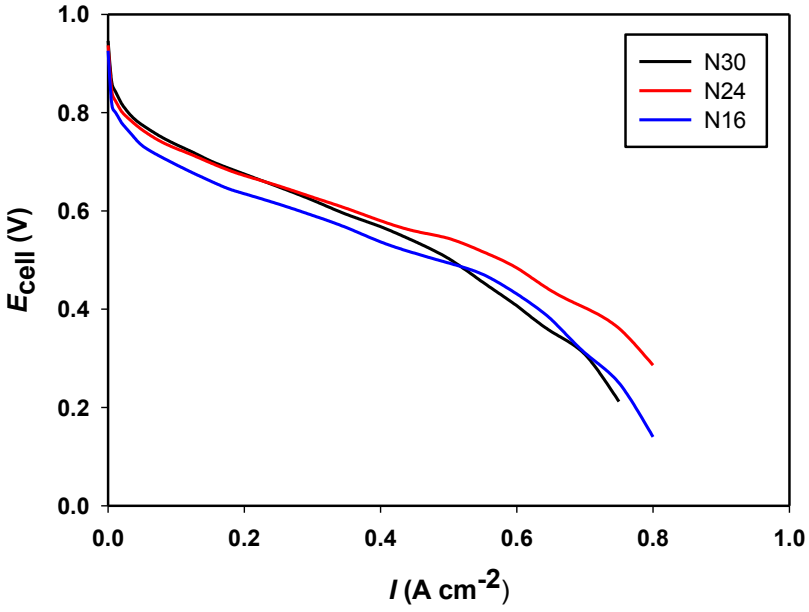

Figure 5.2 I-V characteristics of MEA with different Nafion contents for the cathode catalyst layer with Pt/VC. Platinum loading was kept to 0.3 mg cm^{-2} in all the cases. Measurements were done at the cell temperature of 80 °C under the flow of 100% humidified H_2 and air into the anode and the cathode, respectively, with a constant flow rate of 100 cc min^{-1}.

As seen in Figure 5.2, the Nafion content of both 30 and 24% resulted in the similar I-V curve above 0.6 V. However, below 0.6 V the current decreased when the Nafion content of 30% was used.

Further, cross-sectional SEM observation was performed for cathode catalyst layer with different Nafion contents, and the SEM micrographs are shown in Figure 5.3.

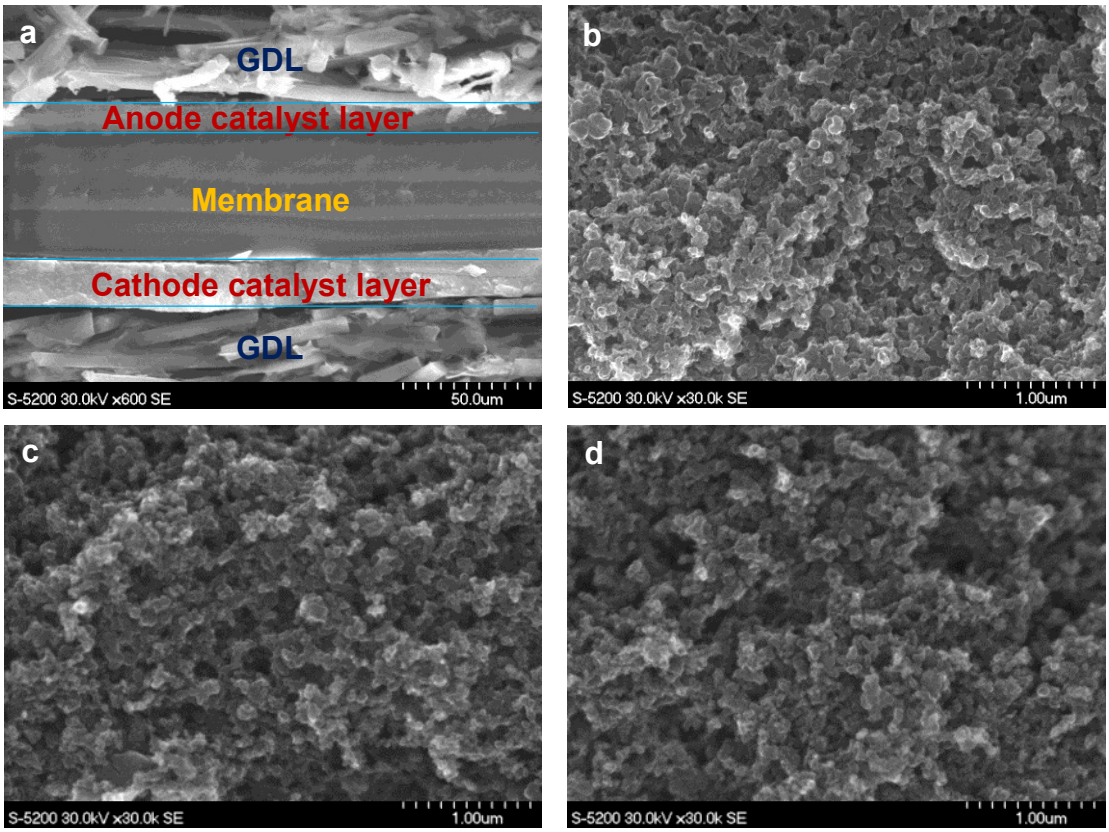

Figure 5.3 SEM images of cross section of MEA (a) and Pt/VC cathode catalyst layers with different Nafion contents (30% (b), 24% (c), and 16% (d)).

Figure 5.3a shows a cross-sectional SEM image of MEA, in which three layers are composed of anode catalyst layer, Nafion membrane, and cathode catalyst layer, sandwiched by the gas diffusion layers (GDLs). In Figure 5.3c and 5.3d, the well-developed porous structure of cathode catalyst layers was identified. However, comparing to these two figures, Figure 5.3b showed that some of gas channels were rather covered by excess Nafion, resulting in a less porous structure. This is a possible reason for reduced current below 0.6 V with 30% Nafion. Consequently, Nafion content for Pt/VC cathode catalyst layer was kept to 24% throughout this study.

5.1.3 Evaluation of Sufficient Nafion Amount for the Cathode Catalyst Layer with Pt/GVC1600

Since the specific surface area of GVC1600 was reduced by the heat treatment, the Nafion content for Pt/GVC1600 cathode catalyst layer was controlled to 24% or lower like 20%. I-V characteristics of resulting MEA are shown in Figure 5.4. Cross-sectional

SEM observation of cathode catalyst layers was also performed, and resulting SEM images are shown in Figure 5.5.

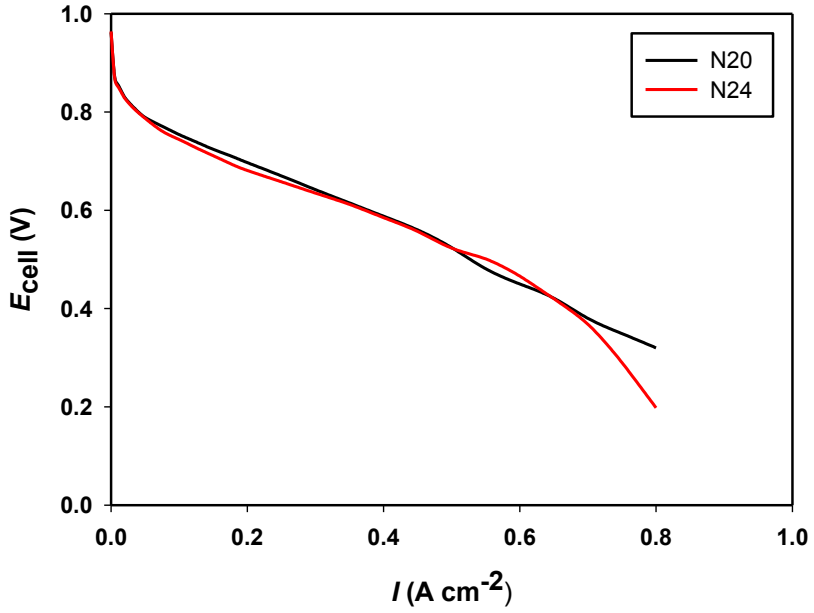

Figure 5.4 I-V characteristics of MEA with different Nafion contents for the cathode catalyst layer with Pt/GVC1600. Platinum loading was kept to 0.3 mg cm^{-2} in all the cases. Measurements were done at the cell temperature of 80 °C under the flow of 100% humidified H_2 and air into the anode and the cathode, respectively, with a constant flow rate of 100 cc min^{-1}.

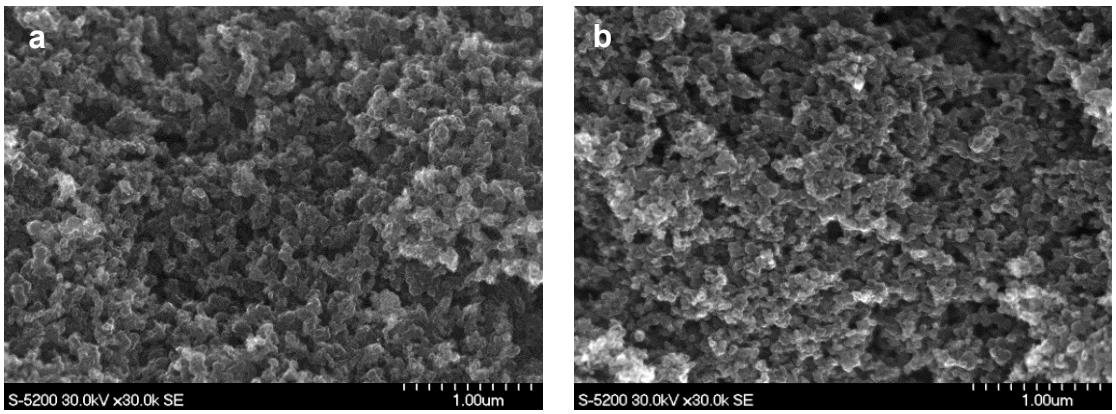

Figure 5.5 SEM images of Pt/GVC1600 cathode catalyst layers with different Nafion contents (24% (a), and 20% (b)).

Both I-V characteristics (Figure 5.4) and SEM images (Figure 5.5) did not show much difference between 24% and 20% of the Nafion content. Therefore, in this study, Nafion content in the Pt/GVC1600 cathode catalyst layer was rather kept to 24% as the same as in Pt/VC cathode.

5.2 Electrochemical Evaluation of MEAs

MEAs were prepared with TEC10E50E as an anode and with Pt/VC or Pt/GVC1600 as a cathode. The amount of Nafion in the catalyst layer was kept to be 30% and 24% for the anode and the cathode, respectively. Then, I-V performance and durability of MEAs were examined.

5.2.1 I-V Characteristics

I-V characteristics of MEAs with Pt/VC and Pt/GVC1600 cathode catalyst layers are shown in Figure 5.6. Their I-V curves were very similar to each other, which can be expected from the comparable initial mass activities for ORR as already shown in Figure 4.16.

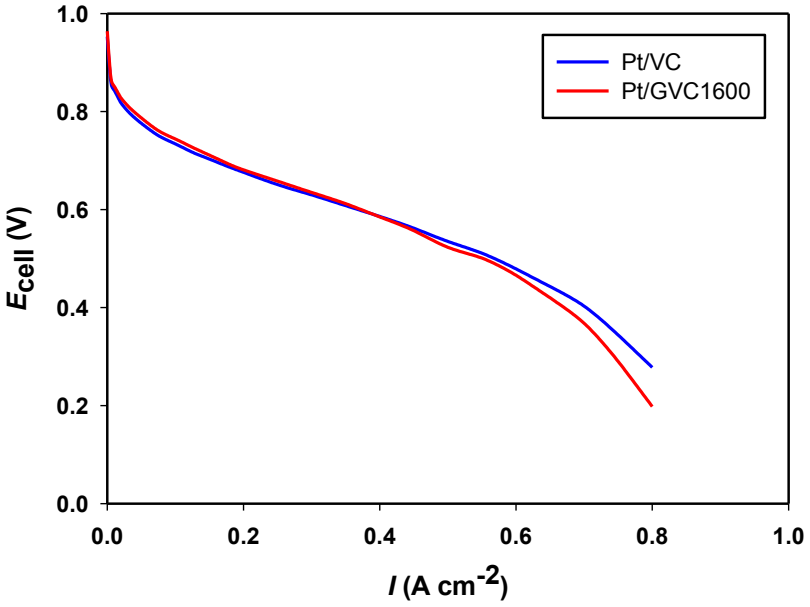

Figure 5.6 I-V characteristics of MEA with Pt/VC (blue) and Pt/GVC1600 (red) for the cathode. Platinum loading was kept to 0.3 mg cm^{-2} in all the cases. Measurements were done at the cell temperature of 80 °C under the flow of 100% humidified H_2 and air into the anode and the cathode, respectively, with a constant flow rate of 100 cc min^{-1}.

For further comparison, ohmic resistance of the cell, the anode, and the cathode was separated through a current interrupt technique, and the results are listed in Table 5.2.

Table 5.2 Ohmic resistance of MEAs with Pt/VC and Pt/GVC1600 cathode layer.

	MEA with Pt/VC (Ωcm^2)	**MEA with Pt/GVC1600 (Ωcm^2)**
Cell ohmic resistance	0.19	0.21
Anode ohmic resistance	0.06	0.06
Cathode ohmic resistance	0.13	0.15

Although cathode ohmic resistance was slightly higher for Pt/GVC1600 than for Pt/VC, the difference remained within the variation of individual MEAs. Therefore, the initial performance of MEAs made with two different electrocatalysts, Pt/VC and Pt/GVC1600, was almost the same.

5.2.2 Change in I-V Characteristics During the Potential Cycle Test

In order to evaluate the durability of MEAs, potential cycling between 1.0 and 1.5 V vs. RHE was applied to MEAs based on the protocol explained in section 2.4.5. Changes in I-V characteristics of MEAs with Pt/VC and Pt/GVC1600 cathode are shown in Figure 5.7 and 5.8, respectively.

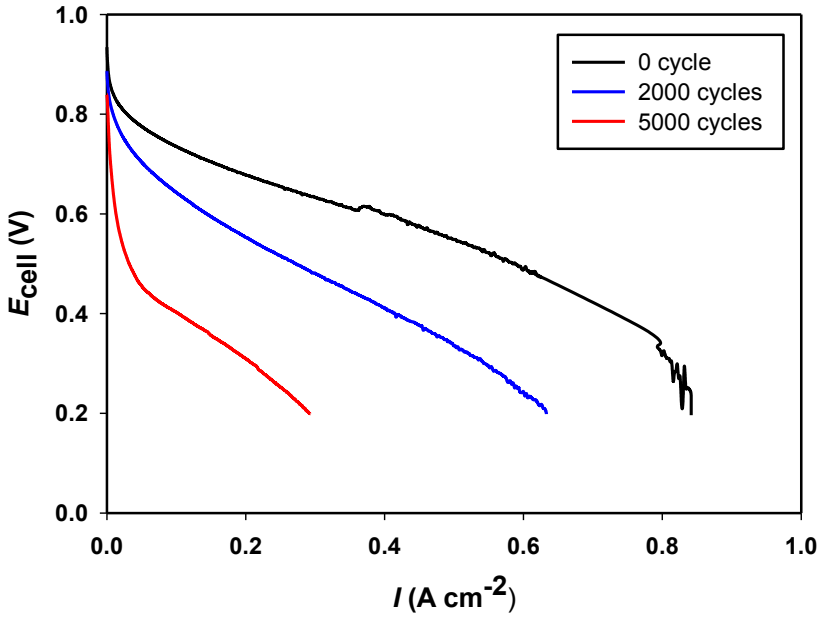

Figure 5.7 Change in I-V characteristics during the potential cycling between 1.0 and 1.5 V vs. RHE for MEA with Pt/VC. Platinum loading was kept to 0.3 mg cm^{-2} in all the cases. I-V measurements were done at the cell temperature of 80 °C under the flow of 100% humidified H_2 and air into the anode and the cathode, respectively, with a constant flow rate of 100 cc min^{-1}.

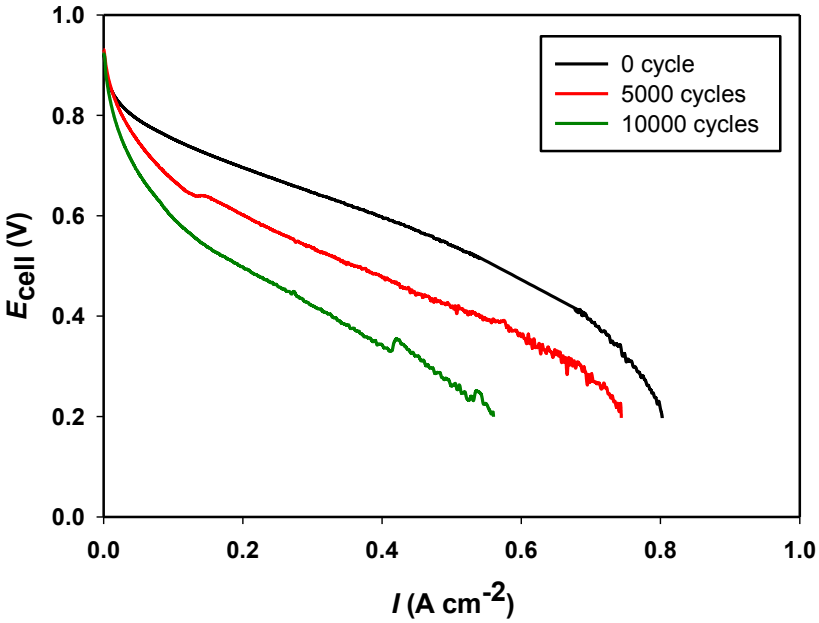

Figure 5.8 Change in I-V characteristics during the potential cycling between 1.0 and 1.5 V vs. RHE for MEA with Pt/GVC1600. Platinum loading was kept to 0.3 mg cm^{-2} in all the cases. I-V measurements were done at the cell temperature of 80 °C under the flow of 100% humidified H_2 and air into the anode and the cathode, respectively, with a constant flow rate of 100 cc min^{-1}.

MEA with Pt/VC lost most of its initial I-V performance after 5,000 potential cycles as shown in Figure 5.7. On the other hand, MEA with Pt/GVC1600 much more gradually lost its initial performance as shown in Figure 5.8. In order to compare the durability between two samples more quantitatively, cell voltages of Pt/VC and Pt/GVC1600 at 0.2 A cm^{-2} are listed in Table 5.3.

Table 5.3 Changes in cell voltage of MEAs with Pt/VC and Pt/GVC1600 during the potential cycle test.

	Pt/VC		**Pt/GVC1600**	
	E_{cell} @ 0.2 A/cm^2, V	**Retention of E_{cell} (%)**	**E_{cell} @ 0.2 A/cm^2, V**	**Retention of E_{cell} (%)**
0 cycle	0.678	--	0.696	--
5000 cycles	0.309	45.6	0.602	86.5
10000 cycles	--	--	0.499	71.7

Regarding to cell voltages after 5,000 cycles, the cell voltage of MEA with Pt/GVC1600, 0.602 V, was significantly higher than that of MEA with Pt/VC, 0.309 V.

Even after 10,000 potential cycles, the resulting cell voltage of Pt/GVC1600 was 0.499 V, and 71.7% of the initial cell voltage was retained. These consequences have agreed with the results obtained from the half-cell evaluation in the previous study. Graphitized surface certainly increased the durability. However, degradation rate was much larger for MEA analyses. The main reasons for faster degradation come from the operation at different temperatures, 25 °C for the half-cell tests and 80 °C for the full-cell tests. Increase in degradation rate at an elevated temperature was also observed in our half-cell study.

In order to compare with the report by others [6], the retention of current density at 0.85 V and evaluated condition are summarized in Table 5.4. Although MEA with our electrocatalyst shows lower retention of current density without heat treatment, similar retention is observed with graphitized carbon. The resulting difference is probably owing to different conditions for potential cycle test and also different carbon sources used in each study. Consequently, similar improvement has been observed even though the evaluated conditions are slightly different. Therefore, our results are reasonable, and so MEA with improved durability has successfully been achieved with the appropriate heat treatment.

Table 5.4 Comparison of MEA performance with other studies.

Cathode electrocatalysts	$j_{0.85\,V}$ (A/cm^2)		Retention of $j_{0.85\,V}$ (%)	Conditions for potential cycle test
	Initial	After		
c-Pt/CB*	0.0441	0.0098	22.2	65 °C, 0.9-1.3 V, 3000 cycles
c-Pt/GCB*	0.0291	0.0177	60.8	65 °C, 0.9-1.3 V, 10000 cycles
Pt/VC	0.0070	0.0002**	3.0**	80 °C, 1.0-1.5 V, 5000 cycles
Pt/GVC1600	0.0108	0.0069	63.9	80 °C, 1.0-1.5 V, 10000 cycles

* The values for these electrocatalysts were obtained from ref [6].

**Current density at 0.84 V was in use.

5.3 Conclusions

In this chapter, sufficient amount of Nafion in the anode and the cathode layer was examined. In our study, 30% and 24% as the Nafion content were determined as appropriate amount for the anode and the cathode, respectively.

With the sufficient Nafion content, MEAs were developed using TEC10E50E for the anode and Pt/VC or Pt/GVC1600 for the cathode. Then, I-V characteristics and durability of MEAs were evaluated. Although the initial performance was almost the same for MEAs with Pt/VC and Pt/GVC1600, regarding to durability, Pt/GVC1600 showed much more improvement than Pt/VC. Results from MEA evaluation have demonstrated that heat treatment of carbon supports at an optimum temperature leads to increase in durability even under the actual PEFC operational condition.

References

[1] M. Uchida, Y. Aoyama, N. Eda, A. Ohta, Investigation of the microstructure in the catalyst layer and effects of both perfluorosulfonate ionomer and PTFE-loaded carbon on the catalyst layer of polymer electrolyte fuel cells, J. Electrochem. Soc., 142 (1995) 4143.

[2] E. Antolini, L. Giorgi, A. Pozio, E. Passalacqua, Influence of Nafion loading in the catalyst layer of gas-diffusion electrodes for PEFC, J. Power Sources, 77 (1999) 136.

[3] E. Passalacqua, F. Lufrano, G. Squadrito, A. Patti, L. Giorgi, Nafion content in the catalyst layer of polymer electrolyte fuel cells: effects on structure and performance, Electrochimica Acta, 46 (2001) 799.

[4] Kun-Ho Kimet al. The effects of Nafion ionomer content in PEMFC MEAs prepared by a catalyst-coated membrane (CCM) spraying method, J. Hydrogen energy, 35 (2010) 2119.

[5] V.A. Paganin, E.A. Ticianelli, E.R. Gonzalez, Development and electrochemical studies of gas diffusion electrodes for polymer electrolyte fuel cells, J. Appl. Electrochem., 26 (1996) 297.

[6] M. Hara, M. Lee, C. Liu, B. Chen, Y. Yamashita, M. Uchida, H. Uchida, M. Watanabe, Electrochemical and Raman spectroscopic evaluation of Ptgraphitized carbon black catalyst durability for the start/stop operating condition of polymer electrolyte fuel cells, Electrochimica Acta, 70 (2012) 171.

Chapter 6

Degradation Mechanism for Pt/C Electrocatalysts

During the analyses by solution half-cell (Chapter 4) and solid full-cell (Chapter 5) methods, the nanostructure of electrocatalysts was found to be most likely an important factor for their durability. In this chapter, nanostructures are evaluated in detail to understand the possible degradation mechanism through both ex-situ and in-situ electromicroscopy methods.

6.1 Degradation of Pt/C Electrocatalysts in Half-cell Reactions

For all of the eight kinds of Pt/C electrocatalysts, TEM images before and after 60000 cycles of the potential cycle test were observed to understand the change in their nanostructures using transmission electron microscopy.

6.1.1 Evaluation of Pt/Vulcan Group Electrocatalysts by Ex-situ TEM Observation

Figure 6.1, 6.2, 6.3, and 6.4 show TEM images of Pt/VC, Pt/GVC1100, Pt/GVC1600, and Pt/GVC2000, respectively.

A part of this chapter has been published in Zhao et al., *J. Electrochimica Acta* 97 (2013) 33-41, and Zhao et al., ECS Trans. 2013 53 (12) 23-29, and also submitted to Zhao et al., ECS Trans. 2013 Vol.58.

Regarding to the images at the initial stage, platinum particles with almost the same size were evenly distributed on carbon supports for Pt/VC (Figure 6.1a) and Pt/GVC1100 (Figure 6.2a). By carefully looking at the initial image of Pt/GVC1600 (Figure 6.3a), the graphite-like layers on the surface of carbon support were clearly observed, which was briefly mentioned in section 3.2.2. Platinum particles were adequately dispersed on the carbon, even though the aggregation of platinum slightly appeared. Therefore, TEM images also clearly support that heat treatment at an adequate temperature makes it possible to have graphitized carbon surface and sufficient interaction of platinum particles and carbon at the same time.

On the other hand, Pt/GVC2000 as shown in Figure 6.4a, carbon seemed graphitized, but at the same time, sufficient interaction between platinum particles and carbon support was lost. Platinum particles were not evenly deposited and rather agglomerated on certain spots, which again explains decreased ECA shown in Table 4.1, despite the presence of considerably small size of platinum particles.

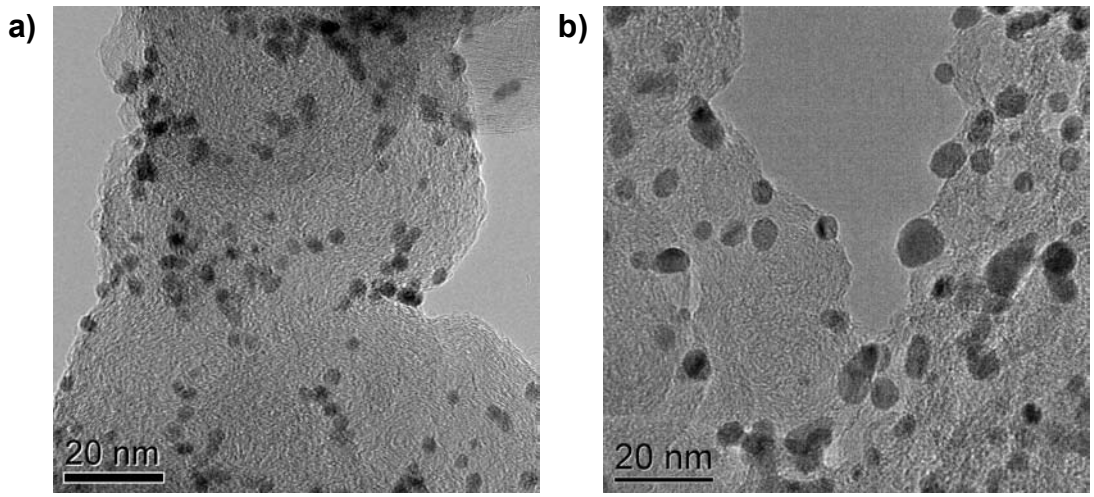

Figure 6.1 TEM images of Pt/VC before (a) and after (b) 60000 cycles of the potential cycle test.

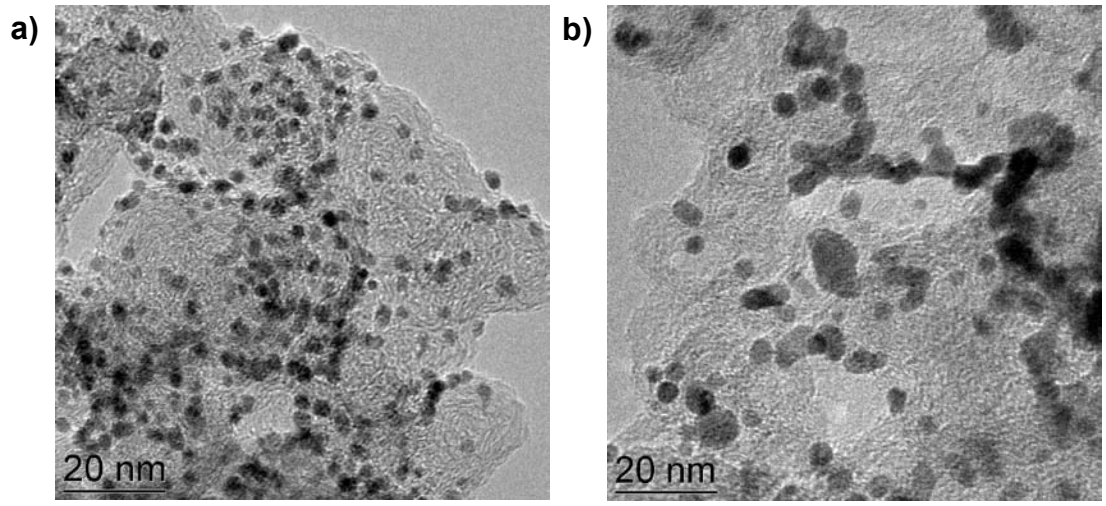

Figure 6.2 TEM images of Pt/GVC1100 before (a) and after (b) 60000 cycles of the potential cycle test.

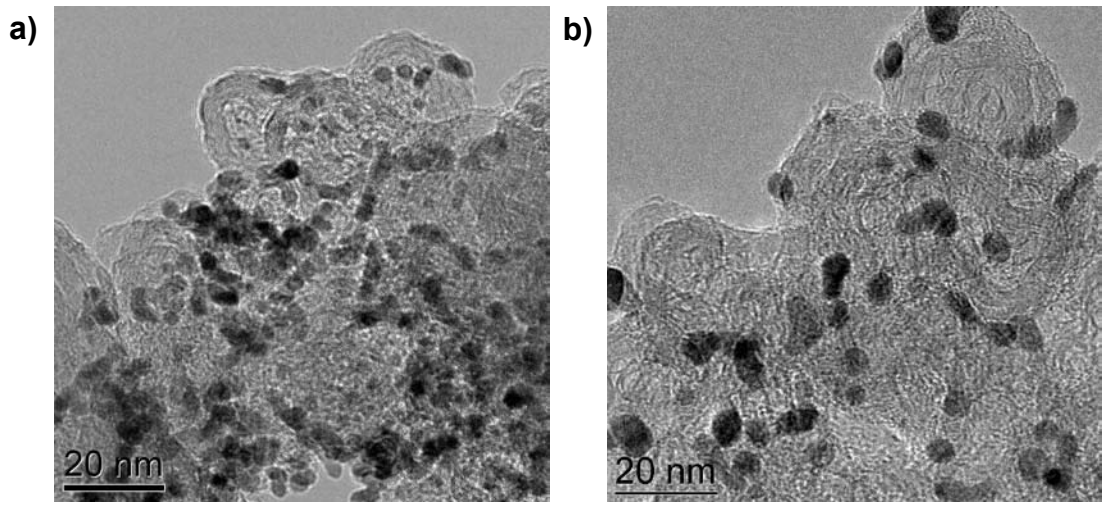

Figure 6.3 TEM images of Pt/GVC1600 before (a) and after (b) 60000 cycles of the potential cycle test.

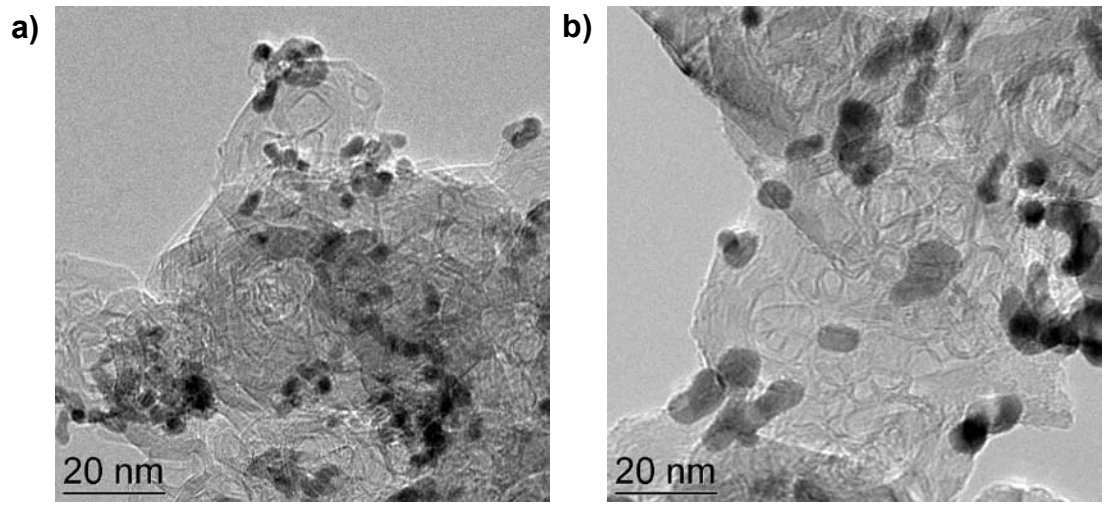

Figure 6.4 TEM images of Pt/GVC2000 before (a) and after (b) 60000 cycles of the potential cycle test.

After the 60000 cycles test, platinum particles were all grown in slightly different degree as shown in Figure 6.1b-6.4b. To compare the platinum particle size more quantitatively before and after the potential cycle test, the average platinum particle size was calculated from the TEM images and is listed in Table 6.1.

The platinum particle size after the potential cycle test remained within the range of 4.09-5.30 nm, which is reasonable to consider the fact that platinum particles increase their structural stability once their size becomes to be 3-5 nm. Although there is no report which examined platinum particle growth in the exactly same condition with ours, on consideration of other report [1], the resulting considerable growth of platinum particles is practical.

Although similar growth in platinum particle size was observed for all Pt/C electrocatalysts, platinum particles least grew for Pt/GVC1600 with an increase of 1.24 nm. Therefore, TEM images also demonstrated that Pt/GVC1600 exhibited the highest durability during the potential cycle test owing to the carbon surface with sufficient corrosion resistance and interaction with platinum particles derived by adequate heat treatment.

Table 6.1 Average platinum particle size of Pt/Vulcan group electrocatalysts before and after the potential cycle test.

Pt/C electrocatalyst	Initial d_{TEM} (nm)	After 60000 cycles d_{TEM} (nm)
Pt/VC	2.32 ± 0.38	4.55 ± 1.26
Pt/GVC1100	2.44 ± 0.30	4.28 ± 1.20
Pt/GVC1600	2.85 ± 0.46	4.09 ± 0.75
Pt/GVC2000	2.88 ± 0.42	5.30 ± 1.27

Using the average size of platinum particles in Table 6.1, theoretical surface area (TSA) was determined with the assumption of spherical shape for all platinum particles, and is listed together with theoretical % retention ($TSA_{after\text{-}60k\text{-}cycle}/TSA_{initial}$) in Table 6.2. Retention of ECA after 60000 cycles calculated in Table 4.1 was also listed in Table 6.2 for the comparison.

Table 6.2 Theoretical surface areas (TSAs) of Pt/Vulcan group electrocatalysts.

Pt/C electrocatalyst	Initial TSA* (m^2g^{-1})	TSA* after 60000 cycles (m^2g^{-1})	Theoretical retention (%)	ECA** Retention (%)
Pt/VC	120.5	61.5	51.0	36.3
Pt/GVC1100	114.6	65.3	57.0	40.0
Pt/GVC1600	98.1	68.4	69.7	70.4
Pt/GVC2000	97.1	52.8	54.4	40.2

* TSA was calculated based on the average platinum particle size observed in TEM images with the assumption that all of the platinum nanoparticles can be regarded to be spherical with the density of platinum, 21.45 g cm^{-3}.

**The values of ECA retention were reproduced from Table 4.1.

Theoretical % retention showed a similar trend to % retention of ECA after the potential cycle test. By considering that a part of platinum particles are embedded into the carbon support and not used for electrocatalytic reactions, the difference between theoretical and experimental results seems reasonable.

6.1.2 Evaluation of Pt/Ketjen Black Group Electrocatalysts by Ex-situ TEM Observation

Figure 6.5, 6.6, 6.7, and 6.8 show TEM images of Pt/KB, Pt/GKB1100, Pt/GKB1600, and Pt/GKB2000, respectively. Before the potential cycle test, platinum particles with almost the same size were evenly distributed on carbon supports.

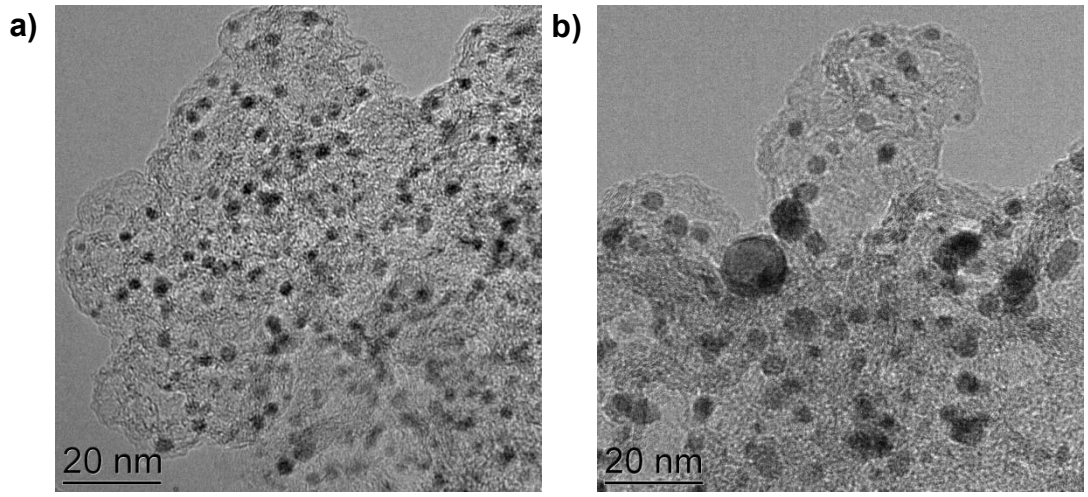

Figure 6.5 TEM images of Pt/KB before (a) and after (b) 60000 cycles of the potential cycle test.

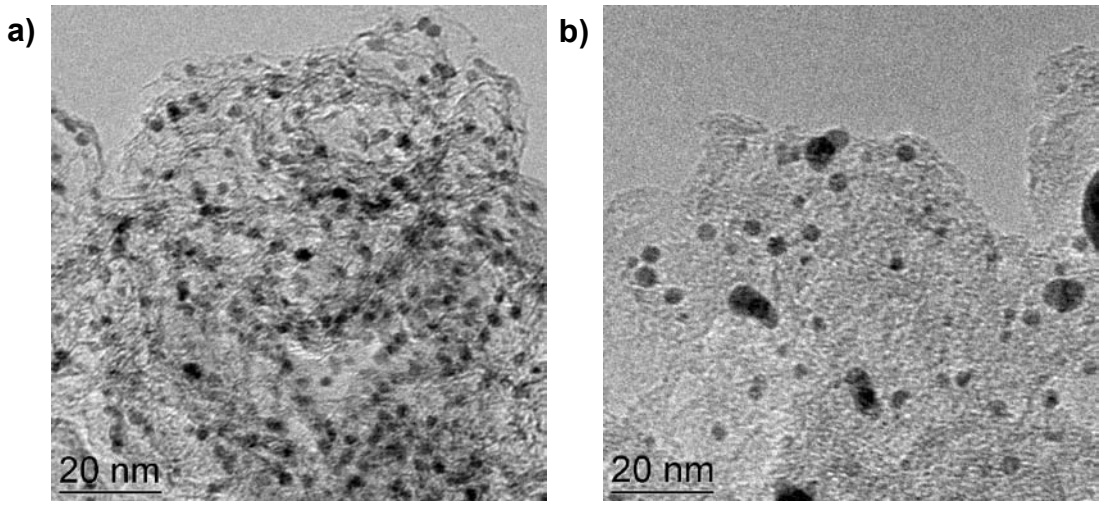

Figure 6.6 TEM images of Pt/GKB1100 before (a) and after (b) 60000 cycles of the potential cycle test.

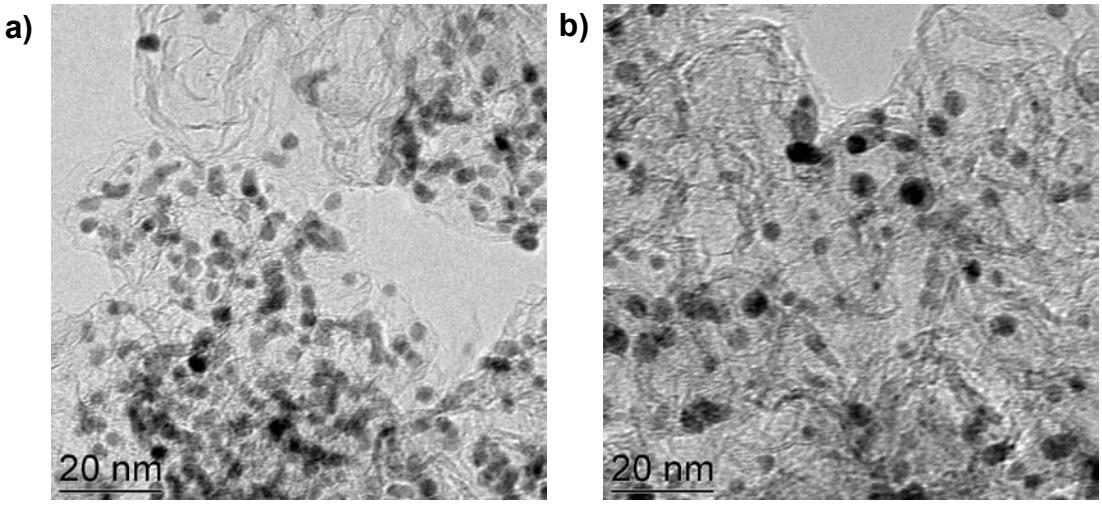

Figure 6.7 TEM images of Pt/GKB1600 before (a) and after (b) 60000 cycles of the potential cycle test.

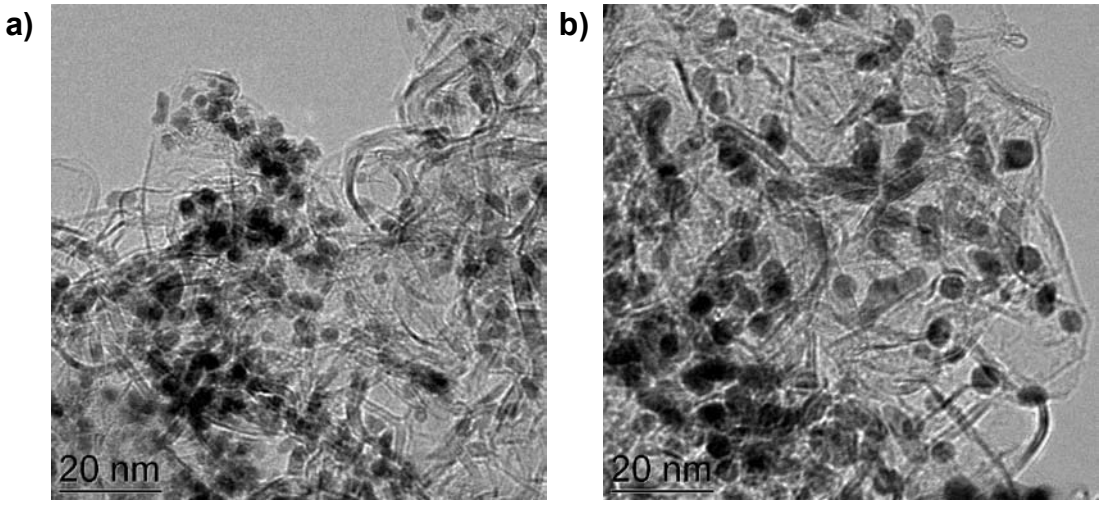

Figure 6.8 TEM images of Pt/GKB2000 before (a) and after (b) 60000 cycles of the potential cycle test.

For Pt/GKB1600 and Pt/GKB2000, the graphite-like layers were clearly observed in Figure 6.7a and Figure 6.8a, respectively. Platinum particles were adequately dispersed on the carbon supports even though the aggregation of platinum slightly appeared.

After the 60000 cycles test, platinum particles were all grown in different degree as shown in Figures 6.5b-6.8b. The average platinum particle size before and after the potential cycle test was calculated from the TEM images for the quantitatively comparison and is listed in Table 6.3.

Table 6.3 Average platinum particle size of Pt/Ketjen Black group electrocatalysts before and after the potential cycle test.

Pt/C electrocatalyst	Initial d_{TEM} (nm)	After 60000 cycles d_{TEM} (nm)
Pt/KB	2.11 ± 0.36	3.62 ± 1.38
Pt/GKB1100	2.14 ± 0.35	3.35 ± 1.57
Pt/GKB1600	2.53 ± 0.33	3.11 ± 0.75
Pt/GKB2000	2.62 ± 0.39	4.01 ± 0.56

Compared to the Pt/Vulcan group electrocatalysts, Pt/Ketjen Black group electrocatalysts rather showed suppressed platinum growth within the range of 3.11-4.01 nm, even though both group electrocatalysts started with a similar platinum size. Similar to the case of Pt/Vulcan group, Pt/GKB1600 showed the least growth of platinum with the increase of 0.58 nm. TEM images again demonstrated that Pt/GKB1600 earned the highest durability owing to increased carbon corrosion resistance and sufficient interaction with platinum particles derived by the adequate heat treatment.

Using the average size of platinum particles in Table 6.3, TSA was also determined with the assumption of spherical shape for all platinum particles, and is listed together with theoretical % retention ($TSA_{after\text{-}60k\text{-}cycle}/TSA_{initial}$) in Table 6.4. Retention of ECA after 60000 cycles calculated in Table 4.2 was also listed in Table 6.4 for the comparison.

ECA % retention for Pt/KB and Pt/GKB1100 resulted in extremely lower than theoretical retention, even though for Pt/GKB1600 and Pt/GKB2000, theoretical and experimental retention remained within the same trend. On consideration of the size of platinum particles like 3 nm after the potential cycle test, % retention of ECA like 2% for Pt/KB and Pt/GKB1100 is too low and cannot be explained. This confliction can only be explained if detachment and/or dissolution of platinum particles into the electrolyte

solution occurs in case of Pt/KB and Pt/GKB1100.

Table 6.4 Theoretical surface areas (TSAs) of Pt/Ketjen Black group electrocatalysts.

Pt/C electrocatalyst	Initial TSA* (m^2g^{-1})	TSA* after 60000 cycles (m^2g^{-1})	Theoretical retention (%)	ECA** retention (%)
Pt/KB	132.5	77.2	58.3	2.1
Pt/GKB1100	130.6	83.5	63.9	1.8
Pt/GKB1600	110.5	89.9	81.4	46.8
Pt/GKB2000	106.7	69.7	65.3	35.5

* TSA was calculated based on the average platinum particle size observed in TEM images with the assumption that all of the platinum nanoparticles can be regarded to be spherical with the density of platinum, 21.45 g cm^{-3}.

**The values of ECA retention were reproduced from Table 4.2.

6.1.3 Evaluation of Pt/C Electrocatalysts by ICP Analysis

In order to understand much lower ECA than the expected value, the electrolyte solution after the potential cycle test was examined. The amount of platinum ions, including platinum nanoparticles, in the electrolyte solution after 60000 c ycles was evaluated by ICP for selected Pt/C electrocatalysts (Pt/KB, Pt/VC, and Pt/GVC1600). The measurements were repeated two to three times for each sample, and then average % platinum dissolution was determined and listed in Table 6.5.

Table 6.5 Platinum dissolution in the electrolyte analyzed by ICP.

	Pt dissolution (%)			
	Sample #1	Sample #2	Sample #3	Average
Pt/KB	73.4	64.7	-	69.1
Pt/VC	37.1	31.0	35.7	34.6
Pt/GVC1600	11.8	11.7	12.8	12.1

As seen in Table 6.5, Pt/KB showed 69.1% dissolution of platinum although Pt/VC showed much less like 34.6%. Therefore, together with the results from TEM in section 6.1.2, Pt/KB lost most of its ECA more predominately by dissolution than agglomeration of platinum. Furthermore, platinum dissolution phenomenon was suppressed through the surface graphitization as seen in Pt/GVC1600, resulting in only 12.1% dissolution. Considering the increase in the mobility of platinum particles on more graphitized

surface of GVC1600, we believe that dissolution phenomenon is rather deeply related to the corrosion resistance than to the mobility of platinum particles on the carbon support.

6.2 Degradation of Pt/C Electrocatalysts at Elevated Temperatures Under the Air (Collaborative Work with Hitachi High Technologies Corporation)

In order to gain fundamental understanding of degradation mechanism of Pt/C electrocatalysts, accelerated degradation test was performed by heating the selected Pt/C electrocatalysts in the air, and a simultaneous in-situ SEM/STEM study was carried out under the accelerated degradation condition.

For this experiment, two samples, Pt/VC and Pt/GVC1600, were selected. Continuous SEM/STEM observation for 30 minutes was performed at 200 °C in the air condition.

6.2.1 Evaluation of Pt/VC by In-situ SEM/STEM Observation

Initial SEM/STEM images for Pt/VC are shown in Figure 6.9. Two images of platinum particles distributed on Vulcan were almost the same.

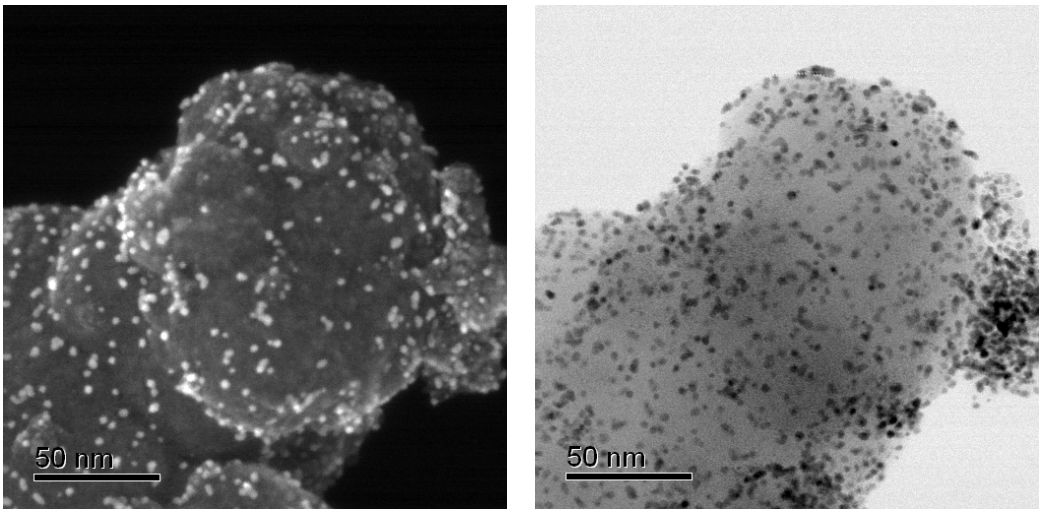

Figure 6.9 Initial SEM (left) and STEM (right) images of Pt/VC.

Then, during the acceleration test at 200 °C in the air, in-situ SEM/STEM images were continuously captured. Sequence of SEM images was placed in Figure 6.10.

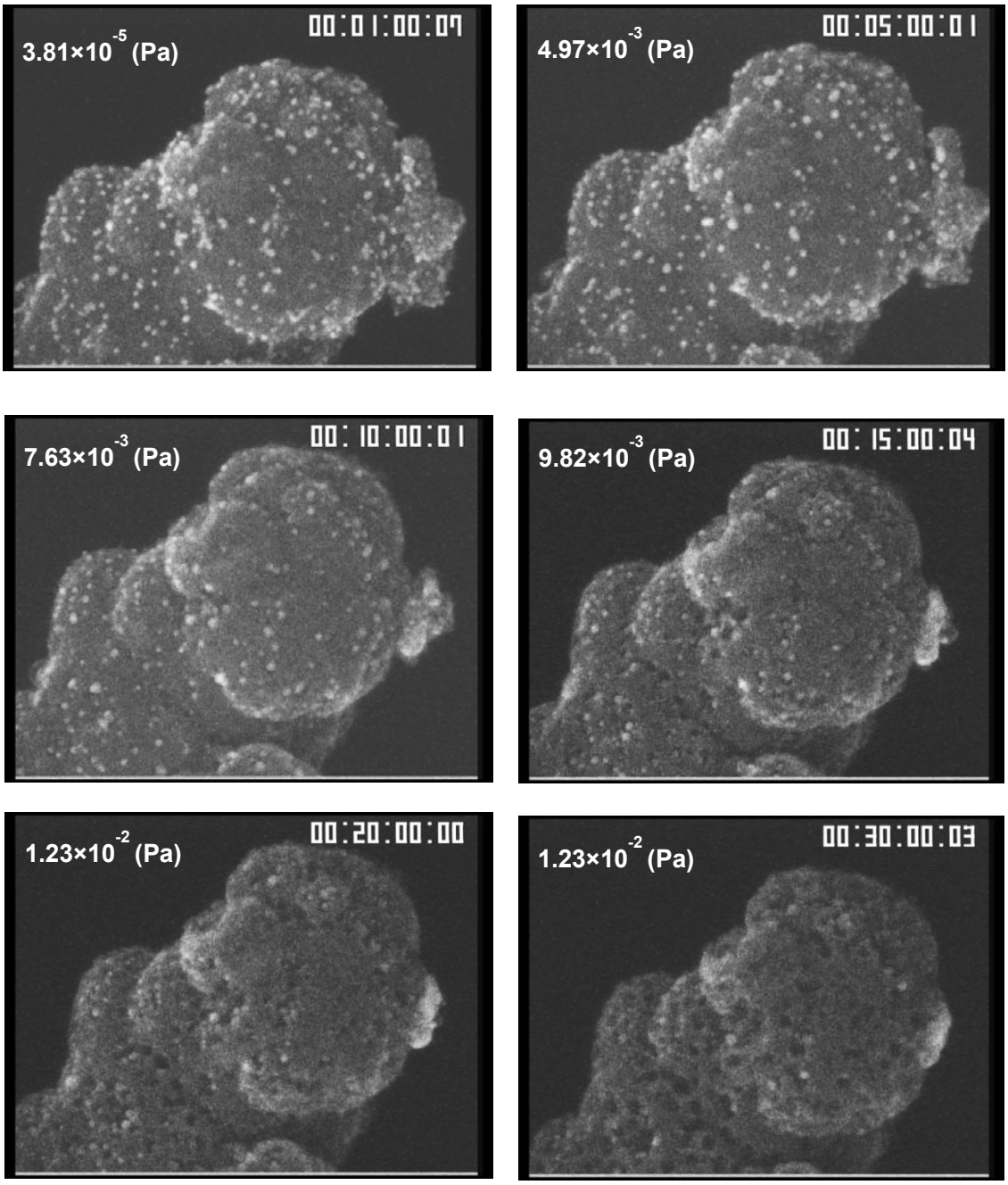

Figure 6.10 Sequence of SEM images for Pt/VC. Observation was performed at 200 °C during the air injection.

During the accelerated degradation test, platinum particles on the carbon surface did not agglomerate much and were rather gradually embedded into the carbon surface owing to carbon corrosion. After 30 minutes, most of platinum particles were not on the carbon surface.

SEM/STEM images of Pt/VC after the accelerated degradation test are shown in Figure 6.11. In this case, two images of platinum particles were very different. The STEM image itself cannot explain the reason for decreased catalytic activity since platinum particles look small and well distributed. However, simultaneous SEM/STEM observation gives us a p ossible reason for low activity, where platinum particles are embedded and not used for catalytic reactions.

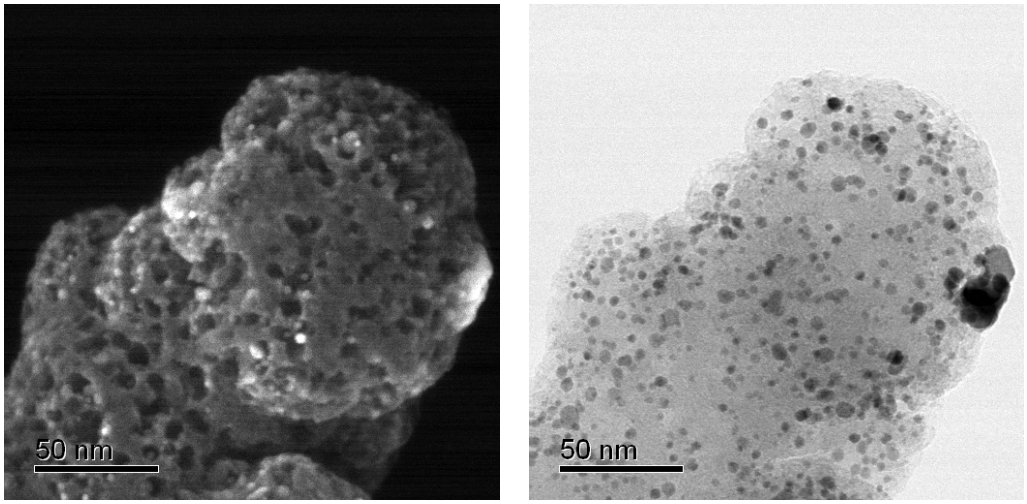

Figure 6.11 SEM (left) and STEM (right) images of Pt/VC after the accelerated degradation test at 200 °C under the air injection.

6.2.2 Evaluation of Pt/GVC1600 by In-situ SEM/STEM Observation

Initial SEM/STEM images of Pt/GVC1600 are shown in Figure 6.12. Again, two images of platinum particles distributed on GVC1600 were almost the same.

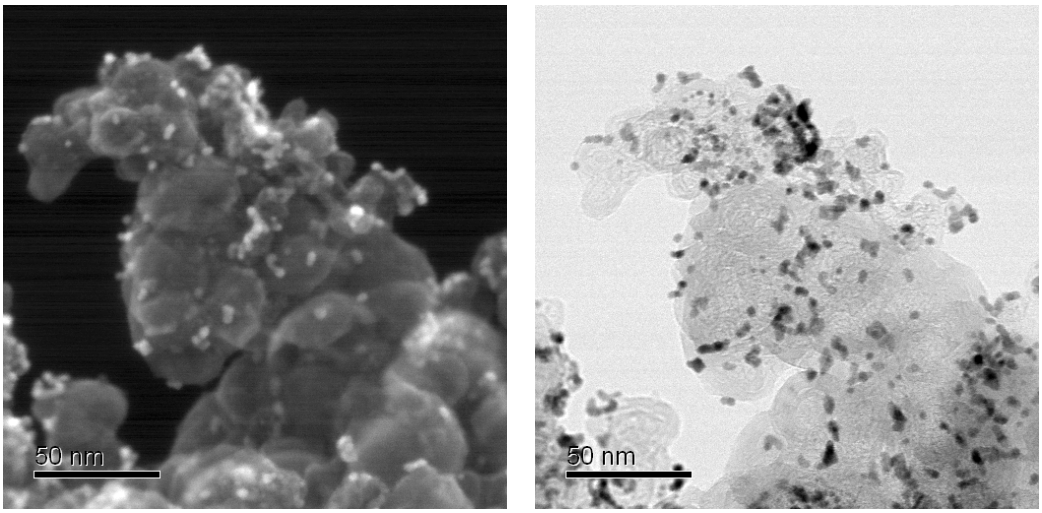

Figure 6.12 Initial SEM (left) and STEM (right) images of Pt/GVC1600.

Then, in-situ SEM/STEM images were continuously captured during the accelerated degradation test. Sequence of SEM images was listed in Figure 6.13.

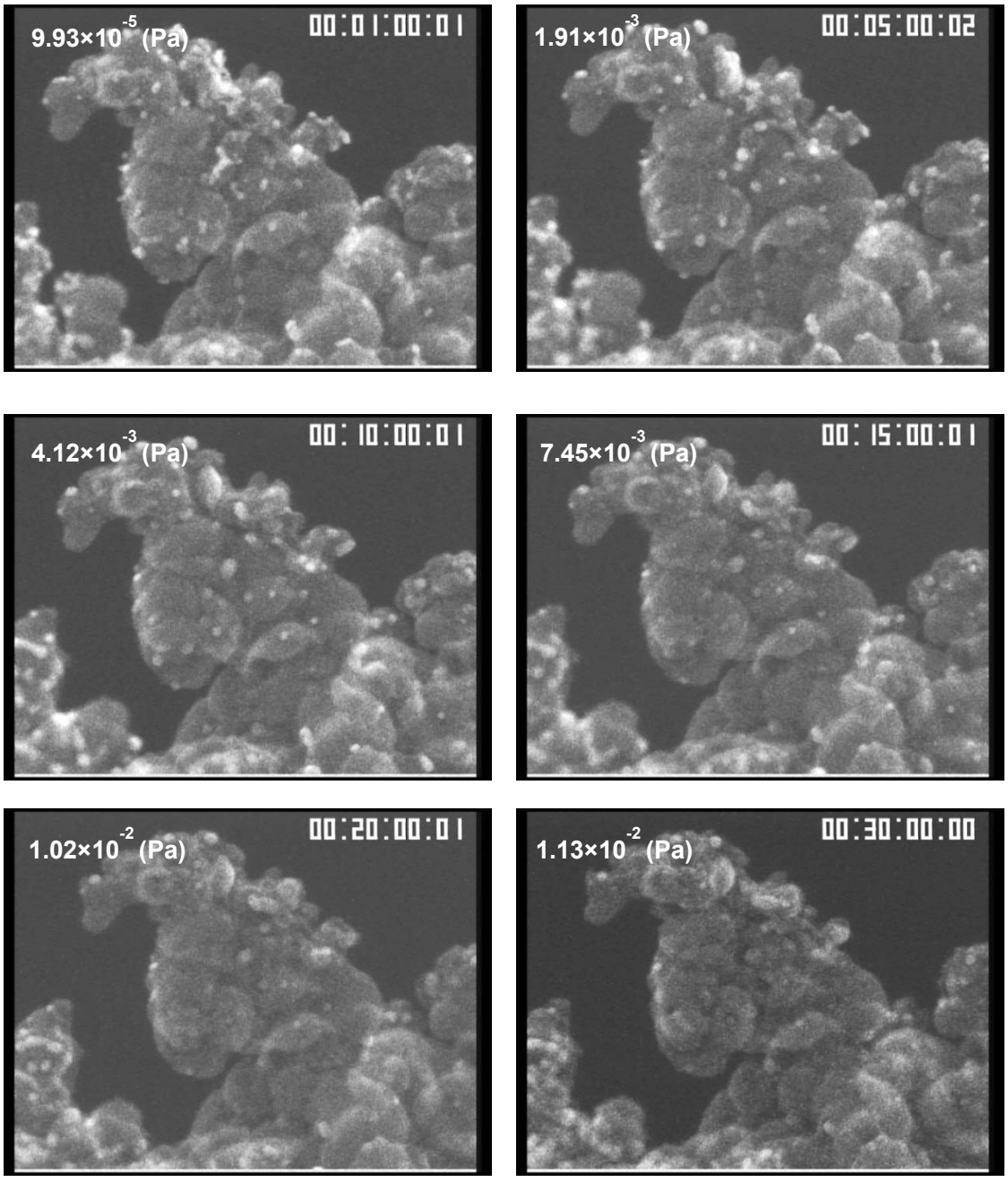

Figure 6.13 Sequence of SEM images for Pt/GVC1600. Observation was performed at 200 °C during the air injection.

Unlike Pt/VC, platinum particles on the carbon surface rather agglomerated but not embedded much even after 30 minutes. Graphitized surface led to more agglomerated but

not embedded platinum, probably resulting in higher activity. This phenomenon suggests a key factor to develop durable electrocatalysts.

SEM/STEM images of Pt/GVC1600 after the accelerated degradation test are shown in Figure 6.14. Unlike Pt/VC, two images of platinum particle were almost the same.

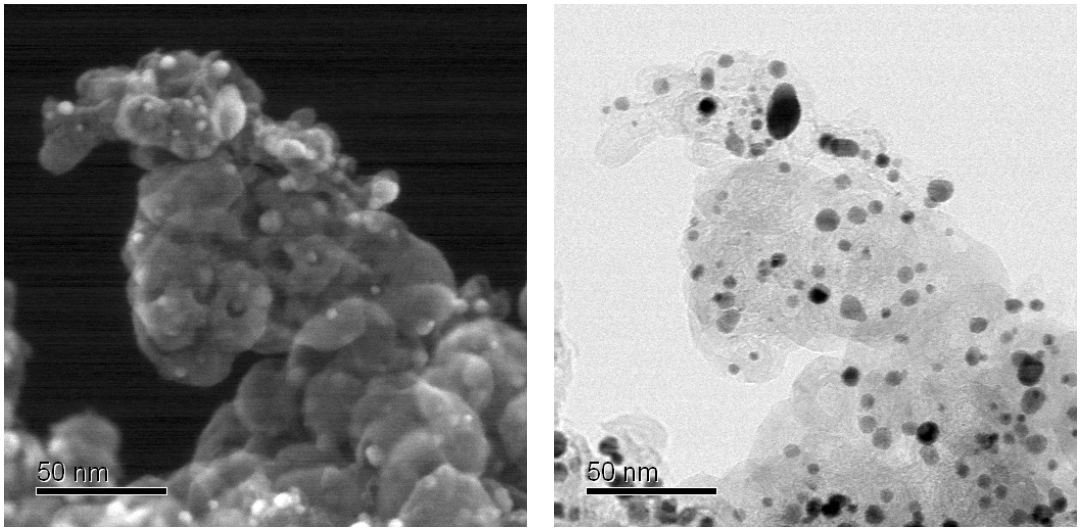

Figure 6.14 SEM (left) and STEM (right) images of Pt/GVC1600 after the accelerated degradation test at 200 °C under the air injection.

6.2.3 Comparison with Degradation in Half-cell Reaction through Ex-situ SEM/STEM Observation

Since a new degradation phenomenon that platinum particles were embedded into the carbon was found in section 6.2.1−6.2.2, simultaneous SEM/STEM observation was performed for Pt/VC and Pt/GVC1600 after the potential cycle test. SEM and STEM images for Pt/VC and Pt/GVC1600 after 60000 cycles are presented in Figure 6.15 and 6.16, respectively.

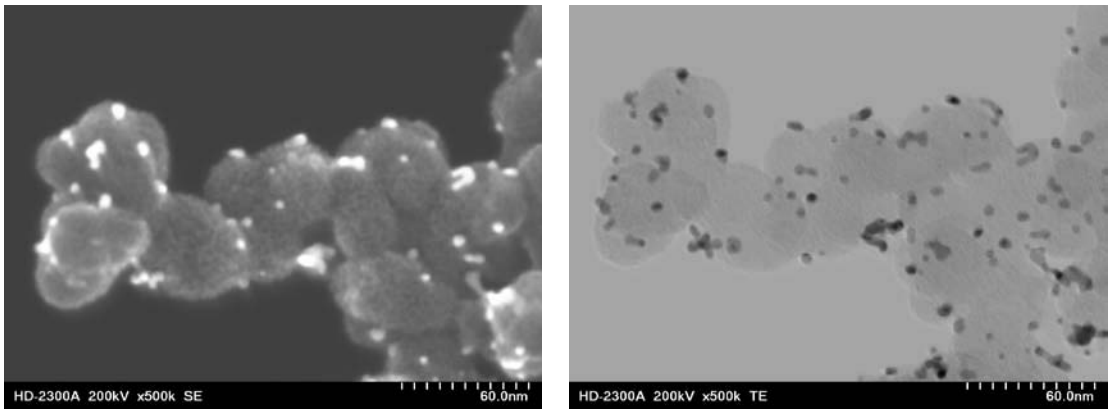

Figure 6.15 SEM (left) and STEM (right) images of Pt/VC after the 60000 potential cycle test. Both images were obtained at the exactly same position by switching the two modes.

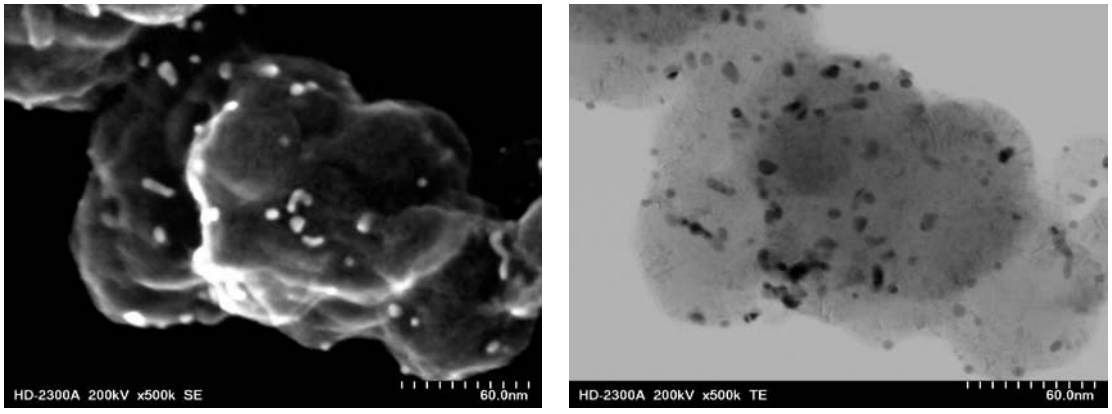

Figure 6.16 SEM (left) and STEM (right) images of Pt/GVC1600 after the 60000 potential cycle test. Both images were obtained at the exactly same position by switching the two modes.

As a result, SEM and STEM images of platinum particles were not very different for Pt/VC and Pt/GVC1600. Unlike the case of the accelerated degradation test by heating in the air, embedded platinum particles were not clearly observed.

Then, Pt/KB, which had much lower durability under the potential cycle test, was evaluated by SEM/STEM.

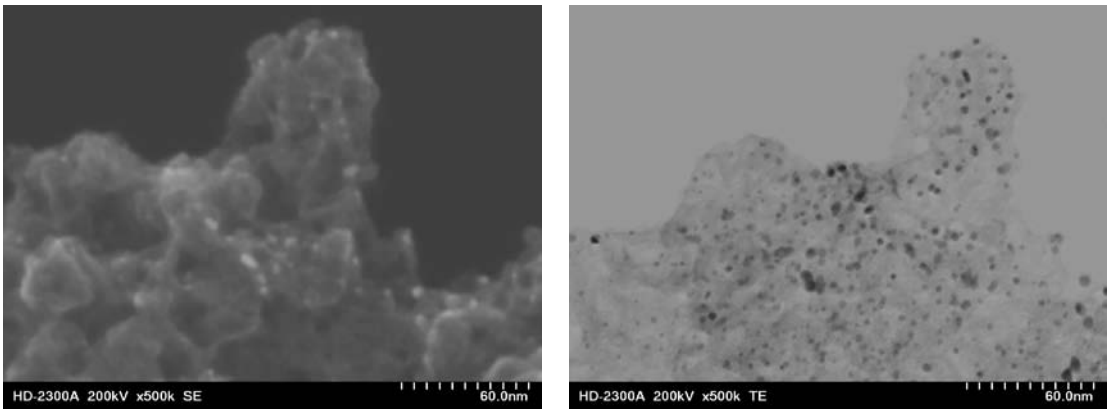

Figure 6.17 SEM (left) and STEM (right) images of Pt/KB after the 60000 potential cycle test. Both images were obtained at the exactly same position by switching the two modes.

Comparing SEM and STEM images of Pt/KB (Figure 6.17), they were very different. A lot of platinum particles observed in the STEM image were not seen in the SEM image. Also, many holes probably made by corrosion were observed. Since Ketjen Black had a nanostructure with hollows, platinum particles existed inside the hollows and SEM and STEM images of platinum particles were different even before the potential cycle test as shown in Figure 6.18. However, many holes on the surface were not seen at the initial stage, and they were surely made during the potential cycle test.

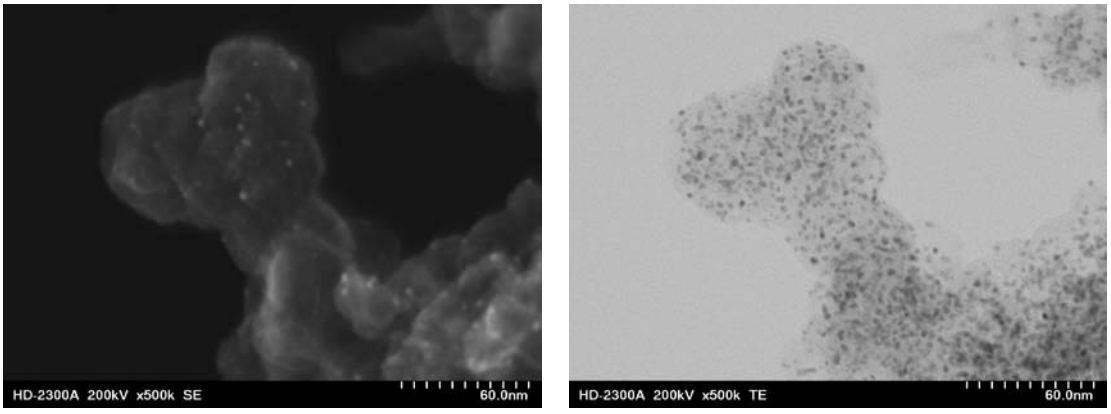

Figure 6.18 SEM (left) and STEM (right) images of Pt/KB before the potential cycle test. Both images were obtained at the exactly same position by switching the two modes.

Consequently, we believe the degradation mechanism observed by heating in the air is the same as the degradation mechanism derived by the potential cycle test. However, the acceleration condition was more severe for heating in the air. Therefore, Pt/VC and Pt/GVC1600, which have relatively high durability, did not show embedded platinum after the potential cycle test.

6.3 Degradation of Pt/C Electrocatalysts in MEAs

During the evaluation of MEAs with Pt/VC and Pt/GVC1600 cathode layers in chapter 5, it was found that Pt/GVC1600 had much more improved durability than that of Pt/VC. In order to investigate how those electrocatalysts were differently degradated, nanostructures of the cathode layer in each MEA were studied by FESEM. SEM images of Pt/VC and Pt/GVC1600 cathode layer are presented in Figure 6.19 and 6.20, respectively.

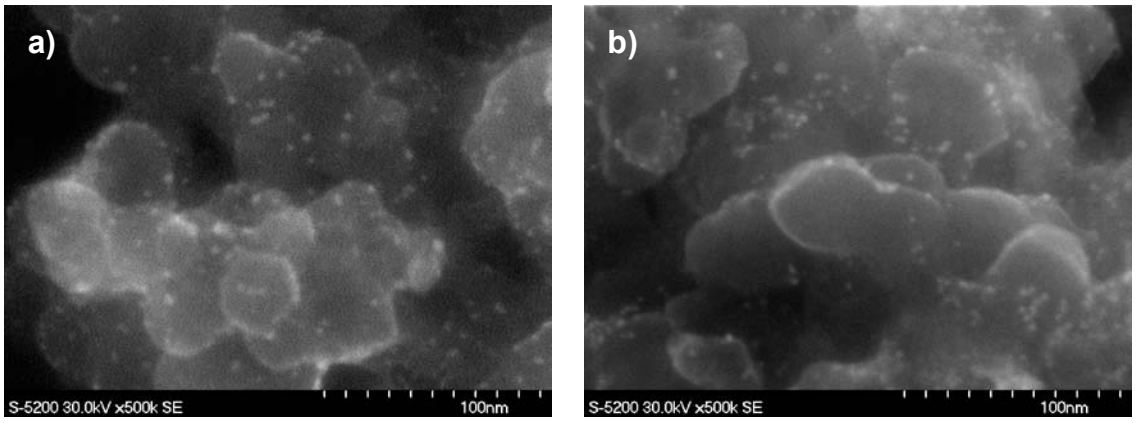

Figure 6.19 SEM images of Pt/VC cathode layer before (a) and after (b) the 5000 potential cycle test.

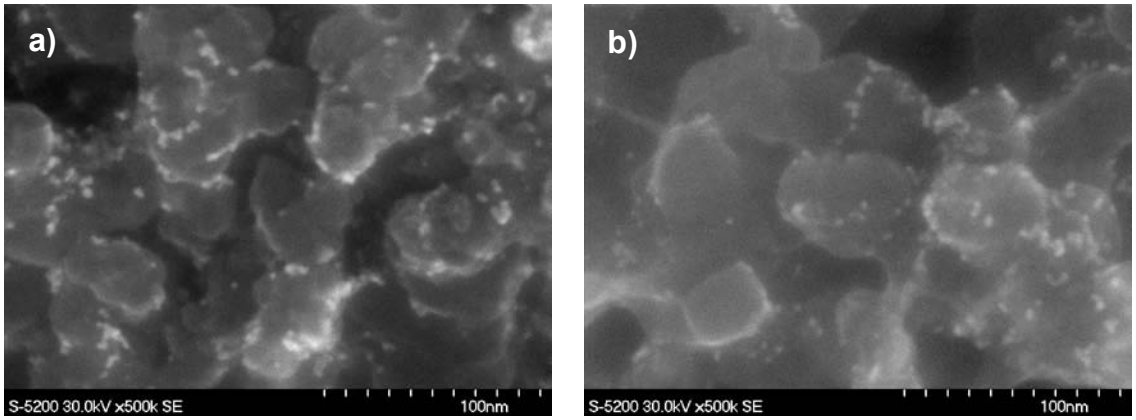

Figure 6.20 SEM images of Pt/GVC1600 cathode layer before (a) and after (b) the 5000 potential cycle test.

Comparing SEM images before and after the 5000 potential cycle test for Pt/VC (Figure 6.19), evenly distributed initial platinum particles on the carbon support showed agglomeration on a certain portion of carbon after the cycle test. Embedded platinum was not observed, either. On considering the size of platinum, although platinum particles slightly grew, but no platinum over 10 nm was observed.

For Pt/GVC1600 (Figure 6.20), the difference before and after the cycle test was slightly smaller comparing to Pt/VC, even though platinum particles were initially larger and more agglomerated, which was also observed in section 6.1.1.

No clear difference was observed between Pt/VC and Pt/GVC1600 cathode layer after the 5000 cycles. On the other hand, in reality, MEA with Pt/VC lost most of its performance while MEA with Pt/GVC1600 still kept enough activity. Therefore, reasons for MEA degradation cannot be simply explained by SEM images. Although analyses of nanostructures in detail are further necessary to understand the degradation mechanism, there is possible migration of platinum into an ionomer pocket between carbon support spheres, reported by More et. al [2], leading to decrease the performance.

6.4 Conclusions

In order to understand the possible degradation mechanism, nanostructures of Pt/C electrocatalysts were evaluated. From Ex-situ TEM observation of Pt/C electrocatalysts before and after the potential cycle test, improved durability for Pt/GVC1600 and Pt/GKB1600 was also proven by their graphite-like surface structure and sufficient interaction between platinum and carbon.

On the other hand, Pt/KB, which had lowest durability, rather showed well dispersed platinum particles, leading to a contradiction between small platinum particles and low ECA. To understand much lower ECA than the expected value, the electrolyte solution after the potential cycle test was examined by ICP. As a result, dissolution of platinum was found to be a predominate factor for degradation of Pt/KB.

On the purpose of gaining fundamental understanding of degradation mechanism of Pt/C electrocatalysts, accelerated degradation test was performed by heating selected electrocatalysts in the air. From the simultaneous in-situ SEM/STEM observation, the phenomenon that platinum particles were embedded into carbon was newly found for Pt/VC, which suggested that this phenomenon was one possible degradation mechanism. Moreover, embedded platinum was suppressed very much through the graphitization of carbon surface.

This new degradation phenomenon was seen with the Pt/C electrocatalyst after the potential cycle test even though that was only seen for Pt/KB, which had lowest

durability. Therefore, we believe that degradation mechanism observed by heating in the air is the same as the degradation mechanism derived by the potential cycle test even though the acceleration condition is more severe for heating in the air.

Finally, degradation of MEA performance cannot clearly be explained from SEM observation by the change of platinum particles. Detailed studies of nanostructures of catalyst layers, including the Nafion structure, are further necessary in order to understand degradation mechanism.

References

[1] Y. Chengfei, E.F. Holby, R. Yang, M.F. Toney, D. Morgan, P. Strasser, Growth trajectories and coarsening mechanisms of metal nanoparticle electrocatalysts, ChemCatChem, 4 (2012) 766.

[2] K.L. More, R. Borup, K.S. Reeves, Identifying contributing degradation phenomena in PEM fuel cell membrane electrode assemblies via electron microscopy, ECS Trans., 3(1), (2006) 717.

Chapter 7

Conclusions

7.1 Conclusions

Heat treatment of carbon materials leads to increase in carbon corrosion resistance owing to the formation of graphitized surface, however at the same time, to increase in the mobility of platinum particles. Therefore, heat treatment at optimum temperature is necessary. In our study, heat treatment at 1600 °C resulted in the highest durability. Not only graphitization degree but also original nanostructure of carbon affects the durability. Vulcan had higher durability than Ketjen Black. Increased durability is also well pronounced for MEA under the actual operational conditions.

Possible degradation mechanism was investigated. Degradation mechanism depends on carbon nanostructure. In the Pt/KB case, platinum dissolution is predominant over platinum particle growth, which is a major factor for degradation in the other cases. In order to understand fundamental material degradation mechanism, accelerated degradation test by heating electrocatalysts in the air was performed. From the simultaneous in-situ SEM/STEM observation, the phenomenon that platinum particles are embedded into carbon owing to carbon corrosion is newly found. This phenomenon is even suppressed on the graphitized surface. In comparison to the surface resulting from the potential cycle test, this new acceleration test is rather a more severe test, but the degradation mechanism is the same in both cases. However, more detailed studies of nanostructures for catalyst layers in MEA are necessary in order to understand the degradation mechanism not only for electrocatalysts but also for catalyst layers including Nafion.

Finally, the aim of this study is not limited to synthesize the best electrocatalysts, and we rather propose that the graphitization degree is an important factor to develop electrocatalysts with high durability for designing next generation fuel cells.

7.2 Outlook and Future Work

Even though our final goal is not limited to develop a best electrocatalyst, we believe that further optimization is possible. We have been working on mesoporous carbon (MC) which contains nanochannel structures [1-4] (Figure 7.1). In this case, platinum mobility is suppressed by encapsulation of platinum particles into the nanochannels, resulting in higher durability. Combination with surface graphitization technique is believed to be an ideal structural design principle to further improve the durability.

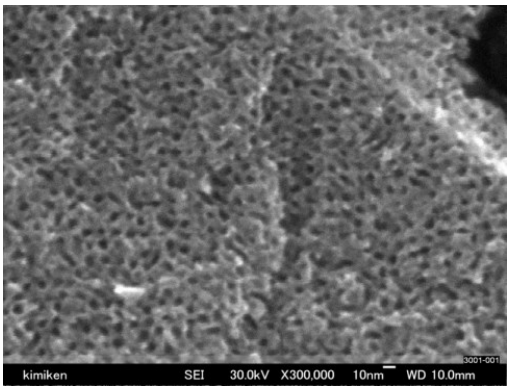

Figure 7.1 A SEM image of powder MC.

References

[1] A. Hayashi, H. Notsu, K. Kimijima, J. Miyamoto, I. Yagi, Preparation of Pt/mesoporous carbon (MC) electrode catalyst and its reactivity toward oxygen reduction, Electrochim. Acta, 53 (2008) 6117.

[2] A. Hayashi, K. Kimijima, J. Miyamoto, I. yagi, Direct observation of well-dispersed Pt nanoparticles inside the pores of mesoporous carbon through the cross section of Pt/mesoporous carbon particles, Chem. Lett., 38 (2009) 346.

[3] A. Hayashi, K. Kimijima, J. Miyamoto, I. yagi, Oxygen transfer and storage processes inside the mesopores of platinum-deposited mesoporous carbon catalyst thin-layer electrode, J. Phys. Chem. C, 113 (2009) 12149.

[4] I. Yagi, A. Hayashi, K. Kimijima, H. Notsu, N. Ohta, A Yamaguchi, Mesoporous materials toward nanofabricator and nanoreactor, Electrochemistry, 78 (2010) 105.